To the Graduate Council:

I am submitting herewith a dissertation written by Ajith H. Wijenayake entitled "DESIGN AND EFFICIENCY OPTIMIZATION OF AN AXIAL GAP PERMANENT MAGNET SYNCHRONOUS MACHINE ADJUSTABLE SPEED DRIVE SYSTEM". I have examined the final copy of this dissertation for form and content and recommend that it be accepted in partial fulfillment of the requirements for the degree of Doctor of Philosophy, with a major in Electrical Engineering.

J. M. Bailey, Major Professor

We have read this dissertation
and recommend its acceptance:

Accepted for the council:

Associate Vice Chancellor
and Dean of the Graduate School

DESIGN AND EFFICIENCY OPTIMIZATION OF AN AXIAL GAP PERMANENT MAGNET SYNCHRONOUS MACHINE ADJUSTABLE SPEED DRIVE SYSTEM

A Dissertation

Presented for the

Doctor of Philosophy

Degree

The University of Tennessee, Knoxville

Ajith H. Wijenayake

August 1995

DEDICATION

To my parents, Amaris Wijenayake and Babinona Wijenayake,

my sister Joslin Amugoda, my brother Karunasena Wijenayake

and

my loving wife Anoma for her unconditional support.

ACKNOWLEDGMENTS

This work has been made possible due to the help of several people. First, I wish to express my deep appreciation to my advisor, Professor J. Milton Bailey for his guidance, encouragement, and kindness over the years. A special thank is also reserved for Professor Jack Lawler and Professor Herbert P. Neff for providing much appreciated advice and guidance during this study. I would also like to thank the other members of my doctoral committee, Dr. M. O. Pace, Dr. J. N. Snider, and Dr. C. Edirisinghe, for their kindness in serving as my supervisory committee.

I would also like to thank Ben Banerjee of Electric Power Research Institute for his support. The advice and support of Dr. P. J. McCleer of McCleer Power, Inc., has been a great help. I am also grateful to my sisters, Rupa Walpola, Indra Perera, and Kanthi Senaratne, and their families, and my friend Anoja de Alwis for their encouragement during my degree-seeking years. In particular, I wish to thank Dr. Josiah Hoskins and Gary Rauscher of Allen-Bradley Company, Inc., for their kindness and help during the last stages of preparation of this manuscript. Thanks are also due to Dr. B. K. Bose for introducing me to Power Electronics.

I would also like to thank Suanne and T. A. Lewis, Robert Citkowski, Sriram Adhyapak, and Steven Daniel for their comments and help. Finally, I wish to thank Sapumal Mendis and Dammika Weeratunga for their technical discussions, advice, and help in many ways.

ABSTRACT

In all areas of adjustable speed drive applications, there is a great need for increased performance, power density and reliability.

A method of design, analysis and performance optimization of an axial gap permanent magnet synchronous machine adjustable speed drive system is discussed in this dissertation. Initially, a brief analysis of the design parameters and their contribution to the drive system performance is discussed. The equations for the machine performance parameters are developed in terms of input design parameters. The single objective optimization (scalar optimization) procedure for performance parameters enhancement, in terms of machine efficiency and specific power has been presented. A multi-objective optimization (vector optimization) procedure, which optimizes the specific power and the efficiency is also discussed for a 3200 rpm, 100 Hp, 216 Volts axial gap brushless dc machine. The feasibility frontier curve, which represents the set of optimum design points under the given constraints, is obtained by changing the weighting factors associated with the multi-objective function.

Next, the analysis and the efficiency optimization of the vector controlled axial gap permanent magnet brushless dc drive system is discussed, using an actively clamped resonant dc link inverter. The resonant frequency at which the inverter losses are minimum is obtained using a scalar optimization procedure.

In the next chapter, an analytical solution for the no-load flux density distribution within the machine is obtained using three dimensional field analysis. The validity of the results is confirmed by comparing with the actual field measurement of the machine.

Finally, a Digital Signal Processor (DSP) based position sensor elimination method with an on-line parameter identification scheme is presented for a vector controlled permanent magnet synchronous machine drive system. This scheme accounts for the machine parameter variations and the core losses, and eliminates the shaft mounted encoder, resulting in a reliable, compact and a rugged drive system. A special inverter switching scheme at the machine start-up is also proposed and designed to enable the estimation algorithm to be used in the entire speed range, including the zero speed. The validity of the speed and position estimation algorithm is verified through simulation studies using SIMNON, a PC-based simulation language.

TABLE OF CONTENTS

1 Introduction 1

1.1 Power Electronics and Adjustable Speed Drives 1

1.2 Axial Gap Permanent Magnet Synchronous Machines 4

1.3 Comparative study for Axial Gap Permanent Magnet Synchronous Machines and Axial Gap Induction Machines 5

2 Design of Axial Gap Permanent Magnet Synchronous Machines

2.1 Introduction 7

2.2 Classical Design Approach 9

2.2.1 Stator Construction 9

2.2.2 Cogging Torque Consideration 10

2.2.3 Number of Stator slot/pole/phase is 1 11

2.2.4 Number of Stator slot/pole/phase is less Than 1 12

2.2.5 Number of Stator slot/pole/phase is Greater Than 1 12

2.2.6 Stator Slot Configuration 13

2.2.7 Rotor Construction 15

2.2.8 Stator Winding Configuration 17

2.2.9 Input Data Organization for the Design Problem 18

2.2.10 Mathematical Formulation of Design Output Data 21

2.2.11 Derivation of Performance Parameters 24

2.2.12 Stator Copper and Core Loss Calculations 26

2.2.13 Organization of the Classical Design Procedure 28

2.3 Specific Power Optimization with a Constraint on Efficiency 34

2.3.1 Method of Optimization Using QPRO 34

2.3.2 Variable Design Parameters 36

2.3.3 Constraints on the Design Parameters 36

2.3.4 Formulation of the Optimization Problem..... 39
2.4 Three and Five Phase Axial Gap Brushless DC Machines..... 50
2.4.1 Introduction..... 50
2.4.2 Comparative Representation..... 51
2.5 Multi-Objective Optimization Approach for Practical Applications..... 56
2.5.1 Introduction..... 56
2.5.2 Bi-criterion Optimization Problem Formulation and Solution..... 58

3 Selection of Inverter Topology for Adjustable Speed Drive System Analysis

3.1 Introduction..... 71
3.2 Actively Clamped Resonant DC Link Inverter and Adjacent/Zero State Current Controller with Zero Hysteresis Band..... 73
3.2.1 Principle of Operation of Actively Clamped Resonant DC Link Inverter..... 73
3.2.2 Adjacent/Zero State Current Controller with Zero Hysteresis Band Regulator..... 74
3.3 Loss Modeling of Inverter Switching Devices..... 77
3.3.1 Main Devices, (Q_1-Q_6) Losses..... 81
3.3.2 Auxiliary Device, Q_7 Losses..... 82
3.3.3 Auxiliary Switch, S_2 Losses..... 84
3.3.4 Auxiliary Diode, D_2 Losses..... 86
3.4 ACRDCL Efficiency Estimation for a Brushless DC Motor Drive.... 89
3.4.1 Resonant Pulse timing and Resonant Devices Peak Current Calculations..... 89
3.4.2 ACRDCL Efficiency Estimation..... 93
3.5 Efficiency Optimization of the ACRDCL Inverter..... 94

3.6 A Summary of the Drive System Performance Parameters..... 98

4 An Analytical Solution for the No-load Flux Distribution Within the Air Gap

4.1 Introduction..... 104

4.2 Mathematical Formulation to Obtain the Solution for Flux Components B_r, B_θ and B_z 104

4.2.1 Solution for No-load Flux Distribution Within the Air Gap..... 107

4.2.2 Application of the Boundary Conditions to Find Constants..... 112

5 Estimation of Rotor Position and Speed with an On-line Parameter Identification Scheme for PMSM Drives

5.1 Introduction..... 125

5.2 Development of an Accurate d^e-q^e Model..... 126

5.3 A Method to Account for Machine Parameter Variations due to Saturation and Temperature..... 131

5.4 Algorithm Development for the Estimation of Rotor Position and Rotor Speed..... 134

5.4.1 Rotor Position Estimation..... 134

5.4.2 Polarity Detection Test and Initial Rotor Position Estimation..... 137

5.4.3 Rotor Speed Estimation..... 145

5.5 DSP-Based Implementation of the Estimation Algorithm..... 147

5.6 Digital Simulation of the Drive System..... 151

5.6.1 Simulation Results..... 151

6 Conclusions and Recommendations for Future Research

6.1 Conclusions..... 156

6.2 Recommendations for Future Research..... 159

References..... 161

Appendices 168

A1 Formulation of the Optimization Problem using QPRO 169

A1.1 Introduction 169

A1.2 Optimizer Menu 169

A1.2.1 Solution Cell 169

A1.2.2 Variable Cells 170

A1.2.3 Constraints 170

A1.2.4 Options Menu 177

A1.3 A Brief Description About Quasi-Newton Methods 179

A2 Solutions for B_r, B_θ, and B_z 187

A3 Calculation of Three Flux Components 191

Vitae 195

LIST OF TABLES

2.1 Input design data..... 19

2.2 Input design data for a 100 Hp, 1800 Rpm, 600 Volts BDCM..... 29

2.3 Design output data and performance parameters 31

2.4 Efficiency in the torque-speed plane..... 32

2.5 Status of the parameters during optimization..... 37

2.6 Design parameters constraint table..... 38

2.7 Optimal design parameter table..... 42

2.8 Constraints and optimal values..... 43

2.9 Detail report of the each iteration step..... 44

2.10 Output and performance parameters for optimized and non-optimized design..... 45

2.11 Non-optimal/optimal design parameters for different design requirements.... 49

2.12 Optimized performance parameters for 3-phase and 5-phase configurations for optimum specific power..... 53

2.13 Optimized performance parameters for 3-phase and 5-phase configurations for optimum efficiency..... 53

2.14 Optimal design input parameters..... 61

2.15 Optimal design output and performance parameters..... 63

2.16 Optimal output and performance parameters for different weighting factors.. 67

2.17 Efficiency and specific power sensitivity to weighting coefficients..... 68

3.1 Current error signals and allowed switching states..... 79

3.2 Ratings of the brushless dc machine used in efficiency estimation..... 92

3.3 Inverter devices data..... 92

3.4 Optimum parameters for ACRDCL inverter..... 97

3.5 Non-optimal and optimal performance parameters for ACRDCL/axial gap brushless motor drive system..... 102

4.1 Peak flux density in z-direction at different radial values..... 116

4.2 Peak flux density in r-direction at different radial values..... 117

4.3 Peak flux density in θ-direction at different radial values..... 118

4.4 The variation of B_r , B_θ and B_z along the center of the magnet face at r=4.835 inch. , as θ_p varies from -90^0 to $+90^0$..... 120

5.1 Machine ratings and parameters..... 133

5.2 Control logic signals at the machine start-up..... 141

A1.1 Input design parameters..... 171

A1.2 Output and performance parameters..... 173

A1.3 Block of variable cells..... 175

A1.4 Optimal design parameters..... 180

A1.5 Constraints and optimal values..... 181

A1.6 Detail report of each iteration step..... 182

A1.7 Optimal input design parameters..... 183

A1.8 Optimal output and performance parameters..... 185

A3.1 Roots of $U_6(m.5.50)=0$ and corresponding values of $U_6(m_i r)$, $U_6^1(m_i r)$ $U_7(m_i r)$ for r=4.835 inch..... 193

LIST OF FIGURES

1.1 Total power loss comparison..... 6

1.2 Efficiency comparison..... 6

1.3 Motor weight comparison..... 6

1.4 Specific weight comparison..... 6

2.1 Axial gap permanent magnet machine configurations..... 8

2.2 Slotted stator of an axial gap machine..... 10

2.3 Stator slot configuration..... 10

2.4 Per phase equivalent circuit for a permanent magnet machine..... 16

2.5 Over-pitched winding configuration for a three phase machine with 14-poles and 12-slots..... 17

2.6 Over-pitched winding configuration for a five phase machine with 22-poles and 20-slots..... 18

2.7 Stator slot configuration with a double layer winding..... 23

2.8 Efficiency map in the torque-speed plane..... 33

2.9 Efficiency curves in the torque-speed plane..... 47

2.10 Main performance parameter's sensitivity to the pole order..... 48

2.11 Performance parameters comparison for 3 phase and 5 phase configurations for optimum specific power..... 54

2.12 Performance parameters comparison for 3 phase and 5 phase

configurations for optimum efficiency..... 55

2.13 A typical trade-off curve for two performance parameters..... 57

2.14 Feasibility frontier curve for efficiency Vs. specific power..... 66

2.15 Efficiency variation over the operating region for different w_{ef} values..... 69

2.16 Performance parameter sensitivity to weight coefficients..... 70

3.1 Actively clamped resonant dc link inverter..... 72

3.2 Actively clamped resonant dc link voltage and current waveforms..... 73

3.3 Modes of operation of the ACRDCL Inverter..... 75

3.4 Resonant voltage pulse waveform during one switching cycle..... 76

3.5 Inverter switching configuration and allowed transition states..... 78

3.6 Over-snubbed switch off waveform of an IGBT..... 82

3.7 Current and voltage waveform of auxiliary switch S_2..... 84

3.8 Current and voltage waveform of auxiliary diode D_2..... 87

3.9 Drive efficiency Vs. switching frequency 99

3.10 Switching losses Vs. switching frequency 99

3.11 Switching losses Vs. resonant capacitance..... 100

3.12 Switching losses Vs. resonant inductance 100

3.13 Optimum resonant capacitance Vs. optimum resonant inductance..... 101

4.1 Magnet configuration of an axial gap machine..... 108

4.2 The plot of $U_p(mR_o)$ for $p=6$, $R_i=4.17$ and $R_o=5.50$ for $m=0^+$ *to* 100..... 114

4.3 Variation of z-direction flux density, B_z, along the center of magnet face.... 121

4.4 Variation of radial flux density, $B_{r,}$, along the center of magnet face..... 122

4.5 Variation of angular flux density, B_{θ}, along the center of magnet face..... 123

4.6 Measured resultant flux density along the center of the magnet face..... 124

5.1 Equivalent per phase diagram with core loss resistor..... 126

5.2 Equivalent phasor diagram in d^e-q^e frame with core loss accounted..... 127

5.3 Modified d^e-q^e equivalent circuit of the machine..... 130

5.4 d^e-q^e equivalent circuit when core losses are neglected..... 130

5.5 d^e-q^e , d^s-q^s , a-b-c axes for the permanent magnet machine..... 135

5.6 Typical magnetization characteristic curve..... 138

5.7 Phase winding connection configuration at the machine start-up..... 139

5.8 Two possibilities of the initial rotor position..... 139

5.9 Inverter control block diagram and switching configuration for initial rotor position estimation..... 142

5.10 The functional block diagram and truth table for SPDT switch..... 143

5.11 Inverter control block diagram and switching configuration for normal mode of operation of the drive system..... 144

5.12 Vector control block diagram of the drive system with estimation algorithm..... 149

5.13 Flow chart of the on-line parameter identification scheme and estimation algorithm..... 150

5.14 SIMNON modules used in the simulations study..... 151

5.15 Estimated and actual unit vectors..... 153

5.16 Phase reference currents and actual motor phase currents generated using estimated rotor position..... 154

5.17 Actual and estimated rotor speed..... 155

CHAPTER 1

INTRODUCTION

1.1 Power Electronics and Adjustable Speed Drives

The basic principles of machine design and operation evolved nearly a century ago, but major developments and advancements in these areas still continue to appear at a steady rate. A rapid development of electric drives began after the invention of electro magnetic principles in 1866 [1] and of the asynchronous machine in 1869 [1]. The demand for drives was first characterized by constant speed and torque. Soon, a major thrust for variable speed/torque applications emerged.

With the invention of semiconductor power devices in the 1960s, rapid development began in the field of AC and DC drives. Modern power electronics has advanced at an enormous rate during the last few decades lending to the development of a new generation of electric machines and adjustable speed drives. This evolution has been possible due to technological advances in fields such as converter topologies, control techniques, microprocessors and digital signal processors, in addition to power electronics devices. With the development of solid state electric drives, machine design engineers are no longer limited to fixed frequency operation and are no longer constrained to use DC machines or wound-rotor machines with inefficient control strategies for variable speed/ torque applications.

The next decade promises to be an exciting period as more and more sophisticated adjustable speed drives fully penetrate the industrial applications area.

Although a variety of DC and AC adjustable speed drives are readily available as off-the shelf products, the dominant technologies and products of the future will be those that are inherently simple, robust, light weight, low cost and efficient.

To a certain extent, however the cost reduction and performance enhancements of the converter were made possible by new advancements in microcomputer control technology, VLSI circuits and the introduction of new solid state power devices such as Insulated Gate Bipolar Transistors (IGBT). But, the advancement of machine performance has so far not been comparable with those enhancements. During the next decade more and more efficient power converters are expected to penetrate the industrial applications arena and therefore, a larger role for adjustable speed drives and a large demand for more efficient and simple machinery is expected.

The permanent magnet synchronous machine is a viable candidate for most industrial applications due to its distinct advantages such as efficiency, specific weight and easy controllability, over the induction machine [2]. Permanent magnet synchronous machines are now being used in a wide range of industrial applications which include machine tools, robotics, aerospace generators, actuators and the promising field of electric vehicle propulsion. The development of high performance magnets such as Samarium-Cobalt and Neodymimum-Iron-Boron have made it possible to have superior power densities, high torque-to-inertia ratios and very high efficiencies with compared to an induction or conventional DC machine. The permanent magnet synchronous machine has two broad classifications according to it's field configurations: radial field machines

and axial field machines [3]. Axial field machines are different from radial field machines in many respects and have distinct advantages over them. The permanent magnet synchronous machine can further be classified into two broad classifications according to its generator back emf waveform: sinusoidal and trapezoidal (electronically commutated) machines [4]. In a sinusoidal back emf machine (PMSM), the stator windings are distributed and therefore the induced voltage in the stator has a sinusoidal variation. This type of machine is somewhat expensive compared to the trapezoidal version. To obtain a non-zero torque from a sinusoidal machine, the stator phase currents must be a balanced function of the rotor electrical angular position with a sinusoidal variation. For PMSMs, the classical solution includes two or three independent phase current regulating loops, which reference to the desired waveform. Therefore, the machine is essentially controlled with the currents. In a trapezoidal machine, known as brushless dc machine (BDCM), the stator windings are concentrated (one slot per pole per phase) and therefore, characterized by a three phase trapezoidal waveform in the stator. For a BDCM, current control is not compulsory. In a three phase BDCM, two out of three phases are pulse with modulated (PWM) in relation with the position of the rotor [3]. There are six possible 60-electrical degree stages. Hence, such a system is equivalent to a configuration of six successive four quadrant DC chopper. Only one current loop is necessary to control the torque in three phase BDCM, and it is similar to the control of a DC machine. Therefore, the BDCM control strategy is much simpler and cost effective [5]. This research work is concentrated on design optimization and further performance enhancement of axial gap

permanent magnet synchronous machine drives with special emphasis in the trapezoidal back emf permanent magnet synchronous machine (BDCM) configuration.

1.2 Axial Gap Permanent Magnet Synchronous Machines

Axial field permanent magnet synchronous machines offer an alternative to the conventional radial field machines. In axial field machines, as the name implies, the air gap flux is in the axial direction and the active current carrying conductors are radially positioned as opposed to the conventional radial field machine. The special features, such as its planar adjustable air gap, high torque-to-inertia ratio, high power density, efficient utilization of the rotor, easy cooling arrangements, easy rotor construction, relatively easy windability due to open and flat stator configuration, enable axial field machines to have distinct advantages over the conventional machines [6]. Some of these advantages are precisely the requirements of the emerging robotics, electric vehicle propulsion and high performance adjustable speed drives.

1.3 Comparative Study for Axial Gap Permanent Magnet and Axial Gap Induction Machines.

To understand the advantages that the axial gap permanent magnet synchronous machine has over the axial gap induction machine, a classical design program for axial gap induction machine was also developed. The study was based on 100-500 Hp machines running at a rated speed of 1800 rpm [7]. Machines were designed for a dc link voltage of 600 Volts. Fig 1.1 - Fig. 1.4 show the comparison between important parameters

of the two designs for a single stator configuration. The efficiency vs. Hp curve clearly shows that the efficiency of the induction machine lies in the lower 90%s whereas that of the permanent magnet synchronous machine is above 95%. Specific power of the PMSM is about twice that of the induction machine.

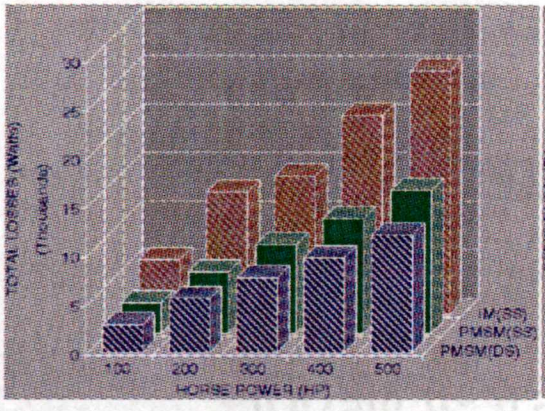


Fig. 1.1 Total power loss comparison

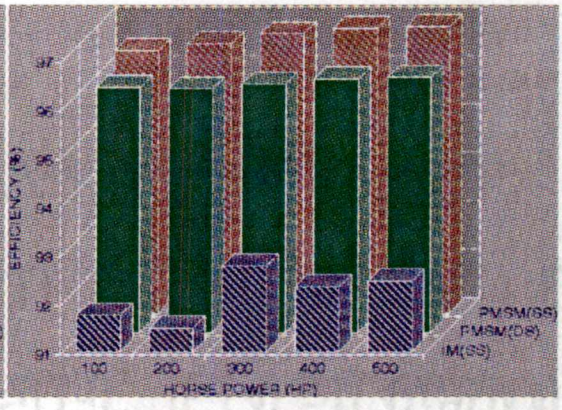


Fig. 1.2 Efficiency comparison

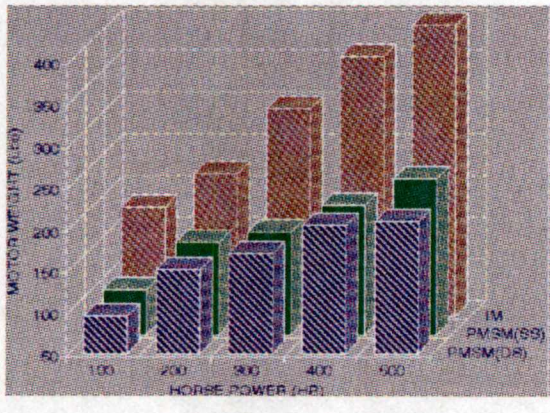


Fig. 1.3 Motor weight comparison

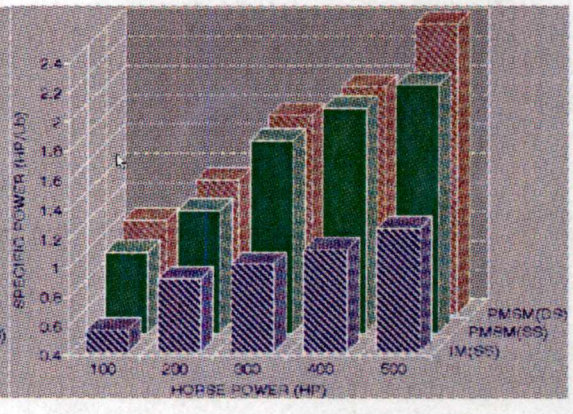


Fig. 1.4 Specific weight comparison

CHAPTER 2

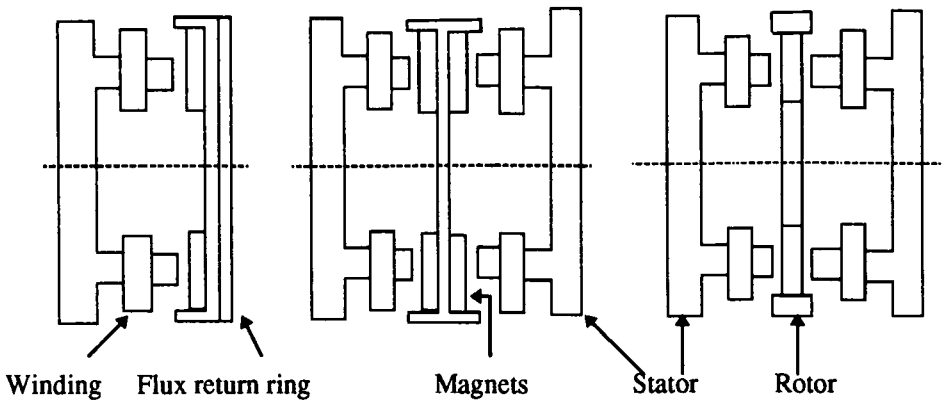
DESIGN OF AXIAL GAP PERMANENT MAGNET SYNCHRONOUS MACHINES

2.1 Introduction

The axial gap permanent magnet synchronous machines can be constructed in different configurations [6]. Depending on the configuration, as shown in Fig. 2.1, they can be classified as follows:

1. Single rotor and single stator (single air gap)
2. Single rotor sandwiched between two stators with magnets on both sides (double air gap)
3. Single rotor sandwiched between two stators with a single set of magnets being the field source for both air gaps (double air gap)
4. Single stator sandwiched between two rotors (double air gap , single sided rotor)
5. A variety of stators and rotors (multiple air gap)

One major drawback of the single air gap configuration is the strong axial magnetic pull between the stator and the rotor. This extra parameter must be taken into account in the mechanical design of the single air gap motor. The magnitude of this axial force is given by equation (2.1) [8].



(a) Single air gap (b) Double air gap (c)Double air gap

Fig. 2.1 Axial gap permanent magnet machine configurations.

$$F_a = \frac{1}{2}.\left(\frac{B_g^2}{\mu_0} - \mu_0.J_w\right) \qquad \text{N/m}^2 \qquad (2.1)$$

Where F_a = Axial force

B_g = Resultant air gap flux density

J_w = Stator winding current density

μ_0 = Permeability of free space

This drawback can be overcome by using a thrust bearing or by using an iron-less rotor disc and a magnetic flux return ring located on the opposite side of the rotor. The double stator arrangement eliminates the flux return ring on the rotor and, therefore, reduces the overall volume [9]. In double- stator , single-rotor configuration stator cores face each other with the rotor sandwiched between them [10]. The magnetomotive force (mmf) set up by each stator rotates in the same direction. The two stator windings can be connected either in series or in parallel. If the windings are connected in series, one stator may be

rotated by half to one slot pitch to reduce the slot ripple, cogging torque and space harmonics. If the stator windings are connected in parallel, care must be taken to align the stator slots properly in order to avoid high circulating currents. The rotor consists of a magnetic steel material disc or aluminum disc with a supporting outer radius ring projecting in axial direction to hold the magnets against the radial forces. In the cases of single air gap or double air gaps with a single set of magnets, it may be necessary to fix the magnet in place with epoxy and have them banded with a non-conducting material. Designs that use conductive rings to hold the magnets to rotor have been demonstrated to be ill-suited for inverter operation due to high harmonic contents [3]. The double air gap configuration with magnets on both sides of the rotor, lend itself to hold the magnets together and results in a simple rotor construction.

2.2 Classical Design Approach

This section discusses the effect of each design parameter selection on machine performance.

2.2.1 Stator Construction

Similar to the radial air gap construction, axial gap could have different types of stator configurations. One configuration is for the stator of an axial gap machine to have a slotless configuration. In this type of construction, the stator windings are systematically placed on the stator back iron and fixed to the core using an epoxy resin. This

construction exhibits no cogging torque due to the elimination of the cogging reluctance torque. Electric loading could also be increased due to the additional space available for copper. However, the lack of teeth makes the effective air gap larger; therefore to maintain a reasonable air gap flux density, magnet thickness should be substantially higher. Increasing the magnet thickness results in a smaller machine inductance due to the large air gap. Fig. 2.2 shows the slotted stator, which is the most commonly used configuration [8]. Fig. 2.3 shows the detail picture of the slot configuration. The number of stator slots and slot dimensions shown in Fig. 2.3, should be given a thoughtful consideration during the design process, since these parameters have a great influence on the overall drive system performance.

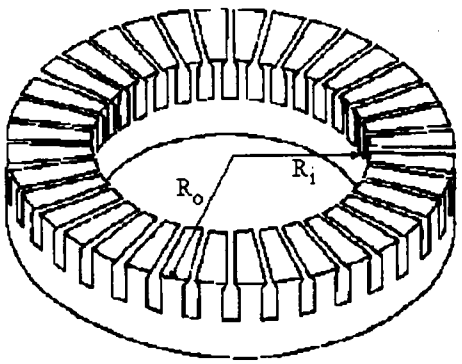


Fig. 2.2 Slotted stator of an axial gap machine

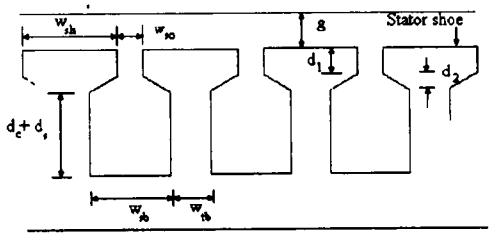


Fig. 2.3 Stator slot configuration

2.2.2 Cogging Torque Consideration

The number of stator slots, the shape of the stator slot opening and rotor magnets have remarkable effects on the motor drive characteristics. These same design parameters are strongly related to motor cogging torque (T_c), which is the most unwanted parasitic

element in permanent magnet motor drives. In permanent magnet motors, air gap permeance is non-uniform due to the shape of the stator slots and rotor magnets, the eccentricity of the stator and the rotor, and the saturation of the teeth [8]. These cause the air gap flux waveform to pulsate, which results in undesirable motor cogging torque. This effect can be minimized by proper selection of the number of stator slots and the slot configuration. In contrast to this, by slanting the slot edges with respect to the magnet (or vice versa), the air gap permeance can be minimized to lower cogging torque. This introduces another design parameter known as the skewing factor (K_s) into the design equations, which is discussed in detail in a latter section. The significance of these parameters and design configurations are briefly discussed in the following section.

2.2.3 Number of Stator slot /pole/phase is 1

Machine design with one slot/pole/phase with a concentrated winding is commonly seen in practice due to its simplicity and cost effectiveness. This configuration results in a back emf with a trapezoidal like waveform. However, in such a slot configuration the rotor magnets are at the same relative position with respect to the stator teeth. This implies that the cogging torque produced by each magnet is in phase. Therefore, the total cogging torque is given by the summation of the individual cogging torques and the net result is higher torque ripple, due to cogging in the drive system. This configuration has the additional advantage of a high electric loading capability compared to the multiple slots/pole/phase, because of the larger available slot area.

2.2.4 Number of Stator slot/pole/phase is Less Than 1 (Fractional)

This configuration can be used in machines where the number of poles is high. Unlike the single slot/pole/phase configuration, the cogging torque generated by each magnet is not in phase and results in a lower torque ripple due to cogging. Two examples of this type of configuration may be a 3-phase, 14-pole machine with 12 slots or a 5-phase, 22-pole machine with 20 slots. This kind of multipole structure also minimizes the magnetic yoke, resulting in the reduction of motor weight and core losses. This is a very attractive feature for a electric vehicle propulsion motor.

2.2.5 Number of Stator slot/pole/phase is Greater Than 1

(Fractional or Integral)

This configuration is widely used when the back emf distribution is sinusoidal rather than trapezoidal. In such a configuration the harmonic contents of the back emf is reduced. However, as the number of slots increases, the size of the slot decreases, resulting in a lower electrical loading capability. It also increases the amount of copper wire used and hence the copper losses. A fractional number of slot/pole/phase has the advantage of having a lower cogging torque compared to the integral number of slots /pole/phase.

2.2.6 Stator Slot Configuration

The stator slot configuration may be either semi-closed slot, as shown in Fig. 2.3, or open slot in which the two parameters d_1 and d_2, shown in Fig. 2.3, become zero. Slot leakage inductance for open and semi-closed configurations are given by equations (2.2) and (2.3) respectively [8].

$$L_{so} = n_s^2 . \frac{\mu_o . (d_c + d_s) . (R_o - R_i)}{3 . W_{sb}} \tag{2.2}$$

$$L_{ssc} = n_s^2 . \mu_o . \left(\frac{(d_c + d_s)}{3 . W_{sb}} + \frac{d_1}{W_{so}} + \frac{d_2}{(W_{so} + W_{sb})/2} \right) . (R_o - R_i) \tag{2.3}$$

where n_s = Number of turns in the slot

d_c = Slot depth

d_s = Slot insulation thickness

W_{sb} = Slot width at base

W_{so} = Slot opening

R_i = Stator inner radius

R_o = Stator outer radius

These equations show that the slot leakage inductance for the semi-closed version is higher due to two additional terms. This is a trade-off and it must be carefully designed with consideration given to the limitation of the machine inductance, depicted by the control strategy in the drive system. Open-slot configuration exhibits a higher

cogging torque compared to semi-closed slot due to the saliency effect and a larger effective air gap length [10]. Equation (2.4) gives an expression for the effective air gap.

$$g_e = K_c g = \frac{W_{sb} + W_{tb}}{(W_{sb} + W_{tb}) - \frac{2.W_{so}}{\pi}\left\{Tan^{-1}\left(\frac{W_{so}}{2.g}\right) - \frac{g}{W_{so}}\log_e\left(1+\frac{W_{so}}{2.g}\right)^2\right\}} g \qquad (2.4)$$

where K_c = Carter's coefficient

g = Actual air gap length

g_e = Effective air gap length

W_{tb} = Tooth width at base

The effect of cogging torque can be lowered by having wider stator shoes. However, a very low value of slot opening will result in undesirable shoe tip saturation and hence they appear as air, neutralizing the idea of uniform permeance over the air gap periphery. The designer can increase the leakage inductance by increasing the ratio of $\frac{d_1}{W_{so}}$ [equation (2.3)] , at the risk of shoe tip saturation, since the flux density at shoe tip is also inversely proportional to slot opening . The maximum flux density at the shoe tip, B_{st} , is given by equation (2.5) [8].

$$B_{st} = \frac{\mu_o n_s}{W_{so}} i \qquad (2.5)$$

where i = Total slot current.

2.2.7 Rotor Construction

Axial gap machines can have the following rotor types according to the number of air gaps within the machine [6].

(i) Single air gap with magnets on one side and a flux return ring on the back of the rotor as shown in Fig. 2.1a.

(ii) Double air gaps with magnets on both sides of the rotor as shown in Fig. 2.1b.

(iii) Double air gaps with a single set of magnets being the flux source for both air gaps as shown in Fig. 2.1c.

The two air gap configuration has the advantage of neutralizing a net axial force, which is given by equation (2.1), on the bearings. Having a magnetic flux return ring as shown in Fig. 2.1a will help to reduce this unbalanced force on the bearing. The flat shape of the rotor makes it possible to have a high pole pitch. This can result in a higher flux linkage and hence a high torque capability. However, having a very high pitch factor, increases the cogging torque effects. This is due to the high rate of change of magnetic flux near the magnet edges. Therefore, a pole pitch factor of 90-96% is considered as an acceptable design [8]. Rotor magnets can also be skewed to reduce the effect of cogging torque. In the axial gap version, the torque is proportional to the square of the radius and hence linear skewing does not eliminate the cogging torque, like in a radial configuration. Skewing the magnets increases the cost and reduces the total flux linked through the stator winding. This results in a reduction of generated back emf and hence the

performance. The skewing factors for a trapezoidal and sinusoidal machine are given by equations (2.6) and (2.7) respectively [8].

$$K_{st} = 1 - \frac{\theta_{se}}{2\pi} \tag{2.6}$$

$$K_{ss} = \frac{Sin(\theta_{se}/2)}{(\theta_{se}/2)} \tag{2.7}$$

where θ_{se} = Slot pitch in electrical degrees.

These equations show that the skewing can be used effectively without paying a higher penalty in the performance reduction when the slot count is high. The per phase equivalent circuit for a permanent magnet synchronous machine can be as shown in Fig. 2.4 [11]. The torque developed can be represented by equation (2.8) [11]. Having a thicker magnet increases the value of I_m and lowers the inductance L_0. However, the net result would be an increase in the product $L_0 I_m$ [11] and hence an increase in torque capability for the same stator current I_s.

$$T_e = K.L_0.I_s I_m.Sin\beta \tag{2.8}$$

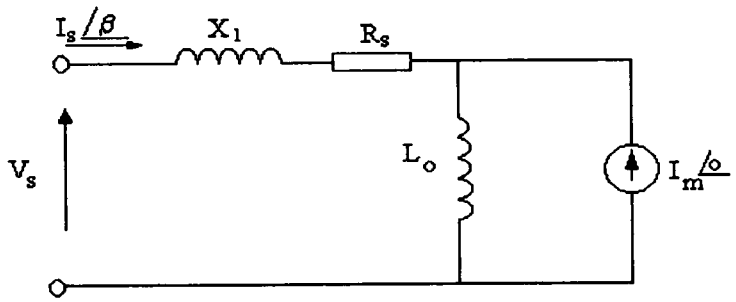


Fig. 2.4 Per phase equivalent circuit for a permanent magnet machine

2.2.8 Stator Winding Configuration

The stator winding configuration can either be full-pitched, short-pitched or over-pitched [8]. When the number of slots/pole/phase is an integer, the coil pitch is equal to the magnet pole pitch and the hence flux linked through the coil will be maximum. When the number of slots/pole/phase has a fractional component, the coil pitch can be made either less than or greater than the magnet pole pitch. Both configurations have the advantage of reducing the cogging torque and harmonics. However, in a short-pitched winding the maximum flux is not linked through the coil and there is a degree of performance reduction due to the lower back emf. The over-pitched configuration becomes very attractive in axial gap machines where the number of poles and the number of phase count is high. This configuration reduces the unwanted lengthy end-winding and therefore, the stator copper losses are reduced. In this type of configuration the number of slots/pole/phase is less than 1 and is shown in Fig. 2.5 and Fig. 2.6.

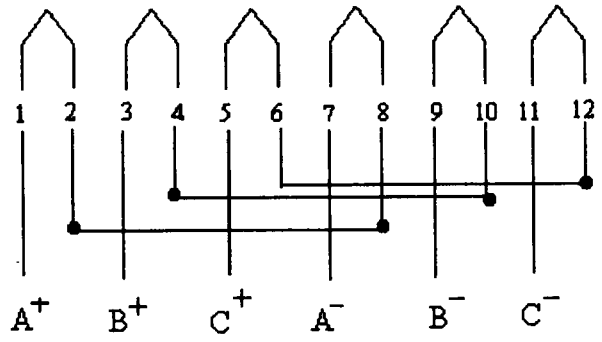


Fig 2.5 Over-pitched winding configuration for a three-phase machine with 14 poles and 12 slots.

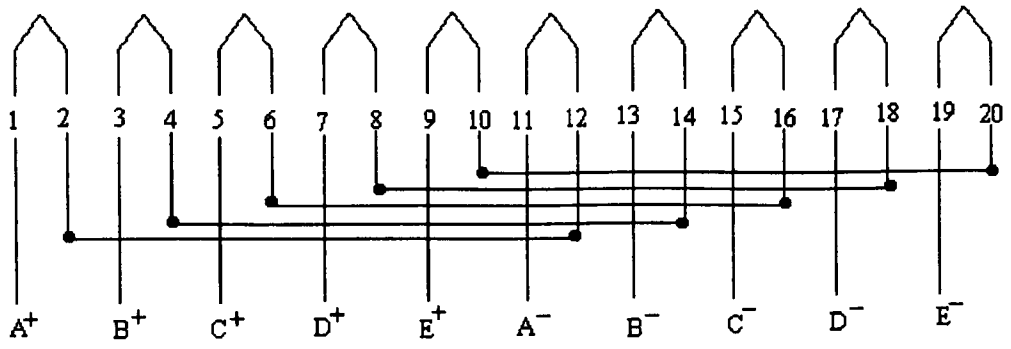


Fig 2.6 Over-pitched winding configuration for a five-phase machine with 22 poles and 20 slots.

2.2.9 Input Data Organization for the Design Problem

In this section the input data is categorized and organized in a logical way so that they can be used to design either trapezoidal back emf (BDCM) machines or sinusoidal back emf (PMSM) machines. In this approach , as shown in Table 2.1 the input data is grouped into seven categories.

2.2.10 Mathematical Formulation of Design Output Data

Given all the input data shown in Table 2.1, one must formulate the output design data, performance parameters and other mechanical parameters in terms of the input parameters. In this formulation, rated power, rated speed and rated voltage are set to their respective given values. If the design is for an adjustable speed drive application, then the maximum available DC link voltage can be set equal to the rated line to line voltage. The following formulations and equations are based on a double stator/dual air gap axial gap

Table 2.1 Input design data.

Parameter	Symbol	Units
1. Machine Ratings & Configuration:		
Rated power/stator	P	Hp
Rated speed	N_r	RPM
Rated voltage (L-L)	V	Volts
Number of magnet poles	N_{mp}	
Number of phases	N_{ph}	
Phase Wdg. connection configuration	Star or Delta	
2. Stator Data:		
Stator outer radius	R_o	Inch
Stator inner radius	R_i	Inch
Stator iron axial thickness	T_{sa}	Inch
Stator lamination thickness	t	mils
3. Stator Winding Data:		
Number of parallel circuit/phase	N_p	
Number of parallel wires/conductor	N_w	
Number of conductors/slot	N_c	
Number of coil sides/slot	2	
Number of stator slots	N_s	
Number of slots/pole/phase	N_{spp}	
Winding distribution factor	K_d	
Winding pitch factor	K_p	
Winding factor	$K_w (K_d.K_p)$	
Wire AWG	A_{wg}	
Wire diameter	d_w	Inch
Wire resistance/1000 ft	r_{1000}	Ohms
Wire weight/1000 ft	w_{1000}	Lb
Number of wires per square inch	N_{si}	
Continuos current rating	I_r	Amps
Coil extension at inner radius	L_{xi}	Inch
Coil extension at outer radius	L_{xo}	Inch
4. Slot Geometry Data:		
Stator slot tip depth	d_1	mils
Stator slot wedge depth	d_2	mils
Space between two coil sides	d_c	mils
Stator average slot opening factor	S_{of} ($=W_{so}/W_{sb}$; $0.1<S_{of}<1$)	
Stator slot width mult. factor	S_{wm} ($1.0<S_{wm}<1.75$)	
Slot fill factor	S_{fi}	
Slot insulation thickness	S_{in}	mils
5. Magnet and Air Gap data:		
Magnet axial thickness	T_{ma}	Inch

Magnet remanence	B_r	Tesla
Magnet recoil permeability	m_r	
Magnet spacer thickness	t_{ms}	Inch
Air gap	g	mils
6. Other Data:		
Shaft diameter	d_{sh}	Inch
Shaft axial extension	L_{ex}	Inch
Rotor steel thickness	t_{rs}	Inch
Rotor outer ring thickness	t_{ri}	Inch
Rotor steel density	r_r	lb/in^3
Stator steel density	r_s	lb/in^3
Magnetic material density	r_m	lb/in^3
Eddy current const. for lamination	k_e	
Hysteresis const. for laminations	k_h	
Hysteresis exponent coefficient	k_{ex}	
7. Material Cost:		
Magnet material	C_{mt}	$/lb
Magnetic steel (Stator Material)	C_{st}	$/lb
Rotor steel	C_{rt}	$/lb
Copper	C_{cu}	$/lb

configuration as shown in Fig. 2.1b. These equations can easily be modified to suit to other configurations as shown in Fig. 2.1a and Fig. 2.1c or any other multiple stator/rotor configuration.

$$* \text{ Torque} = T_e = \frac{5252P}{N_r} \quad \text{(Ft-Lb)} \tag{2.9}$$

$$* \text{ Active radial length} = R_{al} = R_o - R_i \text{ (In)} \tag{2.10}$$

$$* \text{ Tooth width @ inside radius} = W_{tb} = \left(\frac{\pi R_i}{N_{ph} N_{mp} N_{spp}}\right)(2 - S_{wm}) \quad \text{(In)} \tag{2.11}$$

$$* \text{ Shoe width @ inside radius} = W_{sh} = \left(\frac{\pi R_i}{N_{ph} N_{mp} N_{spp}}\right)(2 - S_{of} S_{wm}) \quad \text{(In)} \tag{2.12}$$

$$* \text{ Slot width @ inside radius} = W_{sb} = \left(\frac{\pi R_i}{N_{ph} N_{mp} N_{spp}}\right).S_{wm} \quad \text{(In)} \tag{2.13}$$

$$* \text{ Slot opening @ inside radius} = W_{so} = W_{sb}.S_{of} \quad \text{(In)} \tag{2.14}$$

$$* \text{ Carter's coefficient} = K_c$$

$$K_c = \frac{W_{sb} + W_{tb}}{(W_{sb} + W_{tb}) - \frac{2.W_{so}}{\pi}\left\{Tan^{-1}\left(\frac{W_{so}}{2.g}\right) - \frac{g}{W_{so}}\log_e\left(1 + \frac{W_{so}}{2.g}\right)^2\right\}} \tag{2.15}$$

$$* \text{ Effective gap length} = g_e = K_c.g \quad \text{(mm)} \tag{2.16}$$

$$* \text{ Area of magnet/Area of gap} = A_{mg} = \frac{\left(2\pi R_i - N_{mp}\tau_{ms}\right)}{2\pi R_i} \tag{2.17}$$

* B_{gap} at stator iron surface $= B_g = \dfrac{B_r A_{mg}}{\left(1 + g_e \mu_r A_{mg} / T_{ma} 25.4\right)}$ (T) (2.18)

* Peak flux per pole $= \phi_m = B_g . \pi . \left(R_o^2 - R_i^2\right)$ (mV/sec) (2.19)

* Max B_t at inside radius $= B_{tm} = \left(\dfrac{W_{tb} + W_{sb}}{W_{tb}}\right) B_g$ (T) (2.20)

* Required slot area $= A_s = \left(\dfrac{N_w N_c}{N_{si} S_{fl}}\right).$ (in^2) (2.21)

* Required slot depth $= d_s = \dfrac{A_s}{\left(W_{sb} - 2S_{in} 0.001\right)} + \left(S_{in} + d_c\right) 0.001$ (In) (2.22)

* Max B_y at stator yoke $= B_{ym} = \dfrac{B_g . \pi . R_o}{\left(N_{mp}\left(T_{sa} - \left(d_s + \left(d_1 + d_2\right) 0.001\right)\right)\right)}$ (T) (2.23)

* Phase current $= I_{ph} = \dfrac{2 . N_p . T_e . 10^6}{\left(\left(N_{ph} - 1\right) . N_{mp} N_c B_g \left(R_o^2 - R_i^2\right)\left(25.4\right)^2\right)}$ (A) (2.24)

* Winding current density $= J_d = \dfrac{I_{ph}}{\left(N_p N_w \left(\dfrac{\pi}{4}\right) d_w^2\right)}$ (A/In^2) (2.25)

* Line to line back emf $= V_L = \dfrac{N_{mp} N_c B_g \left(R_o^2 - R_i^2\right) \omega_m}{\left(N_p 10^6\right)} K_w K_s$ (Volt) (2.26)

* Mean length/turn $= L_{mt} = 2\left(R_{al} + L_{xi} + L_{xo}\right) + \pi Sin\left(\dfrac{\pi}{N_{mp}}\right)\left(R_o + R_i\right)$ (In) (2.27)

* Phase resistance $= R_s = \dfrac{N_c L_{mt} N_{mp} r_{1000}}{\left(24 N_w . N_p^2\right)} N_{spp}$ (mOhm) (2.28)

The phase inductance consists of three main components due to the air gap, slots and end turns [8]. Therefore, they are calculated separately and then added together to give the value for phase inductance.

The air gap inductance, L_g is given by:

$$* \text{ Air gap inductance} = L_g = \frac{N_c^2 4\pi.10^{-7}\pi\left(R_o^2 - R_i^2\right)A_{mg}}{N_p^2\left(T_{ma} + \mu_r g_e\right)} \quad \text{(H)} \tag{2.29}$$

Fig. 2.7 shows the stator slot configuration with a double layer winding. By calculating the specific slot permeance of coils due to self and mutual flux linkages of the coils, an expression for the slot leakage inductance can be obtained as follows.

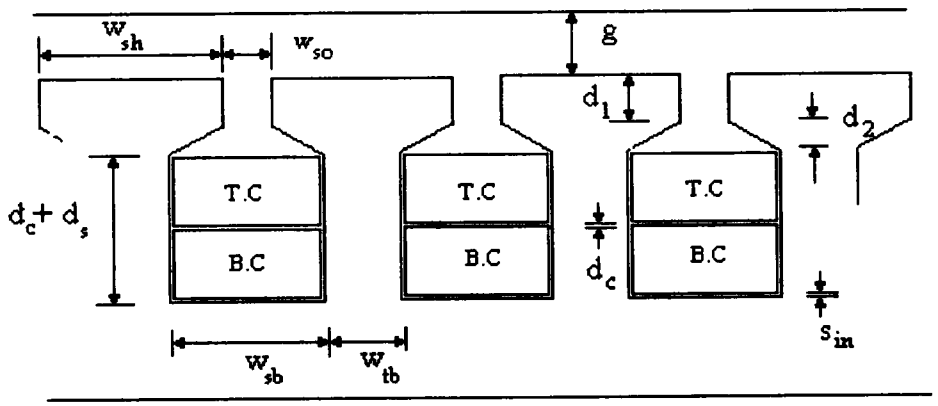


Fig. 2.7 Stator slot configuration with a double layer winding.

* Specific slot permeance of top coil side = P_t

$$P_t = \mu_o\left\{\frac{(d_s - d_c - S_{in}).0.5}{3.W_{sb}} + \frac{d_1}{W_{so}} + \frac{d_2}{(W_{sb} - W_{so})}\ln\left(\frac{W_{sb}}{W_{so}}\right)\right\} \tag{2.30}$$

* Specific slot permeance of bottom coil side = P_b

$$P_b = \mu_o \left\{ \frac{(2.d_s - d_c - 2S_{in}).2}{3.W_{sb}} + \frac{d_1}{W_{so}} + \frac{d_2}{(W_{sb} - W_{so})} \ln\left(\frac{W_{sb}}{W_{so}}\right) \right\} \quad (2.31)$$

* Specific slot permeance due to mutual flux linkages = P_{tb}

$$P_{tb} = \mu_o \left\{ \frac{(d_s - d_c - S_{in}).0.5}{2.W_{sb}} + \frac{d_1}{W_{so}} + \frac{d_2}{(W_{sb} - W_{so})} \ln\left(\frac{W_{sb}}{W_{so}}\right) \right\} \quad (2.32)$$

Total specific slot permeance = $P_{to} = P_t + 2.P_{tb} + P_b$ (2.33)

* Slot leakage inductance [ ], L_{sl} , is then given by

$$L_{sl} = \frac{N_{mp} N_c^2}{N_{ph} N_p^2} \frac{P_{to}}{4} L_{al} 10^{-8} \quad \text{(H)} \quad (2.34)$$

* End winding leakage inductance [64], L_{ew} , is given by

$$L_{ew} = \frac{N_{mp} \left(N_c K_p K_d\right)^2 4\pi 1.2 \left[(L_{xi} + L_{xo}) + 0.5 \left(1 - Cos\left(\frac{\pi}{N_{mp}}\right)\right)(R_o + R_i + L_{xo} - L_{xi}) \right]}{N_{ph} N_p^2 10^8} \quad (2.35)$$

* Phase inductance = $L_s = L_g + L_{sl} + L_{ew}$ (2.36)

2.2.11 Derivation of Performance Parameters

Performance parameters which describe the machine's operation fall into two separate classes: attributes and characteristics. Attributes are the parameters that are always to be maximized or minimized to ensure that the optimum design configuration and optimum performance during the operation is obtained. Machine efficiency, mass (or specific power), cost are the most important attributes. Therefore, these parameters are obtained in terms of input /output design parameters and considered in detail.

* Stator teeth volume $= V_{th}$

$$V_{th} = (R_o - R_i)((d_s(\pi(R_o + R_i) - N_{ph}N_{mp}N_{sppp}W_{sb})) + (((W_{sh}.d_1) + (W_{sh} + W_{tb})\frac{d_2}{2})0.001)N_{ph}N_{mp}N_{spp})) \quad (\text{in}^3) \qquad (2.37)$$

* Stator back iron volume $= V_{bi}$

$$V_{bi} = \pi(R_o^2 - R_i^2)(T_{sa}.25.4 - (d_s + (d_1 + d_2)0.001)) \quad (\text{in}^3) \qquad (2.38)$$

* Stator iron volume $= V_{st} = V_{th} + V_{bi}$ (in^3) (2.39)

* Weight of the stators $= W_{st} = 2V_{st}\rho_s$ (lb) (2.40)

* Magnet weight $= W_{mg} = 2\rho_m(R_o^2 - R_i^2)\pi T_{ma}$ (lb) (2.41)

* Wire weight $= W_{wr} = \dfrac{2N_{ph}N_{mp}N_wN_cN_{spp}W_{1000}L_{mt}}{(48000)}$ (lb) (2.42)

* Rotor steel weight $= W_{rt}$

$$W_{rt} = [\pi.d_{sh}^2 0.5((T_{ma} + T_{sa}) + L_{ex}) + 2\pi(R_o + \frac{t_{ri}}{2})t_{ri}((2T_{ma} + t_{rs})) + \pi.(R_o^2 - R_i^2)t_{rs}]\rho_r \quad (\text{lb}) \qquad (2.43)$$

* Total active material weight $= W_T$

$$W_T = W_{st} + W_{mg} + W_{wr} + W_{rt} \quad (\text{lb}) \qquad (2.44)$$

* Specific power $= S_P = \dfrac{2.P}{W_T}$ (Hp/lb) (2.45)

* Total active material cost $= C_t$

$$C_t = W_{st}C_{st} + W_{mg}C_{mt} + W_{wr}C_{cu} + W_{rt}C_{rt} \quad (\$) \qquad (2.46)$$

From the equations (2.37) to (2.46), it is obvious that the specific power and cost attributes are highly non-linear functions of the input/output parameters. The other important attribute is the machine efficiency and is calculated assuming negligible stray, friction and windage losses in the machine.

2.2.12 Stator Copper and Core Loss Calculations

* Stator copper losses at rated speed = $P_{rl} = \left(N_{ph} - 1\right) I_{ph}^2 R_s$ (W) (2.47)

In order to calculate the stator core losses, the stator is divided into small radial sections and each section's flux density was estimated. Those values are then used to calculate the eddy current and hysteresis losses in each small sections [12]. All of the losses then can be added to give a more accurate representation of the stator core losses. Accuracy of the results depends on the number of sections to which the stator has been divided. Assuming that the active radial length is divided into N number of radial sections, the following equations can be obtained.

* Radial length of a small radial section $\Delta r = \dfrac{\left(R_o - R_i\right)}{N}$ (in) (2.48)

* Average radius of nth small radial section $R_n = R_i + \left(n - 0.5\right)\Delta r$ (in) (2.49)

* Tooth area in nth small section $\Delta A_n = 2\pi R_n \Delta r \dfrac{W_{tb}}{\left(W_{tb} + W_{sb}\right)}$ (in^2) (2.50)

* Tooth flux density in nth small radial section $B_{tn} = \dfrac{B_g 2R_n}{\left(2.R_n - R_i\right)}$ (T) (2.51)

* Yoke flux density in n[th] small section $B_{yn} = \dfrac{\pi R_n B_g}{N_{mp}(T_{at} - d_s - d_1 - d_c)}$ (2.52)

* Tooth eddy current loss per lb. $P_{ek} = 2k_e N_{ph}\left(N_{mp}\omega_m \dfrac{B_{tn}}{\pi}\right)^2$ (2.53)

* Yoke eddy current loss per lb, $P_{ek}^1 = 2k_e N_{ph}\left(N_{mp}\omega_m \dfrac{B_{yn}}{\pi}\right)^2$ (2.54)

* Tooth hysteresis loss per lb, $P_{hk} = k_h N_{mp}\omega_m B_{tn}^{\frac{k_{ex}}{2}}$ (2.55)

* Yoke hysteresis loss per lb, $P_{hk}^1 = k_h N_{mp}\omega_m B_{tyn}^{\frac{k_{ex}}{2}}$ (2.56)

where k_{ex} is the stator magnetic material's exponential coefficient.

* Total tooth eddy current losses, $P_{ten} = P_{ek}\rho_s \Delta A_n(d_1 + d_2 + d_s)$ (2.57)

* Total yoke eddy current loss, $P_{yen} = P_{ek}^1 \rho_s \Delta A_n(T_{at} - d_1 - d_2 - d_s)$ (2.58)

* Total tooth hysteresis losses, $P_{thn} = \rho_s P_{hk} \Delta A_n(d_1 + d_2 + d_s)$ (2.59)

* Total yoke hysteresis losses, $P_{yhn} = \rho_s P_{hk}^1 \Delta A_n(T_{at} - d_1 - d_2 - d_s)$ (2.60)

* Efficiency at rated speed, $\eta = \dfrac{100.P}{P + P_{rl} + \sum_N (P_{ten} + P_{yen} + P_{thn} + P_{yhn})}$ (2.61)

* Rotor Inertia, $J = \dfrac{1}{2}\left((W_{sh} d_{sh}^2 / 4) + W_{rt}(R_o^2 + R_i^2)\right)$ (Lb-Ft^2) (2.62)

2.2.13 Organization of the Classical Design Procedure

Once the input data is available as in section 2.2.3 and the output data and the performance parameters are obtained as functions of input parameters, they can be arranged in a systematic way, by using QPRO[1], as shown in Table 2.2 and Table 2.3. The design process assumes that the required rated power, rated speed and rated voltage are given so that they can be used as fixed design parameters. The design can be initiated with equal slot and tooth width and as the iteration process goes on, they can be changed by varying slot width multiplication factor, S_{wm} . The most sensitive design parameters, such as outer and inner radius, number of conductors per slot, number of magnet poles etc. are changed in order to get an acceptable design. Table 2.2 and Table 2.3 show design input parameters and design output parameters for one of the acceptable designs for a 100 Hp, 1800 RPM, 600 Volts brushless dc machine. The axial gap configuration has very low stray, friction and windage losses (less than 0.01 p.u) and these losses are neglected in efficiency calculation. As shown in column 2 of Table 2.3 the value of the specific power is 1.14 Hp/Lb. The values for the efficiency and the material cost are 95.57% and $1161 respectively. Table 2.4 shows how the motor efficiency varies in the torque-speed plane, while Fig. 2.8 shows the graphical representation of the data shown in Table 2.4.

[1] QPRO is a registered trademark of a spreadsheet software package by Borland International, Inc.

Table 2.2 Input design data for a 100Hp, 1800Rpm, 600 Volts BDCM

Parameter	Value	Units
1. Machine Ratings and Configuration:		
Rated power/stator	100	Hp
Rated speed	1800	RPM
Rated voltage (L-L)	600	Volts
No. of magnet poles	10	
No. of phases	3	
Phase winding connection config.	Star	
2. Stator Data:		
Stator outer radius	5.886	Inch
Stator inner radius	3.000	Inch
Stator iron axial thickness	1.800	Inch
Stator lamination thickness	14	mils
3. Stator Winding Data:		
No. of parallel circuit/phase	1	
No. of parallel wires/conductor	4	
No.of conductors/slot	12	
No. of coil sides/slot	2	
No. of stator slots	48	
No. of slots/pole/phase	1	
Winding distribution factor	1.00	
Winding pitch factor	1.00	
Winding factor	$1.00(K_d.K_p)$	
Wire AWG	18	
Wire diameter	0.0403	Inch
Wire resistance/1000 ft	6.61	Ohms
Wire weight/1000 ft	4.92	Lb
No. of wires per square inch	450	
Continuos current rating	5	Amps
Coil extension at inner radius	0.25	Inch
Coil extension at outer radius	0.25	Inch
4. Slot Geometry Data:		
Stator slot tip depth	35	mils
Stator slot wedge depth	43	mils
Space between two coil sides	60	mils
Stator average slot opening factor	0.70	
Stator slot width mult. factor	0.85	
Slot fill factor	0.60	
Slot insulation thickness	60	mils

5. Magnet and Air Gap data:		
Magnet axial thickness	0.35	Inch
Magnet remanence	1.10	Tesla
Magnet recoil permeability	1.05	
Magnet spacer thickness	0.063	Inch
Air gap	30	mils
6. Other Data:		
Shaft diameter	0.75	Inch
Rotor steel thickness	0.125	Inch
Rotor steel density	0.278	lb/in^3
Stator steel density	0.276	lb/in^3
Magnetic material density	0.273	lb/in^3
Eddy current constant for lamination	$9.30*10^{-3}$	
Hysteresis constant for laminations	$5.80*10^{-3}$	
Hysteresis exponent coefficient	1.93	

Table 2.3 Design output data and performance parameters.

Output Data and Performance Parameters	Value	Units
Torque	145.88	Ft-Lb.
Active radial length	2.89	Inch
Tooth width at inside radius	0.225	Inch
Shoe width at inside radius	0.276	Inch
Slot width at inside radius	0.167	Inch
Slot opening at inside radius	0.116	Inch
Carter's coefficient	1.15	
Effective gap length	34.6	mils
Area of magnet / Area of gap	0.95	
B_g at stator iron surface	0.949	Tesla
Peak flux per pole	0.08	mV-sec
B_t at inside radius	1.650	Tesla
Required slot area	0.178	in^2
Required slot deapth	1.169	in
B_y max at stator yoke	1.985	Tesla
Phase current	65.64	Amps
Slot current density	1071	A/in^2
Line to line back emf at rated speed	567.99	Volts
V_{l-l}+I.R drop+Inverter switch drop	593	Volts
Mean length per turn	11.22	Inch
Phase resistance	148.30	mOhm
Phase inductance	0.241	mH
Stator tooth volume	69.519	in^3
Stator back iron volume	44.49	in^3
Stator iron volume	114.01	in^3
Weight of the stators	62.93	Lb.
magnet weight	15.40	Lb.
Wire weight	5.30	Lb.
Rotor weight	19.55	Lb.
Total active material weight	87.77	Lb.
Specific power	1.14	Hp/Lb
Total active material cost	1161	$
I^2R loss at rated current	1278.03	Watts
Teeth loss at rated speed	304.17	Watts
Stator yoke loss at rated speed	147.57	Watts
Efficiency at rated speed and torque	95.57	%

Table 2.4 Efficiency in the torque-speed plane.

	Efficie.					
Speed/Rated speed Torque/Rated Torque	0.20	0.40	0.60	0.80	1.00	1.20
0.20	92.55	93.72	93.91	93.85	93.68	93.47
0.40	91.60	94.41	95.28	95.64	95.79	95.83
0.60	89.43	93.63	95.05	95.72	96.09	96.29
0.80	87.06	92.51	94.43	95.37	95.92	96.26
1.00	84.70	91.27	93.65	94.86	95.57	96.03
1.20	82.42	90.00	92.81	94.26	95.13	95.70

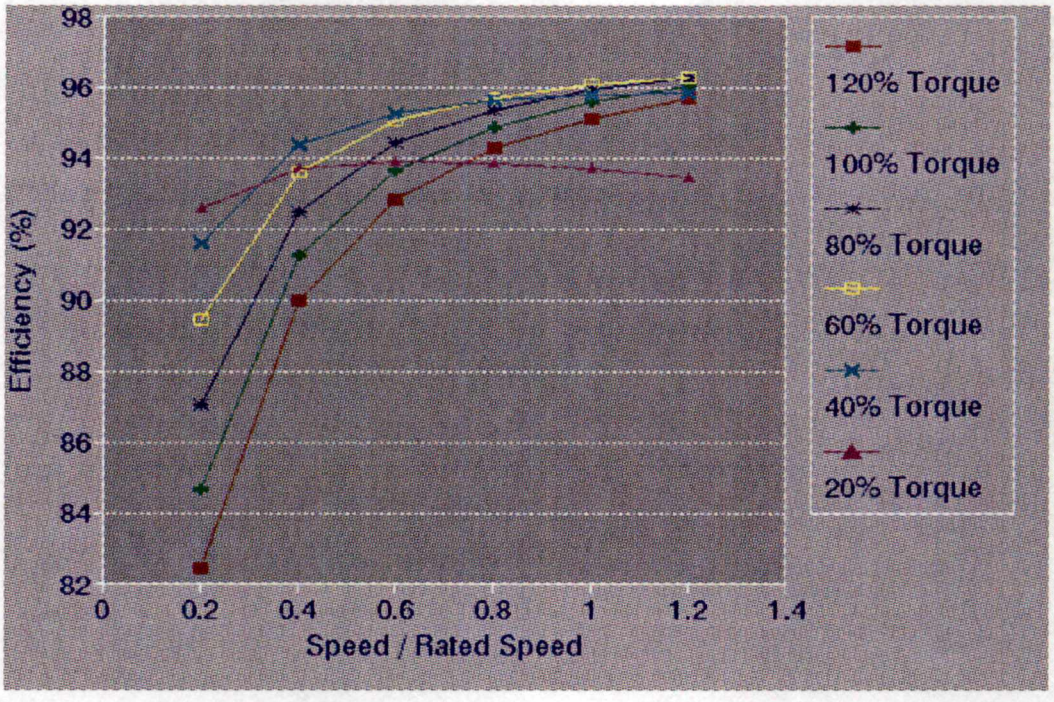


Fig. 2.8 Efficiency map in the Torque-Speed plane.

2.3 Specific Power Optimization with a Constraint on Efficiency

Modern power electronics has advanced at a tremendous rate, leading to the development of more efficient and compact adjustable speed drives. The development of new power electronics devices has made it possible to build light weight and efficient power converters and therefore, in most industrial speed drive applications, the electrical machine accounts for the most of the system weight. In some applications, such as in aerospace and in electric vehicle propulsion, it is very important to reduce the machine weight without loosing the machine performance characteristics. It is generally the intention of the machine designer to produce a design that optimizes the most important performance parameters such as efficiency, specific power, cost etc.. These performance parameters are unfortunately conflicting and therefore a certain amount of tradeoff is used in achieving a particular design. This can be resolved by formulating appropriate design constraints during the design process. In this section, a procedure to optimize the machine specific power (i.e. to minimize the machine weight) with a constraint placed on the efficiency is described.

2.3.1 Method of Optimization Using QPRO

As seen from the equations (2.37) to (2.45), the specific power is a highly non-linear function of the input design parameters. Therefore, in order to optimize the specific power a non-linear optimization procedure should be used. QPRO has built in linear and non-linear optimization algorithms. Because the machine design program is developed

using the cell based QPRO program, the same program can easily be used to find the optimum design parameters of the machine for any particular application.

There are two non-linear optimization algorithms available in QPRO. One method is the Quasi-Newton method which requires less computational work during the computation of search direction. The second method is the Newton-Conjugate method. This method needs more computational work during the search direction and may be helpful if the objective function is changing very slowly during the optimization. The initial estimates of the basic variables can be obtained by using either a tangent method or a quadratic method. The tangent method uses a linear extrapolation approach, while the quadratic method uses quadratic extrapolation approach. To estimate the partial derivatives, either a forward or a central differencing method can be used. Any of these options can be selected in the program before the search for a optimal solution is initiated.

Since the objective is to maximize the machine specific power (i.e. power/weight), it is necessary to program the specific power function, $F(S_p)$, which is a non-linear function of input design parameters and given by equation (2.45), into the solution cell and then specify the optimization problem as a maximization problem. Thus the objective function becomes:

$$Max\{F(S_p)\} \tag{2.63}$$

where $$F(S_p) = \frac{P}{(W_{st} + W_{mg} + W_{wr} + W_{rt})} \tag{2.64}$$

where W_{st} , W_{mg} , W_{wr} , W_{rt} are given by equations (2.40) to (2.43).

2.3.2 Variable Design Parameters

There are many unknown machine parameters involved in the design of an axial gap machine and they can be defined and programmed into the variable cells. Table 2.5 shows the design parameters and their status during the optimization process. All of the parameters shown as "variable" are allowed to adjust to reach an optimal solution.

Since the sensitivity of the specific power to the stator slot tip depth and wedge depth is negligible, they are considered as fixed variables. However, their most suitable values have to be determined by a magnetic circuit analysis, using finite element analysis, in order to make sure that tip saturation does not occur. In this method the wire size (AWG #) and corresponding data are also assumed to be fixed. The reason for this is discussed in the next section. They can also be considered as a variable during the optimization, if required.

2.3.3 Constraints on the Design Parameters

Constraints placed on the input design parameters and the output performance parameters depend on the specific design requirements of the customer. The constraints may either be equal, unequal or a range. Design parameter constraints are shown in table 2.6 for a general case and their values depend on the specific design application requirements.

Table 2.5 Status of the parameters during optimization.

Design Parameter	Status of the parameter
Magnet outer radius, R_o	Variable
Magnet inner radius, R_i	Variable
Magnet axial thickness, T_{ma}	Variable
Magnet remanence, B_r	Fixed
Magnet recoil permeability, μ_r	Fixed
Air gap, g	Variable
Stator iron axial thickness, T_{sa}	Variable
No. of phases, N_{ph}	Variable
No. of magnet poles, N_{mp}	Variable
No. of parallel circuit per phase, N_p	Variable
No. of parallel wires per conductor, N_w	Variable
No. of conductors per slot, N_c	Variable
Stator average slot opening factor, S_{of}	Variable
Stator slot width multiplication factor, S_{wm}	Variable
Stator slot tip depth, d_1	Fixed (can be variable)
Stator slot wedge depth, d_2	Fixed (can be variable)
Wire AWG #, A_{wg}	Fixed (can be variable)
Wire diameter, d_w	Fixed (can be variable)
Wire resistance per 1000 ft., r_{1000}	Fixed (can be variable)
Wires per square inch, N_{si}	Fixed (can be variable)
Wire weight per 1000 ft., w_{1000}	Fixed (can be variable)
Continuos current rating of the wire, I_r	Fixed (can be variable)

Table 2.6 Design parameter constraint table.

<= Constraints	= Constraints	>= Constraints
Stator outer radius , R_o	-----	-----
-----	-----	Inner radius, R_i
Magnet axial thickness, T_{ma}	-----	Magnet axial thickness, T_{ma}
-----	Magnet remanence, B_r	-----
-----	Magnet recoil permeability,m_r	-----
-----	-----	Air Gap , g
Stator axial thickness , T_{sa}	-----	-----
-----	No of poles , N_{mp} (Even #)	-----
-----	No. of par. ct./ Ph ,N_p(Integer)	-----
-----	No of cond./ slot, N_c (Integer)	
-----	No. of par w/ con. ,N_w (Integer)	-----
Slot opening factor , S_{of}	-----	Slot opening factor , S_{of}
Slot width mult. factor, S_{wm}	-----	Slot width mult. factor, S_{wm}
Stator. slot tip depth, d_1	-----	Stator. slot tip depth, d_1
Stator slot wedge depth, d_2	-----	Stator slot wedge deapth,d_2
B_{max} tooth (=< 2.0 Tesla)	-----	-----
B_{max} yoke (=< 2.0 Tesla)	-----	-----
Active radial length	-----	Active radial length
-----	B emf+ Ir drop+ Inv. sw. drop	-----
-----	-----	Efficiency, η (=> 94.00)
Cur. den. J_d (=<6452A/in^2)	-----	Cur. den. J_d (=>645 A/in^2)

2.3.4 Formulation of the Optimization Problem

Given the conditions discussed in sections 2.3.2 and 2.3.3, the optimization problem can be formulated. The optimization problem formulation given below is for the machine designed in section 2.2.13.

$$\text{Maximize}\left\{\frac{P}{W_{st}+W_{mg}+W_{wr}+W_{rt}}\right\} \tag{2.65}$$

where W_{st} , W_{mg} , W_{wr} and W_{rt} are given by equations (2.40) -(2.43).

Subject to constraints:

Outer radius,	$R_o \leq 6$	(2.66)
Inner radius,	$R_i \geq 3$	(2.67)
Magnet axial thickness,	$T_{ma} \geq 0.2$	(2.68)
Magnet permeance,	$B_r = 1.10$	(2.69)
Magnet recoil permeability,	$\mu_r = 1.05$	(2.71)
Stator axial thickness,	$T_{sa} \leq 4.0$	(2.72)
No. of magnet poles,	$N_{mp} \geq 2$	(2.73)
No. of magnet poles,	$N_{mp} \leq 24$	(2.74)
No. of parallel circuits,	$N_p \geq 1$	(2.75)
No. of parallel wires	$N_w \geq 1$	(2.76)
Slot opening factor,	$S_{of} \leq 1$	(2.77)
Slot opening factor,	$S_{of} \geq 0.1$	(2.78)

Slot width magnification factor, $S_{wm} \leq 1.75$ (2.79)

Tooth maximum flux density,

$$B_{tm} = \frac{2B_r\left(2\pi R_i - N_{mp}.\omega\tau_{ms}\right)}{\left(2 - S_{wm}\right)\left(2\pi R_i T_{ma} + g_e \mu_r \left(2\pi R_i - N_{mp}\tau_{ms}\right)\right)} \leq 2 \quad (2.80)$$

Yoke maximum flux density,

$$B_{ym} = \frac{B_g \pi R_o}{\left(N_{mp}\left(T_{sa} - \left(d_s + \left(d_1 + d_2\right)0.001\right)\right)\right)} \leq 2 \quad (2.81)$$

Efficiency, $$\eta = \frac{100.P}{P + P_{rl} + \sum_N \left(P_{ten} + P_{yen} + P_{thn} + P_{yhn}\right)} \geq 94.00 \quad (2.82)$$

where P_{rl} , P_{ten} , P_{yen} , P_{thn} , and P_{yhn} are given in equations (2.47) and (2.57) to (2.60) respectively.

The constraints on the maximum available supply voltage can be written as

$V_l + 2.I_{ph}R_s + Inverter\ switch\ conduction\ drop = Maximum\ available\ voltage$

Assuming 6 Volts for inverter conduction drop, this can be written as

$$\frac{N_{mp}N_c B_g \left(R_o^2 - R_i^2\right)}{N_p 10^6}\omega_m k_w + 2I_{ph}R_s 0.001 + 6 = 600 \quad (2.83)$$

where I_{ph} and R_s are given by equations (2.24) and (2.28) respectively.

In general practice, the stator winding current density is between 645 to 6452 A/In^2 (1 A/mm^2 to 10 A/mm^2) depending on the application requirement [8].

Winding current density, $$J_d = \frac{I_{ph}}{\left(N_c N_p \frac{\pi}{4} d_w^2\right)} \leq 6452 \quad (A/In^2) \quad (2.84)$$

Assuming a safety tolerance limit of 0.25 Amps, the constraint on the current carried by a single conductor results in

$$I_r - \frac{I_{ph}}{\left(N_p N_w N_c\right)} \geq 0.25 \tag{2.85}$$

$$\frac{N_{mp}}{2} = Integer \tag{2.86}$$

$$\frac{N_{mp}}{N_p} = Integer \tag{2.87}$$

$$\frac{N_c}{2} = Integer \tag{2.88}$$

$$N_w = Integer \tag{2.89}$$

Now the objective function and the set of constraints as shown in the equations (2.65) to (2.89) can be programmed in to the cells of the design program using the built in optimizer in QPRO. Then by using the Quasi-Newton method, the optimization is carried out. Table 2.7 shows the optimal design parameter report generated by the optimizer. Table 2.8 shows all the constraints and their optimal values, while table 2.9 shows the optimizer generated detail report with the values of variables as it passes through each iteration step. Design output and performance parameters for non-optimized and optimized configurations are shown in table 2.10, column 2 and 3 respectively.

Table 2.7 Optimal design parameter table.

Answer report			
Solution cell:	**Starting**	**Final**	
Specific power	**1.13**	**1.69**	
Variable cells:	Starting	Final	Dual value
Magnet outer radius	5.899	6.000	0.29
Magnet inner radius	3.000	3.597	0.00
Magnet axial thickness	0.35	0.20	-0.79
Magnet permeance	1.10	1.10	0.00
Recoil permeability	1.05	1.05	0.00
Air gap	30	20	-0.00
Stator axial thickness	1.8000	1.4446	0.00
No. of phases	3	3	0.00
No. of poles	16	18	0.00
No. of parallel cct	1	1	0.00
No. of parallel wires	4	4	0.00
No. of conductors per slot	12	12	0.00
Stator slot opening factor	0.70	0.15	-0.00
Slot width multip. factor	0.85	1.05	0.00

Table 2.8 Constraints and optimal values.

Report on constraints					
Parameter or Constraints	**Value**	**Constra.**	**Binding**	**Slack**	**Dual value**
Mag. outer radius	6.000	6	Yes	0.000	0.00
Magnet inner radius	3.597	3	No	-0.597	0.00
Mag. axial thickness	0.20	0.2	Yes	0.00	0.00
Mag. axial thickness	0.20	0.5	No	0.30	0.00
Magnet permeance	1.10	1.10	Yes	0.00	0.00
Recoil permeability	1.05	1.05	Yes	0.00	0.00
Air gap	20	20	Yes	0.00	0.00
Stator axial thickness	1.4446	1	No	-0.4446	0.00
Stator axial thickness	1.4446	4	No	2.5554	0.00
No. of phases	3	3	Yes	0	0.00
No. of poles	18	24	No	6	0.00
No. of poles	18	2	No	-16	0.00
No. of parallel cct	1	1	No	0	0.00
No. of parallel wires	4	1	No	-3	0.00
No. of conductors per slot	12	2	No	-10	0.00
Stator slot opening factor	0.15	0.1	No	-0.05	0.00
Stator slot opening factor	0.15	1.0	No	0.85	0.00
Slot width multip. factor	1.05	1.75	No	0.70	0.00
Active radial length	2.40	0.5	No	-1.90	0.00
B_{tmax}	2.00	2.00	Yes	0	0.47
B_{ymax}	2.00	2.00	Yes	0	0.29
Winding current density	1058	3871	No	2813	0.00
V_1 + IR drop+ Inv. sw.drop	600	600	Yes	0	0.00
Efficiency	95.71	94.00	No	-1.71	0.00
Even no of poles	0	0	Yes	0.00	0.13
Integer no of parallel cct.	0	0	Yes	0.00	0.00
Integer no of parallel wires	0	0	Yes	0.00	-0.21
Even no of conductors/slot	0	0	Yes	0.00	0.14
Current tolerance in a wire	3.65	0.25	No	-3.40	0.00

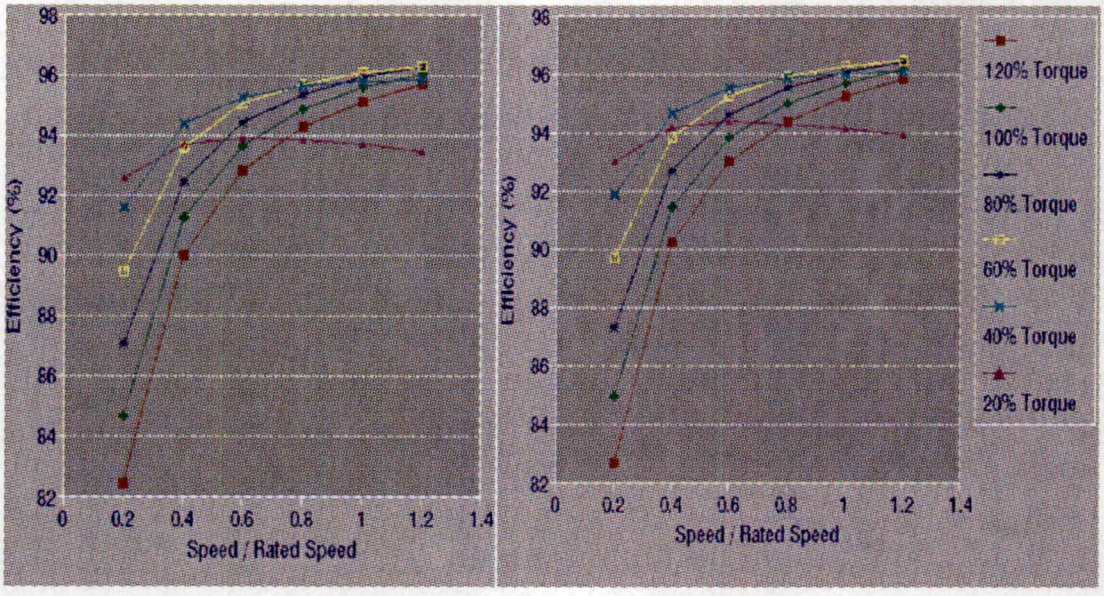
Table 2.9 Detail report of the each iteration step.

Ite. #	R_o	R_i	T_{mn}	B_r	m_r	g	T_{sn}	N_{ph}	N_{mp}	N_p	N_w	N_c	S_{of}	S_{wm}	P_{sp}
Start	5.89	3.00	0.35	1.10	1.05	30	1.80	3	16	1	4	12	0.70	0.85	1.13
# 1	5.89	3.00	0.35	1.10	1.05	30	1.80	3	18	1	4	12	0.70	0.85	1.16
# 2	5.76	3.07	0.27	1.10	1.05	30	1.81	3	18	1	4	12	0.71	0.86	1.30
# 3	5.77	3.08	0.27	1.10	1.05	30	1.83	3	18	1	4	12	0.71	0.91	1.28
# 4	5.77	3.07	0.25	1.10	1.05	30	1.83	3	18	1	4	12	0.70	0.91	1.35
# 5	5.79	3.07	0.22	1.10	1.05	30	1.75	3	18	1	4	12	0.69	1.04	1.49
# 6	5.83	3.06	0.21	1.10	1.05	30	1.57	3	18	1	4	12	0.69	1.11	1.56
# 7	5.84	3.06	0.20	1.10	1.05	30	1.49	3	18	1	4	12	0.68	1.12	1.57
#8	5.86	3.06	0.20	1.10	1.05	30	1.49	3	18	1	4	12	0.68	1.12	1.57
#9	5.86	3.34	0.20	1.10	1.05	29.9	1.41	3	18	1	4	12	0.66	1.12	1.63
#10	6.0	3.45	0.20	1.10	1.05	20	1.42	3	18	1	4	12	0.10	1.09	1.65
# 11	6.0	3.60	0.20	1.10	1.05	20	1.44	3	18	1	4	12	0.10	1.05	1.69
# 12	6.0	3.59	0.20	1.10	1.05	20	1.44	3	18	1	4	12	0.15	1.05	1.69
# 13	6.0	3.59	0.20	1.10	1.05	20	1.44	3	18	1	4	12	0.15	1.05	1.69
Opti	**6.0**	**3.60**	**0.20**	**1.10**	**1.05**	**20**	**1.44**	**3**	**18**	**1**	**4**	**12**	**0.15**	**1.05**	**1.69**
# 15	6.0	3.89	0.21	1.10	1.05	49.9	1.85	3	8	1	3	32	0.35	1.13	1.29
# 16	6.0	3.86	0.20	1.10	1.05	49.9	1.84	3	8	1	3	32	0.33	1.14	1.29
# 17	6.0	3.86	0.20	1.10	1.05	49.9	1.84	3	8	1	3	32	0.33	1.14	1.29
# 18	6.0	3.88	0.20	1.10	1.05	49.9	1.85	3	8	1	3	32	0.20	1.14	1.29
# 19	6.0	3.89	0.20	1.10	1.05	30.8	1.85	3	8	1	3	32	0.19	1.13	1.29
# 20	6.0	4.10	0.20	1.10	1.05	20	1.95	3	8	1	3	32	0.12	1.06	1.32
# 21	6.0	4.21	0.20	1.10	1.05	20	2.03	3	8	1	3	32	0.16	1.01	1.33
# 22	5.78	3.87	0.20	1.10	1.05	20	2.04	3	8	1	3	32	0.29	1.01	1.33
# 23	5.72	3.77	0.20	1.10	1.05	20	2.04	3	8	1	3	32	0.43	1.02	1.33
# 24	5.81	3.86	0.20	1.10	1.05	20	1.99	3	8	1	3	32	0.72	1.04	1.34
# 25	5.85	3.93	0.20	1.10	1.05	20	1.99	3	8	1	3	32	0.69	1.04	1.34
Final	5.85	3.93	0.20	1.10	1.05	20	2	3	8	1	3	32	0.70	1.04	1.34

Table 2.10 Output and performance parameters for optimized and non-optimized design.

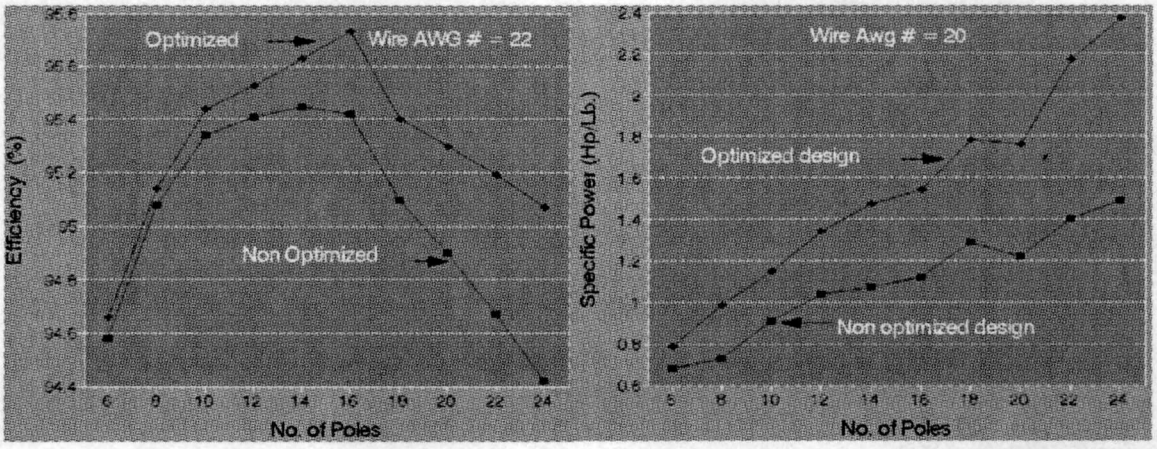
Output Data and Performance Parameters	Non-optimized	Optimized	Units
Torque	145.88	145.88	Ft-Lb.
Active radial length	2.89	2.40	Inch
Tooth width at inside radius	0.225	0.198	Inch
Shoe width at inside radius	0.276	0.384	Inch
Slot width at inside radius	0.167	0.220	Inch
Slot opening at inside radius	0.116	0.043	Inch
Carter's coefficient	1.15	1.02	
Effective gap length	34.6	20.50	mils
Area of magnet / Area of gap	0.95	0.95	
B_g at stator iron surface	0.949	0.949	Tesla
Peak flux per pole	0.08	0.07	mV-sec
B_t at inside radius	1.650	2.00	Tesla
Required slot area	0.178	0.177	$Inch^2$
Required slot depth	1.169	0.870	Inch
B_y max at stator yoke	1.985	2.000	Tesla
Phase current	65.64	64.88	Amps
Slot current density	1071	1058	A/in^2
Line to line back emf at rated speed	567.99	574.62	Volts
V_{l-l}+I.R drop+Inverter switch drop	593	600	Volts
Mean length per turn	11.22	10.04	Inch
Phase resistance	148.30	149.33	mOhm
Phase inductance	0.241	0.378	mH
Stator tooth volume	69.519	40.64	$Inch^3$
Stator back iron volume	44.49	35.98	$Inch^3$
Stator iron volume	114.01	76.62	$Inch^3$
Weight of the stators	62.93	42.29	Lb.
Magnet weight	15.40	7.91	Lb.
Wire weight	5.30	5.34	Lb.
Rotor weight	19.55	11.40	Lb.
Total active material weight	87.77	59.03	Lb.
Specific power	1.14	1.69	Hp/Lb.
Total active material cost	1161	611	$
I^2R loss at rated current	1278.03	1257.36	Watts
Teeth loss at rated speed	304.17	263.78	Watts
Stator yoke loss at rated speed	147.57	150.30	Watts
Efficiency at rated speed and rated torque	95.57	95.71	%

Fig 2.9a and 2.9b exhibit the efficiency curves in the torque-speed plane for the two designs. As can be seen from these fplots, there is not much improvement in the efficiency for the optimized design since the objective was to optimize the specific power. However, in designing a machine for a given application, the consideration should also be given to other aspects such as thermal, frequency and mechanical concerns. Therefore, a particular design which is optimum for a certain application may not be optimal for another application in the same power range. Thus, rather than giving one optimal design, it is helpful to give a set of optimal designs so that the customer can select the best design according to application requirements [13]. Such a set of optimal performance parameters for different design input parameters are shown in table 2.11. In this set of data, the number of magnet poles and the winding wiresize (AWG) # are considered as main parameters. Fig. 2.10a, 2.10b and 2.10c show the variation of the three main performance parameters, cost, efficiency and specific power if the number of poles were changed keeping the wire size (AWG #) constant.

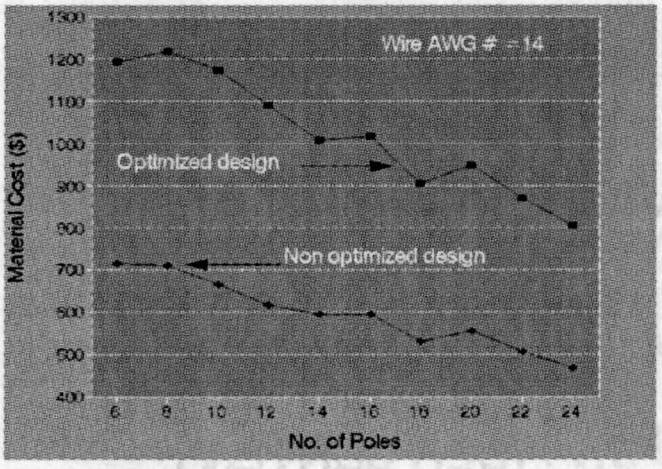


(a) Non-optimized design (b) Optimized design

Fig. 2.9 Efficiency curves in the torque-speed plane.



(a) Efficiency variation (b) Specific power variation



(c) Material cost variation

Fig. 2.10 Main performance parameter's sensitivity to the pole order.

Table 2.11 Non-optimal/optimal design parameters for different design requirements.

AWG #	No. of	Poles	6	8	10	12	14	16	18	20	22	24
14	Non-opti	SP (Hp/Lb)	0.59	0.59	0.52	0.67	1.16	1.16	1.39	1.42	1.50	1.54
		Effi. (%)	94.16	94.77	96.07	96.21	96.29	96.29	96.12	96.14	96.02	96.89
		Cost ($)	1193	1217	1175	1091	1016	1016	904	948	870	804
	Optim.	SP (Hp/Lb)	0.86	1.03	1.2	1.42	1.66	1.66	1.91	1.91	2.12	2.32
		Effi. (%)	94.88	95.61	95.94	96.08	96.32	96.32	96.25	96.36	96.28	96.20
		Cost ($)	713	710	667	616	594	594	530	556	507	467
16	Non-opti	SP (Hp/Lb)	0.93	1.08	1.3	1.44	1.78	1.78	1.89	1.96	1.97	2.09
		Effi. (%)	93.97	94.97	95.22	95.67	95.87	95.97	95.87	96.01	96.14	96.09
		Cost ($)	634	615	558	566	561	525	776	702	746	586
	Optim.	SP (Hp/Lb)	0.98	1.2	1.44	1.58	1.75	1.89	2.15	2.20	2.21	2.39
		Effi. (%)	94.12	94.84	95.32	95.63	95.79	95.95	95.88	96.03	96.15	96.09
		Cost ($)	617	605	561	556	529	519	465	477	484	465
18	Non-opt	SP (Hp/Lb)	0.71	0.90	0.95	1.02	1.05	1.13	1.23	1.32	1.42	1.51
		Effi. (%)	94.00	94.58	95.00	95.37	95.54	95.59	95.47	95.34	95.54	95.42
		Cost ($)	1240	1155	1110	1160	1147	1168	1044	951	1011	943
	Optim.	SP (Hp/Lb)	0.82	1.03	1.23	1.28	1.40	1.43	1.69	1.93	1.97	2.04
		Effi. (%)	94.00	94.56	95.00	95.45	95.62	95.77	95.71	95.64	95.77	95.69
		Cost ($)	835	689	659	686	673	689	611	550	603	554
20	Non-opti	SP (Hp/Lb)	0.68	0.73	0.91	1.04	1.07	1.12	1.29	1.22	1.40	1.49
		Effi. (%)	93.47	94.24	94.61	94.7	94.91	95.00	94.80	94.91	94.24	94.03
		Cost ($)	1233	1169	1115	1025	1004	1006	897	951	858	793
	Optimi.	SP (Hp/Lb)	0.79	0.99	1.15	1.34	1.47	1.54	1.78	1.76	2.17	2.37
		Effi. (%)	93.53	94.20	94.65	94.82	95.00	95.18	95.08	95.23	94.61	94.52
		Cost ($)	744	690	660	611	589	589	526	553	497	458
22	Non-opti	SP (Hp/Lb)	0.6	0.75	0.82	0.89	0.93	0.97	1.08	1.15	1.22	1.25
		Effi. (%)	94.58	95.08	95.34	95.41	95.45	95.42	95.10	94.90	94.67	94.42
		Cost ($)	1241	1163	1114	1042	1014	1015	1038	943	867	802
	Optimi.	SP (Hp/Lb)	0.72	0.89	1.02	1.19	1.30	1.35	1.50	1.71	1.89	2.07
		Effi. (%)	94.66	95.14	95.44	95.53	95.63	95.73	95.40	95.30	95.19	95.07
		Cost ($)	764	708	675	624	602	602	616	555	506	467

2.4 Three Phase and Five Phase Axial Gap Brushless DC Machines

2.4.1 Introduction

In traditional machine drive applications, three phases are normally selected since the normal utility supply consists of three balanced phases. However, when the machines are connected to an adjustable speed drive, a different number of phases can be chosen and may result in better utilization, performance and reliability. Although a balanced three phase, three wire system cannot support a third harmonic component of current, it can flow in systems having a different number of phases. In particular, studies have shown [14] that where as a three phase machine can utilize only the fundamental component to develop the torque, torque can be developed by both first and third harmonics in a five phase machine. Furthermore, five phase machines are particularly attractive since they require the fewest number of transistors beyond the three phase system. In [15] , authors show that 33% addition of third harmonic current component to the stator current results in 10-12% more torque even with the saturation properly taken into account. For a five phase system, the corresponding inverter required ten transistors, each of which operate at a better utilization factor when compared with a conventional three phase inverter. In [16], authors have shown that the ratio of the required peak VA rating of the switches to machine peak VA is lower for the five phase system. The ratio between the figure of merit in two cases is 5:6. It is also well known that the sinusoidal back emf machines in general are not optimum in terms of utilizing the available air gap volume for torque production because only a fraction of air the gap contains the limited peak value of flux density.

Thus, a machine with a trapezoidal back emf and square current waveforms have the potential to produce the maximum force density over the entire air gap periphery. Furthermore, the control strategies are much simpler and cost effective in brushless machines. In [17], authors have proved that for equal rms heating and for equal peak air gap flux density, in comparison to the sinusoidal case, the square wave machine has a force per pole advantage. The figure of merit for the force per pole is given by $\sqrt{2}m_p$, where m_p is the pole pitch which at any time has full stator current sheet excitation at maximum value[17]. For a five phase machine, this figure of merit has a higher value of 1.27, when compared with that of a three phase machine which has a value of 1.16 [17]. Furthermore, a five phase machine can run even with one phase at fault, provided that the per phase ratings are not exceeded, but in a three phase machine this is not possible. This makes a five phase machine more fault tolerant than a three phase machine. This type of fault tolerant operation of the drive system becomes very attractive in aerospace and electric vehicle applications. Such applications also demand light weight and high efficiency systems. Therefore, it is worth studying how much improvement in performance parameters can be obtained in a five phase machine, compared to a three phase machine. In the following section, a comparison is made between five and three phase brushless DC machines.

2.4.2 Comparative Representation

This section make a detail comparative study of three phase and five phase 100-500 Hp, 1800 Rpm, 400 Volts brushless DC machines. In this study, the machine design

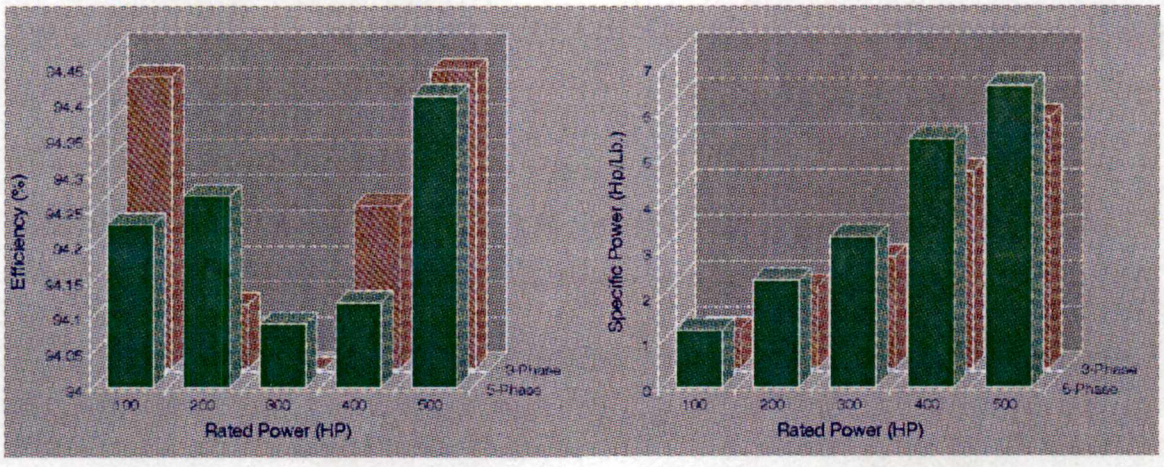
parameters are obtained separately for optimum efficiency and optimum specific power respectively. When the design parameters are sought for optimum specific power, the efficiency is kept very close to a minimum value required by the efficiency constraint condition for both five phase and three phase designs. This ensures that the comparisons of the performance parameters will result in a better picture than if the efficiencies were very much different for the two configurations. Table 2.12 shows the performance parameters comparison for designs which optimize the specific power. Fig. 2.11 a, b, c, d show their comparison in graphical form. Table 2.13 shows the performance parameters for designs which optimize the machine efficiency. In these optimizations the machine specific power is kept in the same range of values for three phase and five phase designs, so that a more meaningful comparison can be made between two configurations. Fig. 2.12 a, b, c, d show the comparison between them. Fig. 2.11b shows that the specific power that could be achieved by having a five phase machine is about 20-30% higher than that could be obtained if the machine was designed for three phase operation. The number of stator slots required in five phase configuration is always higher than that of the three phase configuration. This results in higher stator flux densities in the tooth and back iron in a five phase machine, for a given stator size. Therefore, five phase design always has higher core losses. This can be seen from fig. 2.11c and fig. 2.12c. However, the reduction in per phase current in five phase configuration helps to yield a lower stator copper loss. This is shown in fig. 2.11d and 2.12d. Thus, the total power loss in five phase

Table 2.12 Optimized performance parameters for 3 phase and 5 phase configurations for optimum specific power.

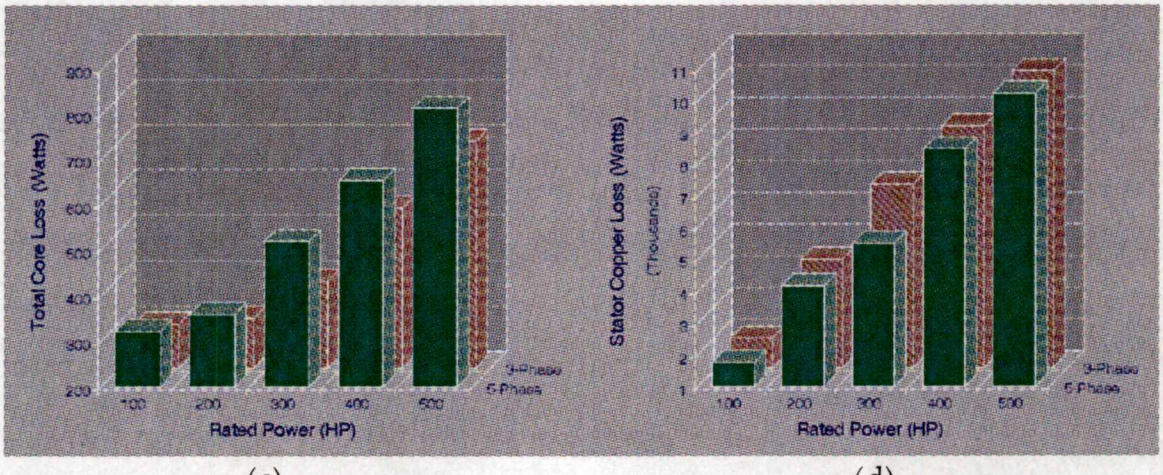
	Efficiency		Optim. SP		Optim. core loss		Optim. I^2R loss	
HP	3-Ph	5-Ph	3-Ph	5-Ph	3-Ph	5-Ph	3-Ph	5-Ph
100	94.41	94.23	0.87	1.67	296	522	1915	1760
200	94.09	94.27	1.79	2.35	310	360	4377	4178
300	94.00	94.09	2.46	3.32	390	520	6753	5493
400	94.23	94.12	4.32	5.44	552	654	8580	8471
500	94.42	94.41	5.51	6.61	699	815	10324	10228

Table 2.13 Optimized performance parameters for 3 phase and 5 phase configurations for optimum efficiency.

	Optim. Effici.		Specific Power		Optim. core loss		Optim. I^2R loss	
HP	3-Ph	5-Ph	3-Ph	5-Ph	3-Ph	5-Ph	3-Ph	5-Ph
100	94.93	96.46	0.45	0.46	200	272	1791	1098
200	95.68	96.29	1.04	1.05	311	359	3057	2519
300	96.07	96.84	1.68	1.65	466	584	4106	3069
400	96.58	96.92	2.35	1.93	830	934	5228	3812
500	96.81	97.03	2.47	2.55	1037	1072	5109	4627

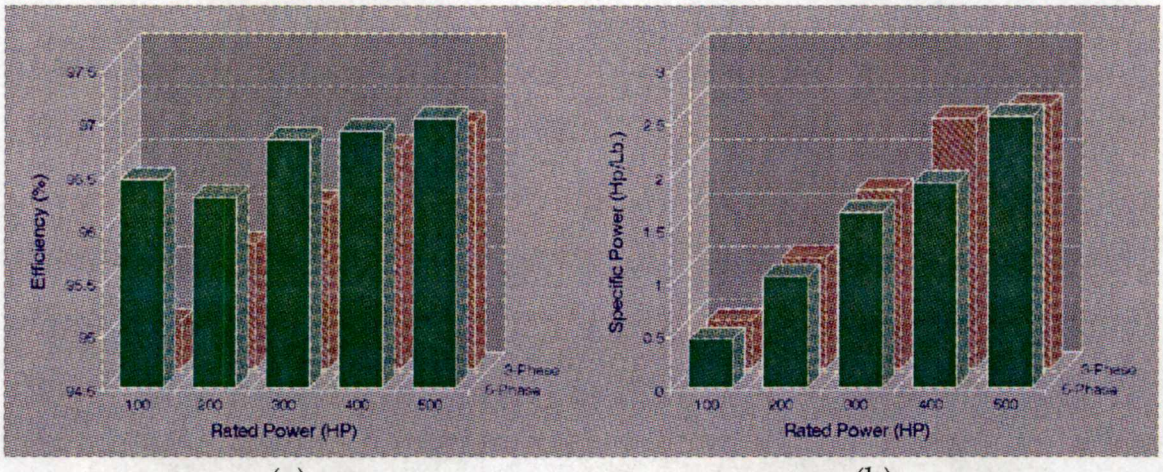


(a) (b)



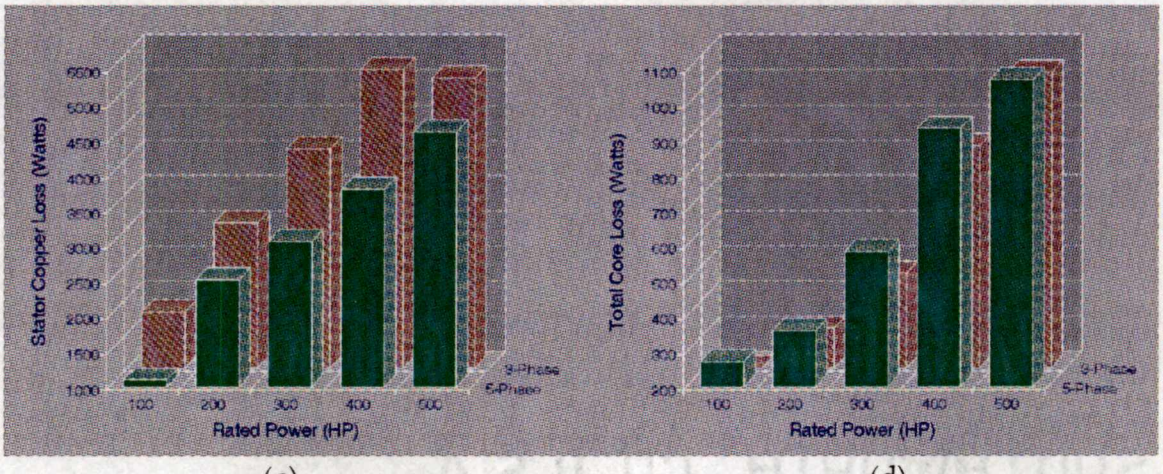
(c) (d)

Fig. 2.11 Performance parameters comparison for 3 phase and 5 phase configurations for optimum specific power.



(a)

(b)



(c)

(d)

Fig. 2.12 Performance parameters comparison for 3 phase and 5 phase configurations for optimum efficiency.

configuration is about 10-30% less than that of the three phase version depending on the power level of the machine.

2.5 Multiobjective Optimization Approach for Practical Applications

2.5.1 Introduction

When designing an adjustable speed drive system, the general objective of the designer is to produce a design that optimizes many performance parameters and characteristics. As described in preceding sections and shown in table 2.11 these objectives unfortunately conflict with each other. For example, the requirements for optimal specific power and the requirement for optimal efficiency conflict with each other. Similarly the efficiency and the material cost requirements conflict. Therefore, optimization of one of these performance parameters with the help of appropriate constraints for the other performance parameters will result in a sub-optimal design [18]. Also, in general, it is very difficult to precisely specify the relative importance of these parameters without referring to the type of application of the adjustable speed drive system. Therefore, a trade-off curve describing the possibilities of optimal designs can offer the customer a more useful approach. Such a curve sets the feasibility frontier for the optimal design and performance parameters. Such a set of optimal designs and the corresponding trade-off curve can be obtained by considering a multiple objective optimization approach, instead of a scalar optimization [18]. The advantage of this type of design approach is the capability of obtaining a superior compromised optimal design, instead of a sub-optimal design. Fig. 2.13 is an example of a possible trade-off

curve between two attributes [13]. The design points that lie on the feasibility frontier curve are superior design points and they are optimal in terms of the two attributes considered. The feasibility curve also divides the attribute space into feasible and infeasible regions of design points. Those points which are above the frontier curve are not feasible . Design points which lie below the curve are feasible but can be considered as inferior design points. The frontier line also shows that when the design point is chosen such that attributes lie on the curve, no other design can be achieved to improve one attribute without adversely affecting the other.

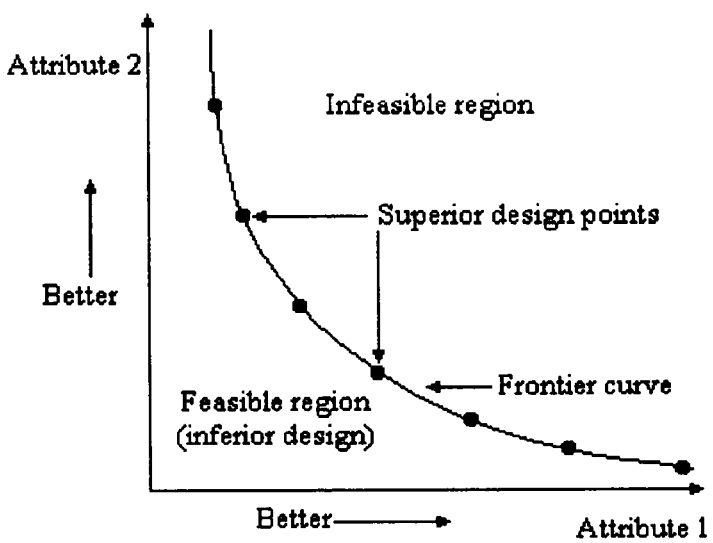


Fig. 2.13 A typical trade-off curve for two performance parameters.

2.5.2 Bi-criterion Optimization Problem Formulation and Solution

In this section, the bi-criterion optimization for the simultaneous maximization of efficiency and specific power for a 100 Hp, 3200 Rpm, 216 Volts axial gap brushless dc machine with a maximum diameter of 11 inches is described. This machine is primarily aimed for electric vehicle propulsion. During this approach, the multiobjective function is formulated as a normalized objective function. Therefore, it is necessary to find the maximum efficiency and maximum specific power that could be obtained under the given constraints conditions, if the problem was considered as a scalar optimization (i.e. single objective optimization) problem, as discussed in the preceding sections. First it is necessary to treat the optimization problem as a pure efficiency optimization problem and formulate the corresponding objective function and constraint conditions, so that the attainable maximum efficiency, η_{max}, can be found . Let the efficiency function can be written as $F(\eta)$. Then the optimization problem can be stated as:

$$\text{Max}\{F(\eta)\} = Max\left\{\frac{P}{P + P_{rl} + \sum_{N}\left(P_{ten} + P_{yen} + P_{thn} + P_{yhn}\right)}\right\} \tag{2.90}$$

Subject to constraints:

Outer radius,	$R_o \leq 5.5$	(2.91)
Inner radius,	$R_i \geq 3$	(2.92)
Magnet axial thickness,	$T_{ma} \geq 0.2$	(2.93)
Magnet permeance,	$B_r = 1.216$	(2.94)

Magnet recoil permeability, $\mu_r = 1.20$ (2.95)

Air gap, $g \geq 20$ (2.96)

Stator axial thickness, $T_{sa} \leq 4.0$ (2.97)

No. of magnet poles, $N_{mp} \geq 2$ (2.98)

No. of magnet poles, $N_{mp} \leq 24$ (2.99)

No. of parallel circuit, $N_p \geq 1$ (2.100)

No. of parallel wires $N_w \geq 1$ (2.101)

Slot opening factor, $S_{of} \leq 1$ (2.102)

Slot opening factor, $S_{of} \geq 0.1$ (2.78)

Slot width mag. factor, $S_{wm} \leq 1.75$ (2.103)

Tooth maximum flux density,

$$B_{tm} = \frac{2B_r\left(2\pi R_i - N_{mp}.\omega\tau_{ms}\right)}{\left(2 - S_{wm}\right)\left(2\pi R_i T_{ma} + g_e\mu_r\left(2\pi R_i - N_{mp}\tau_{ms}\right)\right)} \leq 2 \quad (2.104)$$

Yoke maximum flux density,

$$B_{ym} = \frac{B_g\pi R_o}{\left(N_{mp}\left(T_{sa} - \left(d_s + \left(d_1 + d_2\right)0.001\right)\right)\right)} \leq 2 \quad (2.105)$$

The constraints on the maximum available supply voltage can be written as

$V_l + 2.I_{ph}R_s + Inverter\ switch\ conduction\ drop = Maximum\ available\ voltage$

Assuming a 6 Volts for inverter conduction drop, this can be written as

$$\frac{N_{mp}N_c B_g\left(R_o^2 - R_i^2\right)}{N_p 10^6}\omega_m k_w + 2I_{ph}R_s.0.001 + 6 = 216 \tag{2.106}$$

where I_{ph} and R_s are given by equations (2.24) and (2.28) respectively.

Winding current density, $J_d = \dfrac{I_{ph}}{\left(N_w N_p \dfrac{\pi}{4} d_w^2\right)} \leq 6452$ (2.107)

Assuming a safety tolerance limit of 0.25 Amps the constraint on the current carried by a single conductor results in

$$\frac{I_{ph}}{\left(N_p N_w\right)} - I_r \geq 0.25 \tag{2.108}$$

$$\frac{N_{mp}}{2} = Integer \tag{2.109}$$

$$\frac{N_{mp}}{N_p} = Integer \tag{2.110}$$

$$\frac{N_c}{2} = Integer \tag{2.111}$$

$$N_w = Integer \tag{2.112}$$

Now, as explained in section 2.3, the efficiency optimization can be carried out. Table 2.14, column 3 shows the optimal design input data and table 2.15, column 3 shows the optimal design output and performance parameters. Thus η_{max}, is found to be equal to 98.06 (@ a specific power of 0.69 Hp/Lb.).

Table 2.14 Optimal design input parameters.

Parameter	Non opt.	Eff. opt.	Sp. opt	Units
1. Machine Ratings and Configuration:				
Rated power	100	100	100	Hp
Rated speed	3200	3200	3200	Rpm
Rated voltage (L-L)	216	216	216	Volts
No. of magnet poles	12	12	14	
No. of phases	3	3	3	
Phase winding connection config.	Star	Star	Star	
2. Stator Data:				
Stator outer radius	5.180	5.500	4.557	Inch
Stator inner radius	3.730	3.000	3.557	Inch
Stator iron axial thickness	1.34	4.000	1.3042	Inch
Stator lamination thickness	14	14	14	mils
3. Stator Winding Data:				
No. of parallel circuit/phase	1	1	1	
No. of parallel wires/conductor	5	20	5	
No.of conductors/slot	6	6	8	
No. of coil sides/slot	2	2	2	
No. of stator slots	36	36	42	
No. of slots/pole/phase	1	1	1	
Winding distribution factor	1.000	1.000	1.000	
Winding pitch factor	1.000	1.000	1.000	
Winding factor	1.000	1.000	1.000	
Wire AWG	16	16	16	
Wire diameter	0.0508	0.0508	0.0508	Inch
Wire resistance/1000 ft	4.16	4.16	4.16	Ohm
Wire weight/1000 ft	7.81	7.81	7.81	Lb.
No. of wires per square inch	380	380	380	
Continuos current rating	7.50	7.50	7.50	Amps
Coil extension at inner radius	0.25	0.25	0.25	
Coil extension at outer radius	0.25	0.25	0.25	
4. Slot Geometry Data:				
Stator slot tip depth	35	35	50	mils
Stator slot wedge depth	43	43	25	mils
Space between two coil sides	60	60	60	mils
Stator average slot opening factor	0.51	1.00	1.00	
Stator slot width mult. factor	1.05	1.37	0.99	
Slot fill factor	0.60	0.60	0.60	
Slot insulation thickness	7	7	7	mils

5. Magnet and Air Gap data:				
Magnet axial thickness	0.30	0.20	0.20	Inch
Magnet remanence	1.216	1.216	1.216	
Magnet recoil permeability	1.20	1.20	1.20	
Magnet spacer thickness	0.063	0.063	0.063	
Air gap	40	108.60	21.94	mils
6. Other Data:				
Shaft diameter	0.75	0.75	0.75	Inch
Rotor steel thickness	0.125	0.125	0.125	Inch
Rotor steel density	0.278	0.278	0.278	Lb/In^3
Stator steel density	0.276	0.276	0.276	Lb/In^3
Magnetic material density	0.273	0.273	0.273	Lb/In^3
Eddy current constant for lamination	$9.30*10^{-3}$	$9.30*10^{-3}$	$9.30*10^{-3}$	
Hysteresis constant for laminations	$5.80*10^{-3}$	$5.80*10^{-3}$	$5.80*10^{-3}$	
Hysteresis exponent coefficient	1.93	1.93	1.93	

Table 2.15 Optimal design output and performance parameters.

Output Data and Performance Parameters	Value	Value	Value	Units
Torque	82.06	82.06	82.06	Ft-Lb.
Active radial length	1.45	2.50	1.00	Inch
Tooth width at inside radius	0.309	0.164	0.269	Inch
Shoe width at inside radius	0.477	0.164	0.269	Inch
Slot width at inside radius	0.342	0.359	0.263	Inch
Slot opening at inside radius	0.175	0.359	0.263	Inch
Carter's coefficient	1.14	1.38	1.53	
Effective gap length	45.67	149.60	33.46	mils
Area of magnet / Area of gap	0.97	0.96	0.98	
B_g at stator iron surface	1.000	0.627	1.012	Tesla
Peak flux per pole	0.04	0.04	0.03	mV-sec
B_t at inside radius	2.005	2.000	2.000	Tesla
Required slot area	0.131	0.526	0.175	In^2
Required slot deapth	0.408	1.530	0.711	Inch
B_y max at stator yoke	1.617	0.377	2.000	Tesla
Phase current	185.41	179.83	187.52	Amps
Slot current density	3052	742	2316	A/In^2
Line to line back emf at rated speed	201.08	207.33	198.83	Volts
V_{l-l}+I.R drop+Inverter switch drop	216	216	216	Volts
Mean length per turn	10.14	11.91	7.67	Inch
Phase resistance	25.32	7.43	29.79	mOhm
Phase inductance	0.0337	0.0548	0.0557	mH
Stator tooth volume	11.58	53.90	11.08	In^3
Stator back iron volume	34.03	159.66	13.19	In^3
Stator iron volume	45.61	213.56	24.27	In^3
Weight of the stators	25.18	117.87	13.40	Lb.
Magnet weight	6.65	7.29	2.78	Lb.
Wire weight	3.57	16.75	4.19	Lb.
Rotor weight	8.97	11.21	4.41	Lb.
Total active material weight	37.71	145.83	22.00	Lb.
Specific power	2.65	0.69	4.55	Hp/Lb.
Total active material cost	502.88	649.04	218.63	$
I^2R loss at rated current	1741	480.73	2095.06	Watts
Teeth loss at rated speed	110.15	224.27	162.58	Watts
Stator yoke loss at rated speed	136.54	34.25	101.97	Watts
Efficiency at rated speed and rated torque	94.94	98.06	94.05	%

The next step is to formulate the optimization problem as a pure specific power optimization problem in order to find the maximum attainable specific power under the same constraint conditions. Let the specific power function can be written as $F(S_p)$. Then the optimization problem can be stated as:

$$\text{Max}\left[F(S_p)\right] \tag{2.113}$$

Subject to:

Same constraints conditions shown in equations (2.91) to (2.112) plus

$$\text{Efficiency, } \eta = \frac{100.P}{P + P_{rl} + \sum_{N}\left(P_{ten} + P_{yen} + P_{thn} + P_{yhn}\right)} \geq 94.00 \tag{2.114}$$

where P_{rl} , P_{ten} , P_{yen} , P_{thn} , and P_{yhn} are given in equations (2.47) and (2.57) to (2.60) respectively. Table 2.14, column 4 shows the optimal design input parameters, while table 2.15, column 4 shows the optimal design output and performance parameters for the specific power optimization problem. This shows that the maximum specific power, S_{pmax} , that can be obtained subjected to given constraints condition is 4.55 Hp/Lb. (@ 94.05% efficiency). Now using the values of η_{max} and S_{pmax}, we can formulate the normalized multiobjective problem as follows:

$$\text{Max}\left\{w_{sp}.\frac{F(S_p)}{S_{p\max}} + w_{ef}.\frac{F(\eta)}{\eta_{\max}}\right\} \tag{2.115}$$

Subject to:

Same constraint conditions under which $F(S_p)$ was maximized and

$$w_{sp} + w_{ef} = 1 \tag{2.116}$$

where w_{sp} and w_{ef} are the weighting factors given to each performance parameter depending upon how important these parameters are to a particular application. When $w_{sp} = 1$ $(i.e.\ w_{ef} = 0)$ the multiobjective optimization problem becomes a single objective specific power optimization and when $w_{ef} = 1$ $(i.e.\ w_{sp} = 0)$ the problem becomes an efficiency optimization problem. Thus depending on the weighting factors assigned to the two performance parameters, we can obtain the different optimal design points and hence the frontier curve for the two parameters. Fig. 2.14 shows the trade-off curve between the efficiency and the specific power that could be obtained when the weighting factor w_{ef} is varied from 0 to 1 $(i.e.\ w_{sp}$ from 1 to 0). This set of design points and the trade-off curve allow the designer to make a better compromised selection depending on the requirement of the drive application. Table 2.16 shows the output and performance parameters for three different weighting factors. As w_{ef} is increased from 0 to 1 there is a considerable improvement in the efficiency characteristics over the torque-speed operating range. Table 2.17 shows the sensitivity of the machine efficiency and the specific power to the weighting factors. Fig. 2.15 a, b, c, d, e show how the efficiency varies over the torque-speed plane as w_{ef} is varied from 1 to 0. Fig. 2.16a and fig. 2.16b show the sensitivity of the efficiency and the specific power to the weight coefficients.

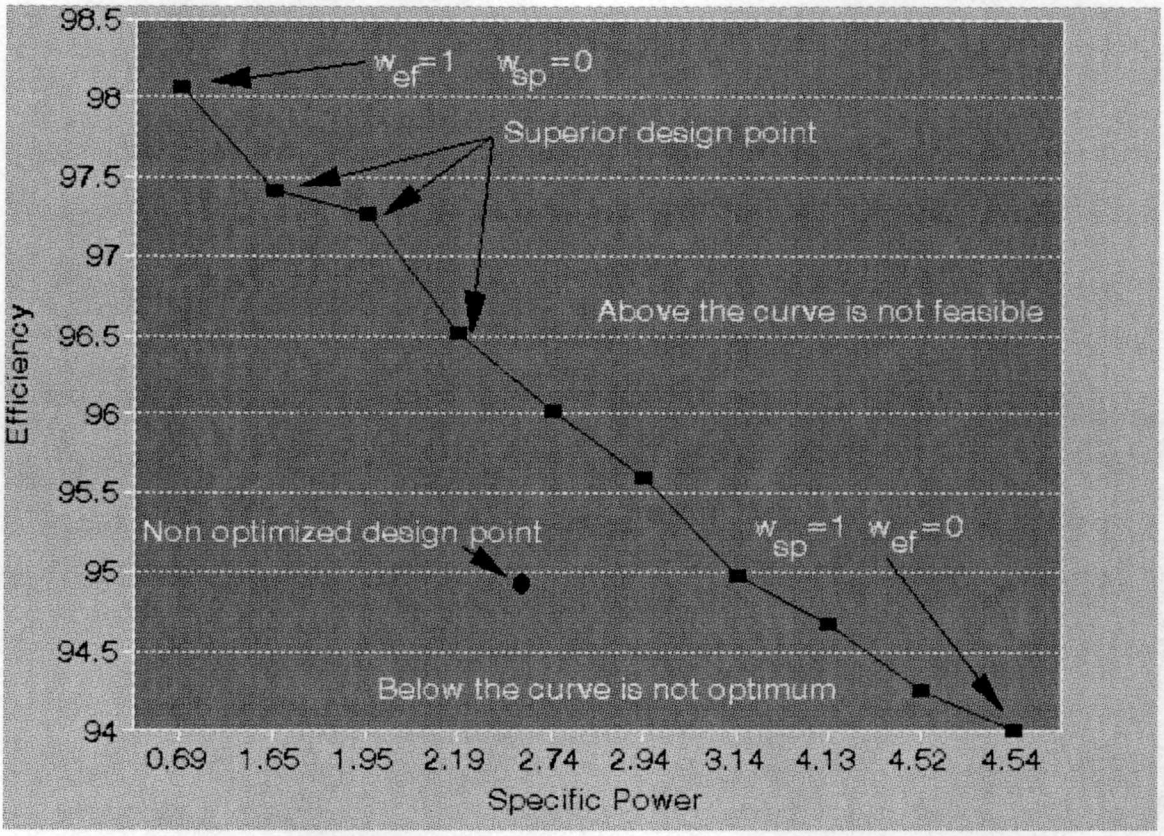


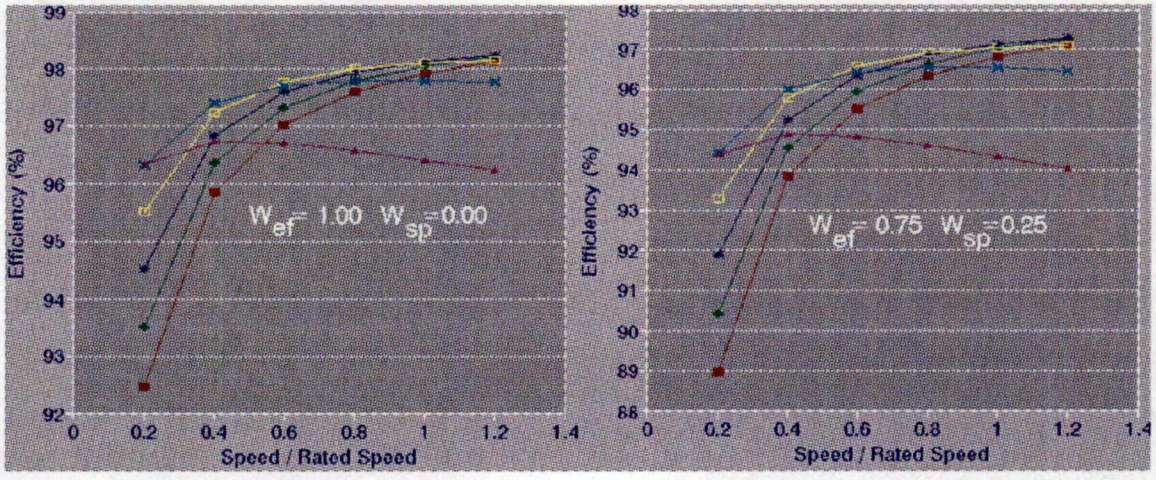
Fig. 2.14 Feasiblity frontier curve for efficiency Vs. specific power.

Table 2.16 Optimal output and performance parameters for different weighting factors.

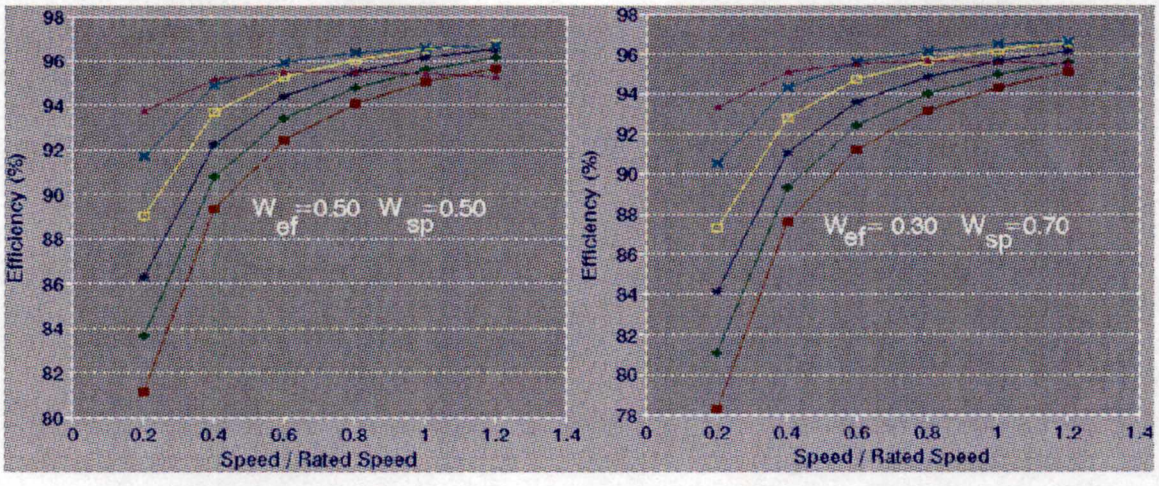
Output Data and Performance Parameters	w_{ef}=0.75 w_{sp}=0.25	w_{ef}=0.55 w_{sp}=0.45	w_{ef}=0.30 w_{sp}=0.70	**Units**
Torque	111.26	111.26	111.26	N-m
Active radial length	1.46	1.52	1.54	Inch
Tooth width at inside radius	0.334	0.311	0.299	Inch
Shoe width at inside radius	0.403	0.435	0.337	Inch
Slot width at inside radius	0.370	0.331	0.296	Inch
Slot opening at inside radius	0.301	0. 208	0.258	Inch
Carter's coefficient	1.40	1.23	1.45	
Effective gap length	42.10	37.00	29.13	mils
Area of magnet / Area of gap	0.97	0.97	0.97	
B_g at stator iron surface	0.948	0.969	1.005	Tesla
Peak flux per pole	0.04	0.04	0.04	mV-sec
B_t at inside radius	2.000	2.000	2.000	Tesla
Required slot area	0.316	0. 184	0.131	In^2
Required slot deapth	0.893	0.587	0.473	Inch
B_y max at stator yoke	2.000	2.000	2.000	Tesla
Phase current	181.01	183.40	185.63	Amps
Slot current density	1239	2155	3052	A/In^2
Line to line back emf at rated speed	205.98	203.29	200.85	Volts
V_{l-l}+I.R drop+Inverter switch drop	216	216	216	Volts
Mean length per turn	10.68	10.26	9 .87	Inch
Phase resistance	11.11	18.29	24.64	mOhm
Phase inductance	0.0520	0.0513	0.0506	mH
Stator tooth volume	23.59	16.47	13.16	In^3
Stator back iron volume	29.93	27.93	26.26	In^3
Stator iron volume	53.52	44.40	39.42	In^3
Weight of the stators	29.54	24.51	21.76	Lb.
Magnet weight	4.79	4.62	4.41	Lb.
Wire weight	9.01	5.05	3.47	Lb.
Rotor weight	7.22	6.92	6.59	Lb.
Total active material weight	45.76	145.83	31.82	Lb.
Specific power	2.19	2.74	3.14	Hp/Lb.
Total active material cost	384	361	340	$
I^2R loss at rated current	727.88	1230.31	1697.93	Watts
Teeth loss at rated speed	237.92	153.45	123.87	Watts
Stator yoke loss at rated speed	182.17	163.68	151.03	Watts
Efficiency at rated speed and rated torque	97.01	96.02	94.98	%

Table 2.17 Efficiency and specific power sensitivity to weighting coefficients.

Effi. weight fac.	**Efficiency over T-S plane**		**Sp. weight fac.**	**Specific power**
w_{ef}	η_{min}	η_{max}	w_{sp}	S_p
1.00	92.55	98.02	0.00	0.69
0.90	92.75	97.50	0.10	1.65
0.80	90.89	97.30	0.20	1.95
0.75	89.00	97.15	0.25	2.19
0.55	82.60	96.85	0.45	2.74
0.50	81.30	96.50	0.50	2.94
0.30	78.10	96.00	0.70	3.14
0.20	77.00	95.80	0.80	4.13
0.10	75.53	95.60	0.90	4.52
0.00	74.60	95.30	1.00	4.55

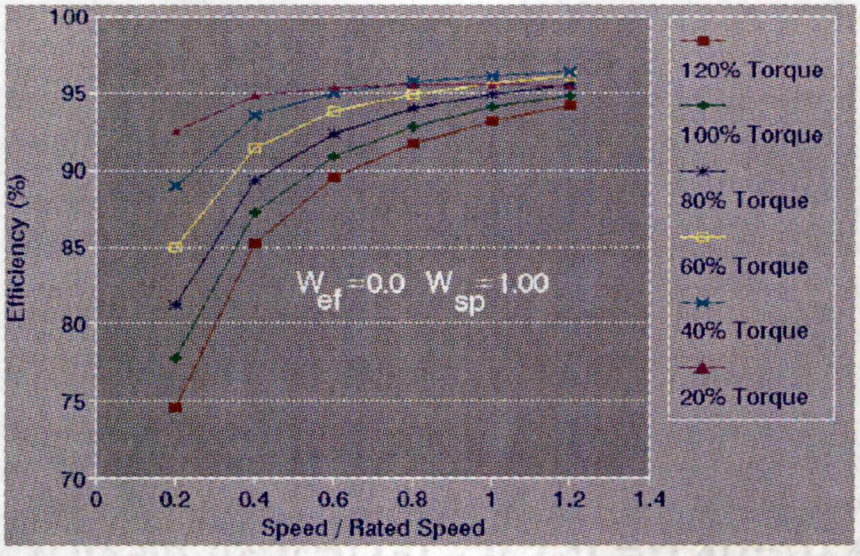


(a) (b)



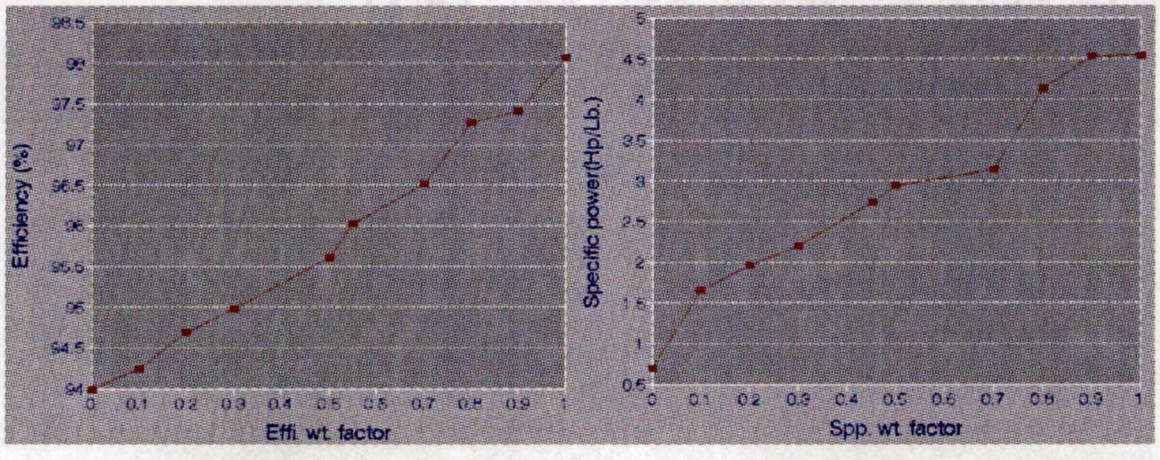
(c) (d)

Fig. 2.15 Efficiency variation over the operating region for different w_{ef} values.



(e)

Fig. 2.15 (continued).



(a) (b)

Fig. 2.16 Performance parameter sensitivity to weight coefficients.

CHAPTER 3

SELECTION OF INVERTER TOPOLOGY FOR ADJUSTABLE SPEED DRIVE SYSTEM ANALYSIS

3.1 Introduction

In all areas of adjustable speed drive applications, there is a need for increasing the performance and power density of the power converters. Performance of a converter can be characterized by factors such as ripple current, transient response, spectral characteristics and acoustic noise. Improvement of such parameters can be accomplished by using higher switching frequencies. Power switching device technology has improved steadily and these devices are capable of switching at very high frequencies, mostly in the range of 50-80 kHz. However, it can be said that in present hard-switched PWM converters used in the industry, the switching devices are not utilized to the extent of their capabilities, due to the higher thermal losses which occur at higher switching frequencies. Recent developments in converter topologies have shown that soft-switching converters will be a very attractive solution to overcome inherent shortcomings of the hard-switched conventional converters which are extensively used in the industry at the present time [33] [34].

Soft switching converters are of two types; Zero current switching and zero voltage switching. In zero current switching configuration the device turn-on and turn-off occur with no current in the device. Zero voltage switching occurs when the voltage across the device is zero. In both configurations the devices have very low switching

losses and how close the switching losses are to zero, is dependent on the values of the snubber capacitors and the inductors used in the application [34]. Many switching configurations can be used to reduce the switching losses in a PWM converter. The reduction in switching losses reduces the heat dissipation within the device and allows substantial increase in the inverter switching frequency. This will result in improved spectral characteristics, reduced EMI and increased power densities.

The actively clamped resonant dc link voltage source inverter (ACRDCL) [32] makes a good candidate to replace the hard-switched conventional PWM converters, due to the simplicity of the construction, ease and robustness of control and reduced peak voltage stresses in the devices when compared to other soft-switching configurations [32] [33]. This circuit configuration, as shown in Fig. 3.1 resembles a conventional voltage source inverter with additional LC element and a switch at the front end. This configuration is capable of limiting the peak voltage stresses in the devices to a more reasonable value of 1.2 V_s- 1.5 V_s depending on the design objectives [33].

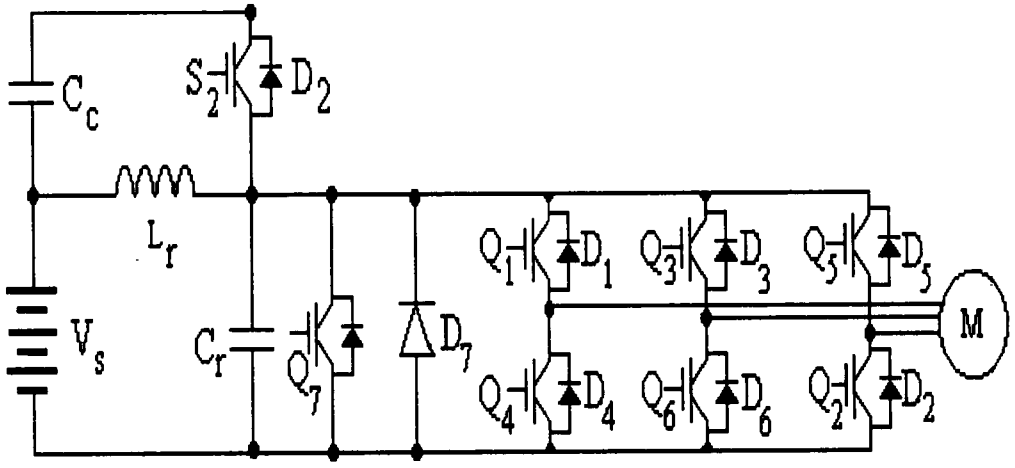


Fig. 3.1 Actively clamped resonant dc link inverter.

3.2 Actively Clamped Resonant DC Link Inverter and Adjacent/Zero State Current Controller with Zero Hysteresis Band

3.2.1 Principle of Operation of Actively Clamped Resonant DC Link Inverter

The voltage and current waveforms of an actively clamped resonant dc link inverter are shown in Fig. 3.2. One resonant cycle consists of five mode of operation [32]. As shown in Fig. 3.3a, mode M_0 occurs while the dc bus is shorted through the switch Q_7. During this period, inductor current increases linearly to I_L as given in equation (3.1).

$$I_L = I_o + I_{iq7} \tag{3.1}$$

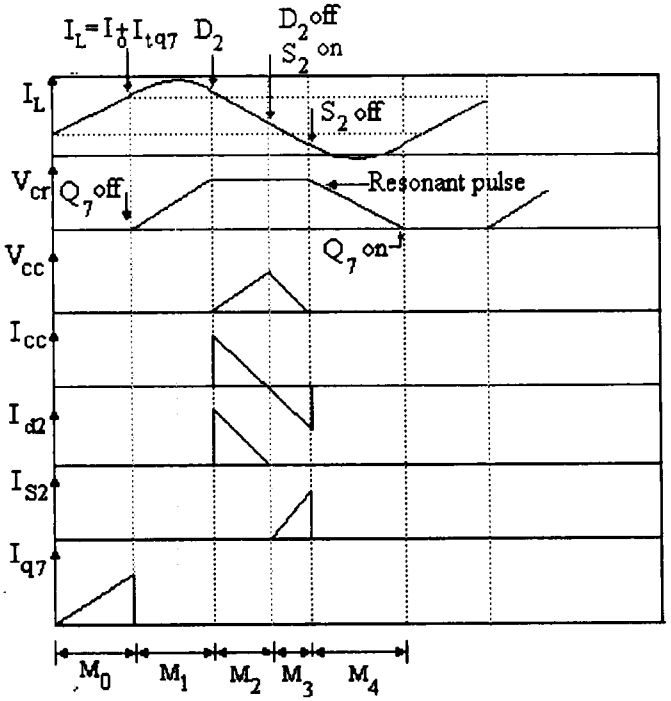
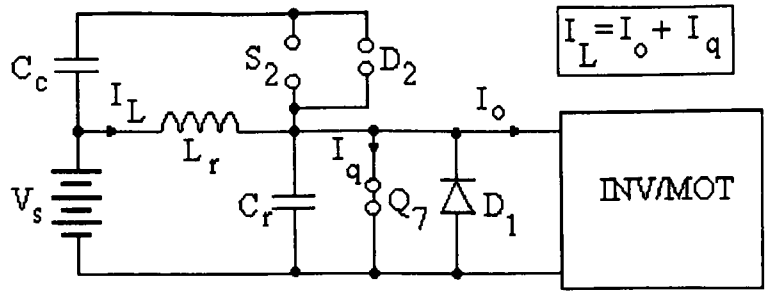


Fig. 3.2 Actively clamped resonant dc link voltage and current waveforms.

Where I_{tq7} is the trip current level established to turn Q_7 off. During mode M_1, capacitor C_r charges up to clamp voltage level as shown in Fig. 3.3b. When the capacitor C_r is charged to the clamp voltage level, the diode D_2 becomes forward biased and the mode of operation switches from M_1 to M_2 . The mode M_2 operation is shown in Fig. 3.3c. The mode M_2 operation prevails until the clamp capacitor current reaches zero, at which point the operation mode is changed from M_2 to M_3 as shown in Fig. 3.3d. The operation mode M_4 starts when the switch S_2 is switched off, forcing the resonant pulse to resonate back to zero voltage. As shown in Fig. 3.2 the switching on and off of main devices Q_1-Q_6 and Q_7 coincide with the zero voltage crossing point of the resonant pulse. The auxiliary devices D_2 and S_2 are also switched when the current through the devices are zero. Thus, the timing diagram for the entire resonant cycle is known and therefore, the maximum possible switching and conduction losses in the inverter can be calculated analytically for drive system efficiency estimation. Fig. 3.4 shows the resonant pulse voltage waveform for one switching cycle.

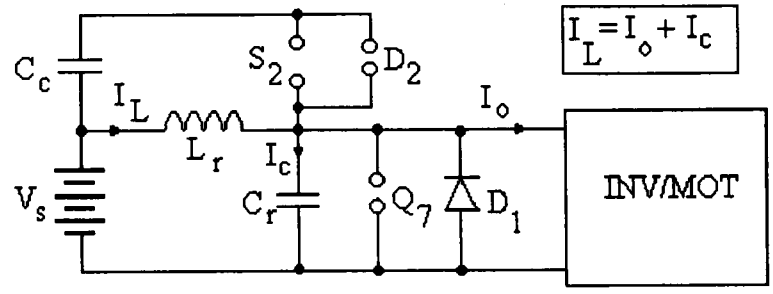
3.2.2 Adjacent/Zero State Current Controller with Zero Hysteresis Band Regulator

The inverter current control configuration uses a special control strategy which reduces the switching voltage stresses of the main devices. This switching method eliminates the $-V_s$ to $+V_s$ transitions. The possible configuration of the inverter switching pattern is shown in Fig. 3.5a. The different switching states are designated as S_o-S_6. As



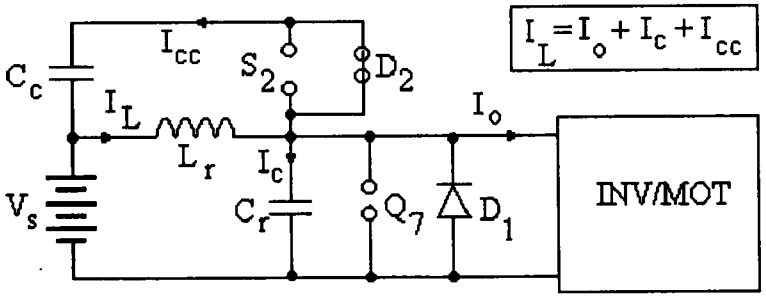
Mode $M_o = [Q_7 = On \quad S_2 = Off \quad D_2 = Off]$

Fig. 3.3a



Mode $M_1 = [Q_7 = Off \quad S_2 = Off \quad D_2 = Off]$

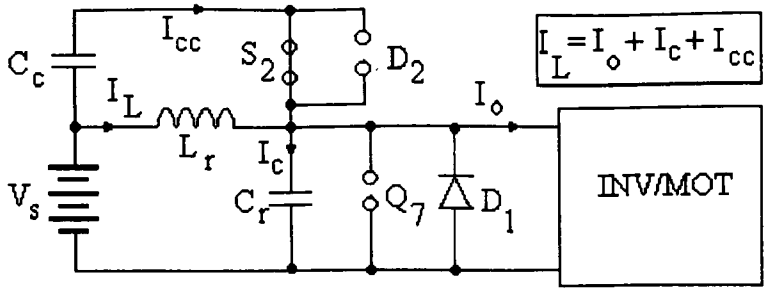
Fig. 3.3b



Mode $M_2 = [Q_7 = Off \quad S_2 = Off \quad D_2 = On]$

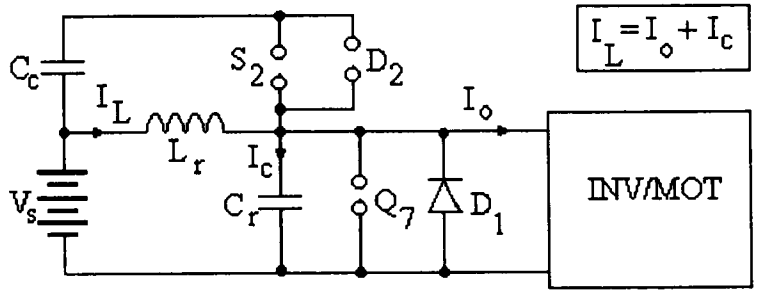
Fig. 3.3c

Fig. 3.3 Modes of operation of the ACRDCL inverter.



Mode $M_3 = [Q_7 = \text{Off}\ \ S_2 = \text{On}\ \ D_2 = \text{Off}]$

Fig. 3.3d



Mode $M_4 = [Q_7 = \text{Off}\ \ S_2 = \text{Off}\ \ D_2 = \text{Off}]$

Fig. 3.3e

Fig. 3.3 (continiued).

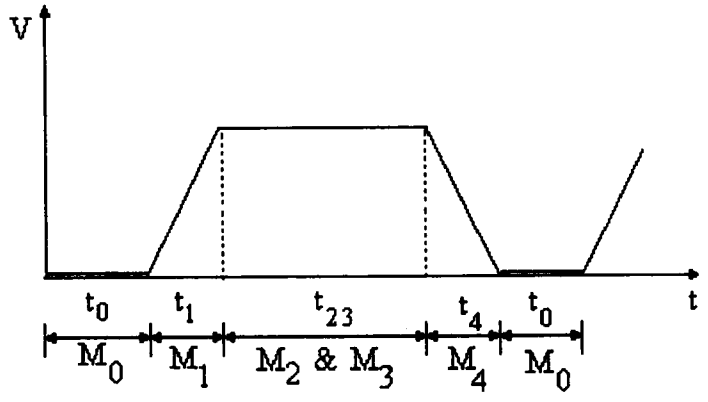


Fig. 3.4 Resonant voltage pulse waveform during one switching cycle.

shown in Fig. 3.5b, the transition from state S_o to any state is allowed by the controller. However, the transition from any other state is allowed only if the controller demanded switching state is adjacent to the present switching state (i.e. if the present switching state is S_1 , then allowed states would be only S_2 , S_0 and S_6). Otherwise , the switching state will remain in the present state or switch to S_0 state depending on the current error signals [35]. The inverter switching state change command is synchronized with the zero crossing of the resonant voltage pulse and is obtained through the sign of the current error signals. Table 3.1 shows the possible signs of the phase current errors and the allowed transitions from a given state. As shown by the column 2 of the Table 3.1, there are only six possible combinations of current error signals. Since the control is based on the sign of the current error signals, there is no fixed hysteresis band associated with the controller. However, the maximum allowed error of the phase current depends on the switching frequency and hence a higher switching frequency will result in a low ripple current.

3.3 Loss Modeling of Inverter Switching Devices

This section describes an analytical method to estimate the ACRDCL inverter device losses for a axial gap brushless motor drive. The motor parameters used in this analysis are the optimized design parameters which is discussed in section 2.5. The inverter main switches and auxiliary devices are assumed to be 3rd generation IGBTs.

Switch Condition						Switching State Designation
Q_1	Q_2	Q_3	Q_4	Q_5	Q_6	
ON	OFF	**ON**	OFF	**ON**	OFF	S_0
ON	**ON**	OFF	OFF	OFF	**ON**	S_1
ON	**ON**	**ON**	OFF	OFF	OFF	S_2
OFF	**ON**	**ON**	**ON**	OFF	OFF	S_3
OFF	OFF	**ON**	**ON**	**ON**	OFF	S_4
OFF	OFF	OFF	**ON**	**ON**	**ON**	S_5
ON	OFF	OFF	OFF	**ON**	**ON**	S_6

Fig. 3.5a

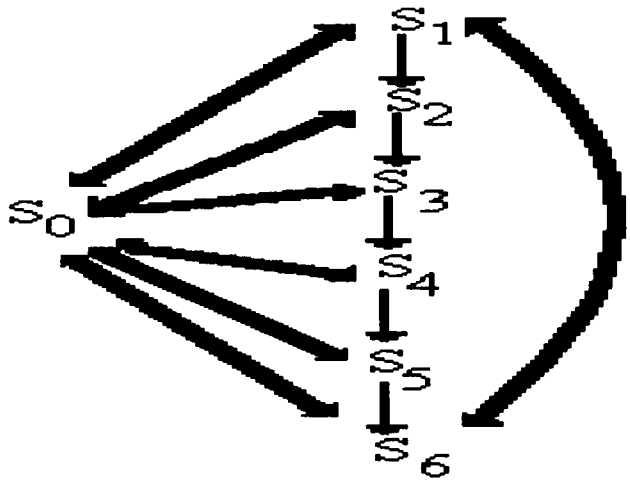


Fig. 3.5b

Fig. 3.5 Inverter switching configuration and allowed transition states.

Table 3.1 Current error signals and allowed switching states.

ERR														
	PSS	NSS	PSS	NSS	PSS	NSS	PSS	NSS	PSS	NSS	PSS	NSS	PSS	NSS
Iac(-)	Q1	Q1	Q1	Q1	Q1	Q1	Q4	Q1	Q4	Q1	Q4	Q1	Q1	Q1
Ibe(+)	Q3	Q6	Q6	Q6	Q3	Q6	Q3	Q6	Q3	Q6	Q6	Q6	Q6	Q6
Ice(+)	Q5	Q2	Q2	Q2	Q2	Q2	Q2	Q2	Q5	Q2	Q5	Q2	Q5	Q2
State	S0	S1	S1	S1	S2	S1	S3	S1	S4	S1	S5	S1	S6	S1
Trans.	AL		NT		AL		NA		NA		NA		AL	
Iac(-)	Q1	Q1	Q1	Q1	Q1	Q1	Q4	Q1	Q4	Q1	Q4	Q1	Q1	Q1
Ibe(-)	Q3	Q3	Q6	Q3	Q3	Q3	Q3	Q3	Q3	Q3	Q6	Q3	Q6	Q3
Ice(+)	Q5	Q2	Q2	Q2	Q2	Q2	Q2	Q2	Q5	Q2	Q5	Q2	Q5	Q2
State	S0	S2	S1	S2	S2	S2	S3	S2	S4	S2	S5	S2	S6	S2
Trans.	AL		AL		NT		AL		NA		NA		NA	
Iac(+)	Q1	Q4	Q1	Q4	Q1	Q4	Q4	Q4	Q4	Q4	Q4	Q4	Q1	Q4
Ibe(-)	Q3	Q3	Q6	Q3	Q3	Q3	Q3	Q3	Q3	Q3	Q6	Q3	Q6	Q3
Ice(+)	Q5	Q2	Q2	Q2	Q2	Q2	Q2	Q2	Q5	Q2	Q5	Q2	Q5	Q2
State	S0	S3	S1	S3	S2	S3	S3	S3	S4	S3	S5	S3	S6	S3
Trans.	AL		NA		AL		NT		AL		NA		NA	
Iac(+)	Q1	Q4	Q1	Q4	Q1	Q4	Q4	Q4	Q4	Q4	Q4	Q4	Q1	Q4
Ibe(-)	Q3	Q3	Q6	Q3	Q3	Q3	Q3	Q3	Q3	Q3	Q6	Q3	Q6	Q3
Ice(-)	Q5	Q5	Q2	Q5	Q2	Q5	Q2	Q5	Q5	Q5	Q5	Q5	Q5	Q5
State	S0	S4	S1	S4	S2	S4	S3	S4	S4	S4	S5	S4	S6	S4
Trans.	AL		NA		NA		AL		NT		AL		NA	

Iac(+)	Q1	Q4	Q1	Q4	Q1	Q4	Q4	Q4	Q4	Q4	Q4	Q4	Q1	Q4
Ibc(+)	Q3	Q6	Q6	Q6	Q3	Q6	Q3	Q6	Q3	Q6	Q6	Q6	Q6	Q6
Icc(-)	Q5	Q5	Q2	Q5	Q2	Q5	Q2	Q5	Q5	Q5	Q5	Q5	Q5	Q5
State	S0	S5	S1	S5	S2	S5	S3	S5	S4	S5	S5	S5	S6	S5
Trans.	AL		NA		NA		NA		AL		NT		AL	
Iac(-)	Q1	Q1	Q1	Q1	Q1	Q1	Q4	Q1	Q4	Q1	Q4	Q1	Q1	Q1
Ibc(+)	Q3	Q6	Q6	Q6	Q3	Q6	Q3	Q6	Q3	Q6	Q6	Q6	Q6	Q6
Icc(-)	Q5	Q5	Q2	Q5	Q2	Q5	Q2	Q5	Q5	Q5	Q5	Q5	Q5	Q5
State	S0	S6	S1	S6	S2	S6	S3	S6	S4	S6	S5	S6	S6	S6
Trans.	AL		AL		NA		NA		NA		AL		NT	

PSS= Present switching state NSS= Next switching state

AL= Transition allowed NA = Transition not allowed

NT= No transition occur

3.3.1 Main Device Losses (Q_1-Q_6)

Inverter main switching devices (Q_1-Q_6) are switched on and off at the zero crossing of the resonant link voltage which appears on the main dc link. Therefore, no switching losses will occur in the main devices. The losses in the main devices are mainly due to conduction. In addition to that the anti-parallel diodes losses occur during the current change over from the main devices to diodes and vice versa. However, in these calculations the main diode losses are neglected and it is assumed that current transfer occurs from one main device to another without a dead time period. This assumption will result in a slight over estimation of the losses and will not cause any errors in the final results, because the main objective is to find the optimum values of the resonant link devices and the frequency at which the system losses are minimum. The conduction losses are given by equation (3.2), since at any given time only two main devices are conducting.

$$\text{Conduction losses, } P_{QC} = 2V_{ces}I_o \quad \text{(W)} \tag{3.2}$$

where V_{ces} = Device collector to emitter saturation voltage

I_o = Load current

There is an additional loss component associated with the main devices during the switch off period. This is due to the fact that the additional current (Inductor current less the load current) which is flowing through the auxiliary device Q_7, is transferred to the capacitor C_r, boosting up the dc link voltage from zero during the device switch off. This additional loss component is given by the equation (3.3) assuming the over-snubbed switch off conditions as shown in Fig. 3.6 [33].

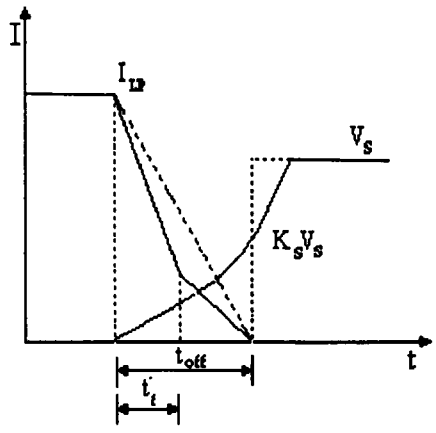


Fig. 3.6 Over-snubbed switch off waveform of an IGBT

Maximum possible switch off losses , $P_{Qsw} = \dfrac{(I_{LPL} - I_o)^2 t_f^2 f_{lk}}{24C_r}$ (W) (3.3)

where I_{LPL} = Inductor peak current

t_f = IGBT fall time

f_{lk} = Resonant link frequency

C_r = Resonant capacitance

Equation (3.3) shows that high value of the resonant capacitor lowers the additional switch off loss component. However, high value of resonant capacitance will reduce the value of resonant inductance for a given value of switching frequency. This may not be a good design criterion since the resonant inductance could not be lowered beyond a certain value due to the stray inductance involved in the circuit.

3.3.2 Auxiliary Device, Q_7 Losses

As shown in Fig. 3.2, the auxiliary device Q_7 is switched on and off at the resonant pulse zero crossings. Therefore, the device will not incur losses due to switching

operations. However, as explained in section 3.3.1, during switch off, the current may flow into the resonant capacitor and boost the dc link voltage to a value above zero. This may result in some switch off losses within the device Q_7. The maximum possible value of this component is given by equation (3.4).

Maximum possible switch off losses in Q_7 , $P_{Q7sw} = \frac{I_{tq}^2 t_f^2 f_{lk}}{24C_r}$ (W) (3.4)

where $I_{tq7} = \frac{I_o}{K_t}$ = Trip current of Q_7

K_T = Trip current constant

The conduction losses in the device Q_7 is given by equation (3.5)

Conduction losses in Q_7, , $P_{Q7C} = (I_{LPL} - I_o)V_{ces}t_o f_{lk}$ (3.5)

where I_{LPL} = Inductor peak current with load

The peak current in the inductor under no-load conditions is given by equation (3.6) [37].

$$I_{LP} = \sqrt{\left(\frac{V_s t_o}{L_r}\right)^2 + \left(V_s\sqrt{\frac{C_r}{L_r}}\right)^2} \quad (3.6)$$

The peak current in the inductor under load, I_{LPL} , is then given by the sum of peak load current and peak inductor current. This is given by equation (3.7) [37].

$$I_{LPL} = I_{LP} + I_o \quad (3.7)$$

Equation (3.4) shows that by keeping Q_7 trip current level low, the losses can be reduced during switch off. However, the trip current level should be selected such that there is enough energy stored in the inductor, to make sure that the link can resonate back

to zero voltage at the end of mode M_4. In general the trip current level is set around 25-35% of full load current [37].

3.3.3 Auxiliary Switch, S_2 Losses

The auxiliary switch S_2 is always switched on when the clamp circuit current is zero. Therefore, the device will not have switch-on losses due to zero current switching. However, the device will have the conduction losses and the switch-off losses. Fig. 3.7 shows the current and voltage waveforms of S_2. For simplicity, the voltage drop across the device is assumed to be equal to saturation voltage during the current build up. By using Fig. 3.7, an equation for the current through the device S_2, I_{s21}, can be obtained assuming a linear approximation and is given in equation (3.8).

$$I_{s21} = I_{CP}\frac{2t}{t_{23}} \tag{3.8}$$

where I_{CP} = Peak current through the capacitor

t_{23} = Half of the clamping time (shown in Fig. 3.4)

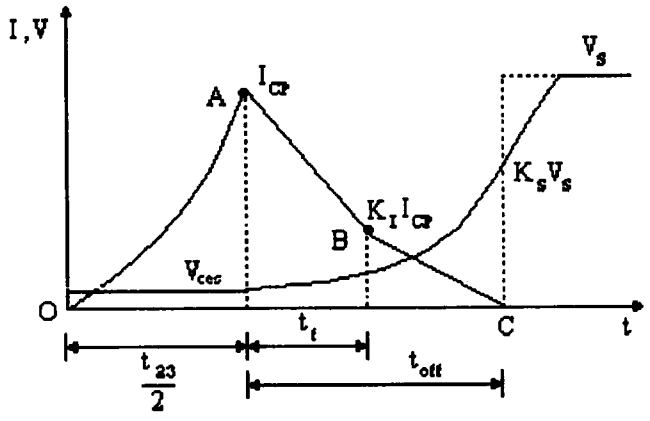


Fig. 3.7 Current and voltage waveforms of auxiliary switch S_2.

The peak current through the resonant link capacitor is given by equation (3.9) [37].

$$I_{CP} = \sqrt{(I_o)^2 + (2K_v - K_v^2)\left[V_s\sqrt{\frac{C_r}{L_r}}\right]^2} \tag{3.9}$$

The switch off losses, P_{s1}, of the device from time 0 to $\frac{t_{23}}{2}$ is given by equation (3.10).

$$P_{s1} = \int_0^{\frac{t_{23}}{2}} I_{s21} V_{ces} dt \qquad \text{(J)} \quad \text{per resonant pulse} \tag{3.10}$$

Equation (3.10) can be simplified to equation (3.11)

$$P_{s1} = \frac{I_{CP}}{4} t_{23} V_{ces} \quad \text{(J)} \quad \text{per resonant pulse} \tag{3.11}$$

Assuming a linear current decay through the device, the current from time $\frac{t_{23}}{2}$ to $\frac{t_{23}}{2} + t_f$, I_{s22} can be approximated by equation (3.12)

$$I_{s22} = I_{CP}\left[1 - (1 - K_I)\frac{t}{t_f}\right] \tag{3.12}$$

The collector to emitter voltage build up within the device during switch off is shown in Fig. 3.7. Assuming a linear increase in the voltage from time $\frac{t_{23}}{2}$ to $\frac{t_{23}}{2} + t_{off}$, the switch off losses, P_{s2}, of the device from time $\frac{t_{23}}{2}$ to $\frac{t_{23}}{2} + t_f$ can be approximated by equation (3.13).

$$P_{s2} = \int_0^{t_f} I_{CP}\left[1 - (1 - K_I)\frac{t}{t_f}\right] K_s V_s \frac{t}{t_{off}} dt \qquad \text{(J) per resonant pulse} \tag{3.13}$$

where K_I = Constant related to IGBT current fall characteristics.

K_s = Over-snubbed constant

t_{off} = IGBT switch off time.

Equation (3.13) simplifies to equation (3.14).

$$P_{s2} = \frac{I_{CP}}{t_{off}} K_s V_s \left[\frac{t_f^2}{2} - (1 - K_I) \frac{t_f^2}{3} \right] \quad \text{(J) per resonant pulse} \qquad (3.14)$$

During the tail time (from point B to C in Fig. 3.7), the device current, I_{s23} , can be approximated by equation (3.15).

$$I_{s23} = \frac{K_I I_{CP}}{(t_{off} - t_f)} (t_{off} - t) \qquad (3.15)$$

The device power losses during tail time, P_{s3}, can be written as:

$$P_{s3} = \int_{t_f}^{t_{off}} \frac{K_I I_{CP}}{(t_{off} - t_f)} (t_{off} - t) K_s V_s \frac{t}{t_{off}} dt \quad \text{(J) per resonant pulse} \qquad (3.16)$$

Equation (3.16) can be simplified as shown in equation (3.17).

$$P_{s3} = \frac{K_s K_I V_s I_{CP}}{t_{off}(t_{off} - t_f)} \left[\frac{t_{off}^3}{6} + t_f^2 \left(\frac{t_f}{3} - \frac{t_{off}}{2} \right) \right] \quad \text{(J) per resonant pulse} \qquad (3.17)$$

3.3.4 Auxiliary Diode, D_2 Losses

The auxiliary diode, D_2 is always switched off when the diode current is zero. Hence this device will not incur any switch-off losses due to zero current switching. However, this will have some switch-on losses and conduction losses. Fig. 3.8 shows the

auxiliary diode switching waveforms without considering the diode reverse recovery waveform. The voltage and current waveforms of the diode D_2 during switch on can be approximated by linear relationships as shown in equations (3.18) and (3.19).

$$V_D = (K_v - 1)V_s\left(1 - \frac{t}{t_r}\right) \tag{3.18}$$

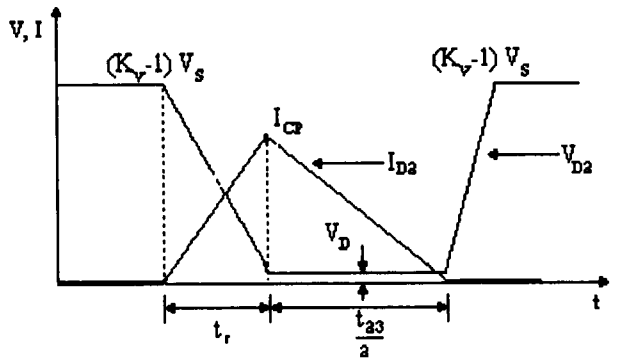


Fig. 3.8 Current and voltage waveforms for auxiliary diode, D_2.

$$I_D = I_{CP}\frac{t}{t_r} \tag{3.19}$$

where t_r = Rise time of diode.

The switch on losses of auxiliary diode D_2, P_{Dsw}, can be approximated by equation (3.20) and can be simplified as shown in equation (3.21).

$$P_{DSW} = \int_0^{t_r} I_{CP}\frac{t}{t_r}(K_v - 1)V_s\left(1 - \frac{t}{t_r}\right)dt \quad \text{(J) per resonant pulse} \tag{3.20}$$

$$P_{DSW} = (K_v - 1)V_s\frac{I_{CP}}{t_r}\left(\frac{t_r^2}{2} - \frac{t_r^2}{3}\right) \quad \text{(J) per resonant pulse} \tag{3.21}$$

The auxiliary diode current during the clamping period can be approximated by the linear equation as shown in equation (3.22).

$$I_D = I_{CP}\left(1-\frac{2t}{t_{23}}\right) \tag{3.22}$$

The conduction losses of D_2 during the clamping period, P_{DC} , then can be calculated by using equation (3.23).

$$P_{DC} = \int_0^{\frac{t_{23}}{2}} I_{CP}V_D\left(1-\frac{2t}{t_{23}}\right)dt \quad \text{(J) per resonant pulse} \tag{3.23}$$

Equation (3.23) simplifies to equation (3.24)

$$P_{DC} = I_{CP}V_D\frac{t_{23}}{4} \quad \text{(J) per resonant pulse} \tag{3.24}$$

The individual device losses calculated above are estimated at the worst case conditions and therefore, represent the maximum possible total losses within the devices. These losses can be added together to obtain the inverter total power loss, P_{LT} .

$$P_{LT} = \left\{P_{L(Q_1-Q_6)}\right\}+\left\{P_{L(Q_7)}\right\}+\left\{P_{L(S_2)}\right\}+\left\{P_{L(D_2)}\right\} \tag{3.25}$$

where $P_{L(Q_1-Q_6)}$ = Total power loss in main devices, Q_1-Q_6.

$P_{L(Q_7)}$ = Total power loss in auxiliary device Q_7.

$P_{L(S_2)}$ = Total power loss in switch S_2.

$P_{L(D_2)}$ = Total power loss in auxiliary diode D_2.

Equation (3.25) can be rewritten in terms of conduction and switching losses of the individual devices.

$$P_{LT} = \{P_{QC} + P_{QSW}\} + \{P_{Q7C} + P_{Q7SW}\} + \{(P_{s1} + P_{s2} + P_{s3})f_{lk}\} + \{(P_{DC} + P_{DSW})f_{lk}\} \quad (3.26)$$

where P_{QC} = As defined in equation (3.2)

P_{QSW} = As defined in equation (3.3)

P_{Q7SW} = As defined in equation (3.4)

P_{Q7C} = As defined in equation (3.5)

P_{s1} = As defined in equation (3.10)

P_{s2} = As defined in equation (3.13)

P_{s3} = As defined in equation (3.17)

P_{DSW} = As defined in equation (3.21)

P_{DC} = As defined in equation (3.24)

3.4 ACRDCL Efficiency Estimation for a Brushless DC Motor Drive

This section describes the efficiency estimation procedure for the ACRDCL inverter. The machine ratings and inverter devices data used in the estimation are shown in Table 3.2 and Table 3.3 respectively.

3.4.1 Resonant Pulse Timing and Resonant Devices Peak Current Calculations

The resonant pulse timing calculations presented in this section assume the resonant link frequency of 60 kHz. First, the resonant inductance should be selected such that the stray inductance in the circuit will not dominate during the operation of the

inverter. During the time period in which the auxiliary transistor Q_7 is shorted (in Mode M_0) the inductor current increases linearly. The inductor selection must ensure that at the end of this mode of operation, there is enough energy stored in the inductor such that the link can resonate back to zero volt during the switching cycle. This condition is satisfied if the inductor current rises to about 25-33% of the maximum output current during mode M_0 operation [37].

This assumption results in:

$$L_{rMax} = 4\frac{V_s t_o}{I_o} \tag{3.27}$$

$$L_{rMin} = 3\frac{V_s t_o}{I_o} \tag{3.28}$$

A value between 5-20 mH is reasonable for the resonant inductance depending on the resonant frequency at which the ACRDCL is operated [37]. Assuming a resonant inductor value to be 8 mH , the following estimations can be made.

By using equation (3.27) and assuming a current build up of 25% of the maximum load current in the resonant inductor,,

$$t_o = \frac{360 * 8 * 10^{-6}}{216 * 4} = 3.333 \text{ ms} \tag{3.29}$$

Assuming a link frequency of 60 kHz, the resonant capacitance can be calculated using equation (3.30).

$$60 * 10^3 = \frac{1}{2\pi\sqrt{C_r * 8 * 10^{-6}}} \tag{3.30}$$

$$C_r = 880 \text{ nF} \tag{3.31}$$

Since the resonant link frequency is 60 kHz, the period, T, of the resonant pulse is 16.66 ms.

From Fig. 3.4, $$T = 16.66 = t_o + t_1 + t_{23} + t_4 \quad (3.32)$$

Now assuming the clamping factor to be 1.3 (i.e. K_v =1.3), the resonant pulse rise, clamping and fall time can be calculated by using equations (3.33) and (3.35) [32].

$$16.66 * 10^{-6} = \frac{1.3}{(1.3-1)}(t_1 + 3.333) \quad (3.33)$$

$$t_1 = t_4 = 0.5116 \text{ ms} \quad (3.34)$$

$$t_{23} = \frac{t_o + t_1(2 - K_v)}{(K_v - 1)} \quad (3.35)$$

$$t_{23} = \frac{3.333 + 0.5116(2 - 1.3)}{(1.3-1)} = 12.303 \text{ ms} \quad (3.36)$$

The no-load peak current in the resonant inductor and peak current under load can be calculated by using equations (3.6), (3.7).

The no-load peak current in the inductor, I_{LP}:

$$I_{LP} = \sqrt{\left(\frac{216 * 3.333 * 10^{-6}}{8 * 10^{-6}}\right)^2 + \left(216\sqrt{\frac{880 * 10^{-9}}{8 * 10^{-6}}}\right)^2} = 115.02 \quad \text{Amps} \quad (3.37)$$

The maximum possible peak current in the inductor under load conditions, I_{LPL}:

$$I_{LPL} = 360 + 115.02 = 475.02 \quad \text{Amps} \quad (3.38)$$

The peak current in the resonant capacitor can be calculated using equation (3.9).

$$I_{CP} = \sqrt{(360)^2 + (2.6 - 1.3^2)\left[216\sqrt{\frac{880 * 10^{-9}}{8 * 10^{-6}}}\right]^2} = 366.42 \quad \text{Amps} \quad (3.39)$$

Table 3.2 Ratings of the brushless dc machine used in efficiency estimation.

Parameter	Value	Units
DC link voltage	216	Volts
Rated machine current	360	Amps
L-L back emf @ 3200 rpm	207	Volts
Rated horse power	100	Hp
Rated speed	3200	RPM

Table 3.3 Inverter devices data

Parameter	Symbol	Ratings	Units
Collector-Emitter voltage	V_{CES}	600	Volts
Collector current	I_C	400	Amps
Max. power dissipation	P_C	1600	Watts
Collector-Emitter saturation voltage	$V_{CE(SAT)}$	3.5	Volts
Turn-on time	t_{on}	0.6	ms
	t_r	0.4	ms
Turn-off time	t_{off}	0.7	ms
	t_f	0.2	ms
Constant of fall characteristics	K_I	0.2	-
Diode forward on-voltage	V_F	2.5	Volts
Rise time	t_R	0.25	ms

3.4.2 ACRDCL Efficiency Estimation

The inverter device power losses can now be estimated using the results of section 3.3 and section 3.4.1. The inverter main device losses can be estimated using equations (3.2), (3.3), data in Table 3.2 and Table 3.3.

Main devices conduction losses, $P_{QC} = 2 * 3.5 * 360 = 2520$ (W) (3.40)

Neglecting the tail time, max. possible switch off losses, P_{Qsw}:

$$P_{Qsw} = \frac{(475.02 - 360)^2 (0.7 * 10^{-6})^2 60 * 10^3 * 2}{24(880 * 10^{-9})} = 36.90 \quad \text{(W)} \tag{3.41}$$

Maximum possible conduction losses, P_{Q7C} , in auxiliary device Q_7:

$$P_{Q7C} = (475.02 - 360)3.5 * 3.333 * 10^{-6} * 60 * 10^3 = 80.50 \quad \text{(W)} \tag{3.42}$$

Assuming the trip current level to be peak inductor no-load current, the switching losses in the auxiliary device can be estimated using equation (3.4).

$$P_{Q7sw} = \frac{115.02^2 * (0.7 * 10^{-6})^2 * 60 * 10^3}{24 * 880 * 10^{-9}} = 18.45 \quad \text{(W)} \tag{3.43}$$

The three loss components, P_{s1} ,P_{s2} , and P_{s3} of the auxiliary switch S_2 can be estimated by using equations (3.11), (3.14) and (3.17) respectively.

$$P_{s1} = \frac{366.42 * 12.303 * 10^{-6} * 3.5 * 60 * 10^3}{4} = 236.71 \quad \text{(W)} \tag{3.44}$$

$$P_{s2} = \frac{366.42}{0.7 * 10^{-6}} 0.5 * 216 \left[\frac{0.2^2}{2} - (1 - 0.2) \frac{0.2^2}{3} \right] 10^{-12} * 60 * 10^3 = 37.97 \text{ (W)} \tag{3.45}$$

$$P_{s3} = \frac{0.5*0.2*216*366.42}{0.7(0.7-0.2)}\left[\frac{0.7^3}{6}+0.2^2\left(\frac{0.2}{3}-\frac{0.7}{2}\right)\right]10^{-6}*60*10^3 = 74.59 \text{ (W)} \quad (3.46)$$

The auxiliary diode power losses P_{DSW} and P_{DC} can be estimated using equations (3.21) and (3.24).

$$P_{DSW} = (1.3-1)*216\frac{366.42}{0.25}\left(\frac{0.25^2}{2}-\frac{0.25^2}{3}\right)10^{-6}*60*10^3 = 59.33 \quad \text{(W)} \quad (3.47)$$

$$P_{DC} = 366.42*2.5\frac{12.303*10^{-6}}{4}*60*10^3 = 169.08 \quad \text{(W)} \quad (3.48)$$

The total power loss of the inverter is given by the summation of equations (3.40) to (3.48).

Total power loss of ACRDCL, $P_{TL} = 3236.39$ (W) (3.49)

Out put power from the inverter to motor, $P_o = 207*360 = 74520$ (W) (3.50)

ACRDCL efficiency, $$\eta = \frac{74520}{74520+3237} = 95.83\% \quad (3.51)$$

3.5 Efficiency Optimization of the ACRDCL Inverter

The efficiency maximization of the ACRDCL inverter can be achieved by minimizing the inverter switching and conduction losses for a given switching frequency. The total power losses of the inverter is given by equation (3.26). This can be used as the objective function which is to be minimized during the optimization process. Therefore, the objective function can be stated as:

$$\text{Min}\left\{\left\{P_{QC}+P_{QSW}\right\}+\left\{P_{Q7C}+P_{Q7SW}\right\}+\left\{(P_{s1}+P_{s2}+P_{s3})f_{lk}\right\}+\left\{(P_{DC}+P_{DSW})f_{lk}\right\}\right\} \quad (3.52)$$

The parameters in the above equation are defined in equation (3.26)

From the analysis in section 3.3 it is clear that all loss components except P_{QC} , are dependent on resonant link parameters. Therefore, P_{QC} can be eliminated from the objective function. It is also obvious that the minimum device losses always occur when the K_s and K_T values are minimum. Therefore, if required, they can be set to their minimum values before the optimization process begins. Then the objective simply becomes finding the optimum resonant capacitance and inductance, at which the device losses are minimum. The range of resonant link capacitance and inductance depend on the application and the inverter control configuration. Given these conditions, the optimization problem can be formulated for a general case as follows:

$$\text{Min}\left\{P_{QSW} + \left\{P_{Q7C} + P_{Q7SW}\right\} + \left\{(P_{s1} + P_{s2} + P_{s3})f_{lk}\right\} + \left\{(P_{DC} + P_{DSW})f_{lk}\right\}\right\} \tag{3.53}$$

Subject to:

$$L_r \geq 6 * 10^{-6} \tag{3.54}$$

$$C_r \geq 8 * 10^{-9} \tag{3.55}$$

$$2 \leq K_T \leq 4 \tag{3.56}$$

$$1.3 \leq K_v \leq 1.5 \tag{3.57}$$

$$0.50 \leq K_s \leq 1.0 \tag{3.58}$$

$$K_I = 0.2 \tag{3.59}$$

$$f_{lk} = f_o \tag{3.60}$$

where f_o is the frequency of the resonant link.

Equations (3.53)-(3.60) can be programmed into QPRO optimizer in order to get the optimum parameters for a given switching frequency of the resonant link. Table 3.4 shows the optimum resonant capacitance, inductance, minimum switching losses and optimum efficiency for switching frequencies from 5 kHz to 75 kHz. The Table 3.4 also shows that a significant improvement cannot be achieved in the inveter efficiency since the main power loss component of the inverter, the main device conduction losses, are independent of the resonant link parameters. This amounts to 2522 Watts, while the total power losses vary from 2842 Watts to 3266 Watts depending on the inverter switching frequency. The only way to reduce the main devices conduction losses is to use devices with low saturation voltages. Table 3.4 shows that the efficiency is high at lower frequencies. However, the switching frequency selection should also consider the ripple current, transient response, spectral characteristics , acoustic noise and compactness of the drive system. These performance parameters are very much improved when the switching frequency is at the higher end. Therefore, selection of the switching frequency is a trade-off depending on the application requirements of the drive system. Fig. 3.9 and Fig. 3.10 show the optimum efficiency and the minimum switching losses variation as the switching frequency is varied from 5 kHz to 75 kHz. Fig. 3.11 and Fig. 3.12 show the switching losses for different optimum values of link capacitance and inductance. Fig. 3.13 shows the optimum capacitance and the inductance associated with switching frequencies ranging from 5 kHz to 75 kHz.

Table 3.4 Optimum parameters for ACRDCL inverter.

Switching frequency (kHz)	**Efficiency (%)**	**Power Loss (W)**	**Capacitance (μF)**	**Inductance (mH)**
5	96.33	2842	49.7	20.4
10	96.32	2851	16.0	15.8
15	96.29	2871	9.93	11.3
20	96.27	2891	6.79	9.33
25	96.24	2915	4.78	8.48
30	96.21	2941	3.43	8.20
35	96.17	2969	2.56	8.06
40	96.13	3001	1.97	8.05
45	96.09	3034	1.56	8.03
50	96.05	3068	1.26	8.02
55	96.00	3104	1.05	8.01
60	95.96	3142	0.88	8.00
65	95.91	3182	0.75	8.00
70	95.86	3222	0.65	8.00
75	95.81	3266	0.56	8.00

Table 3.4 shows that the efficiency is high at lower frequencies. However, the switching frequency selection should also consider the ripple current, transient response, spectral characteristics, acoustic noise and compactness of the drive system. These performance parameters are very much improved when the switching frequency is at the higher end. Therefore, selection of the switching frequency is a trade-off depending on the application requirements of the drive system. Fig. 3.9 and Fig. 3.10 show the optimum efficiency and the minimum switching losses variation as the switching frequency is varied from 5 kHz to 75 kHz. Fig. 3.11 and Fig. 3.12 show the switching losses for different optimum values of link capacitance and inductance. Fig. 3.13 shows the optimum capacitance and the inductance associated with switching frequencies ranging from 5 kHz to 75 kHz.

3.6 A Summary of the Drive System Performance Parameters

Table 3.5 summarizes the non-optimized and optimized performance parameters for the ACRDCL inverter/ axial gap brushless dc motor drive system. This shows that the main device conduction losses remain constant even after the optimization process. However, there is a decrease in auxiliary device losses after the optimization. This also shows that by the design optimization process, the overall drive efficiency can be increased from 91.28% to 94.46%.

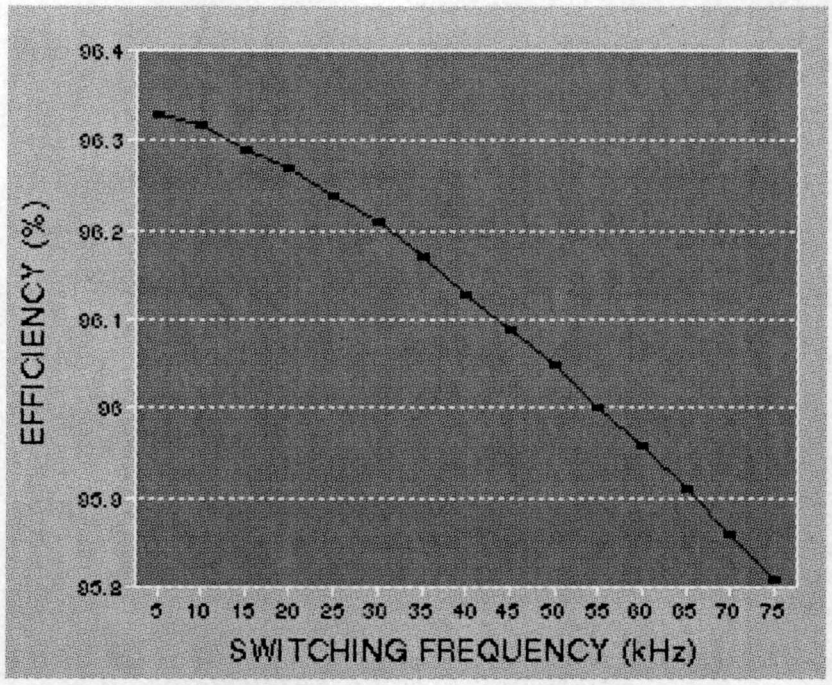


Fig. 3.9 Drive efficiency Vs. switching frequency.

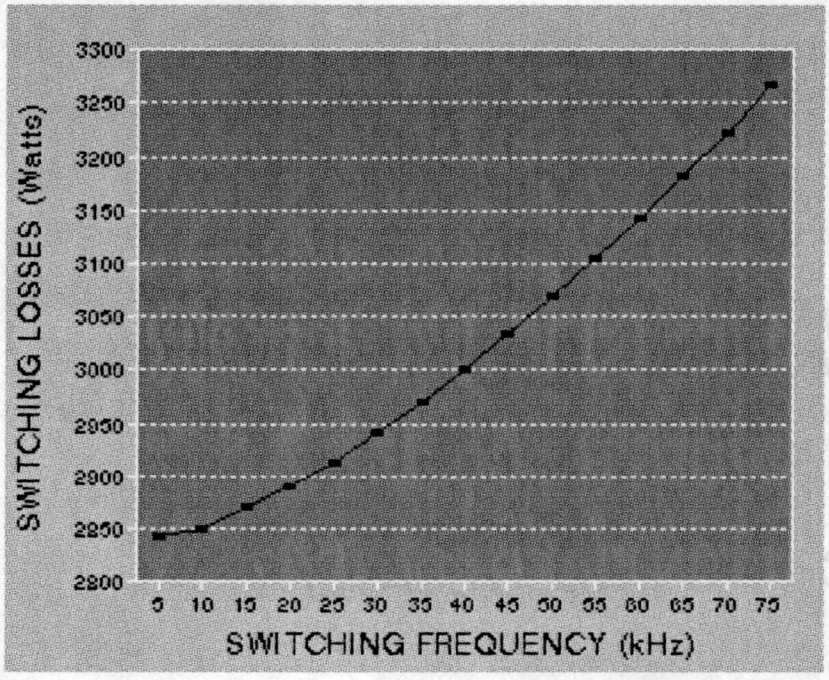


Fig. 3.10 Switching losses Vs. switching frequency.

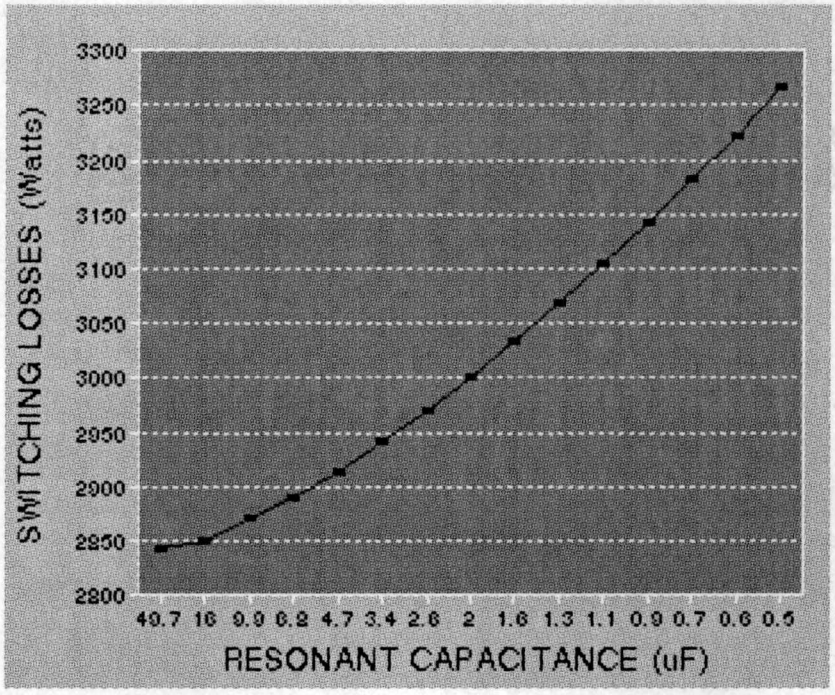


Fig. 3.11 Switching losses Vs. Resonant capacitance.

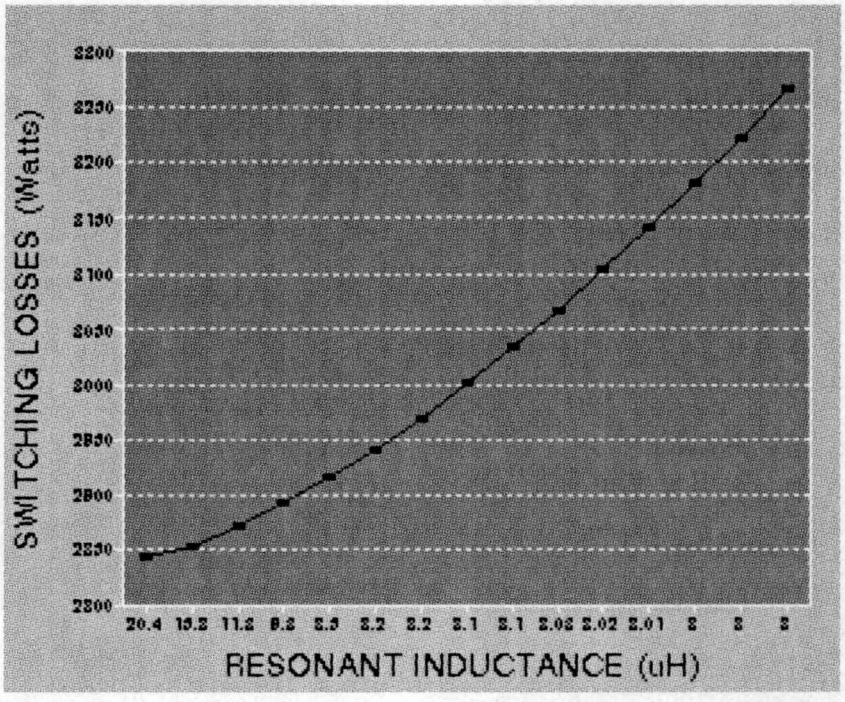


Fig. 3.12 Switching losses Vs. resonant inductance.

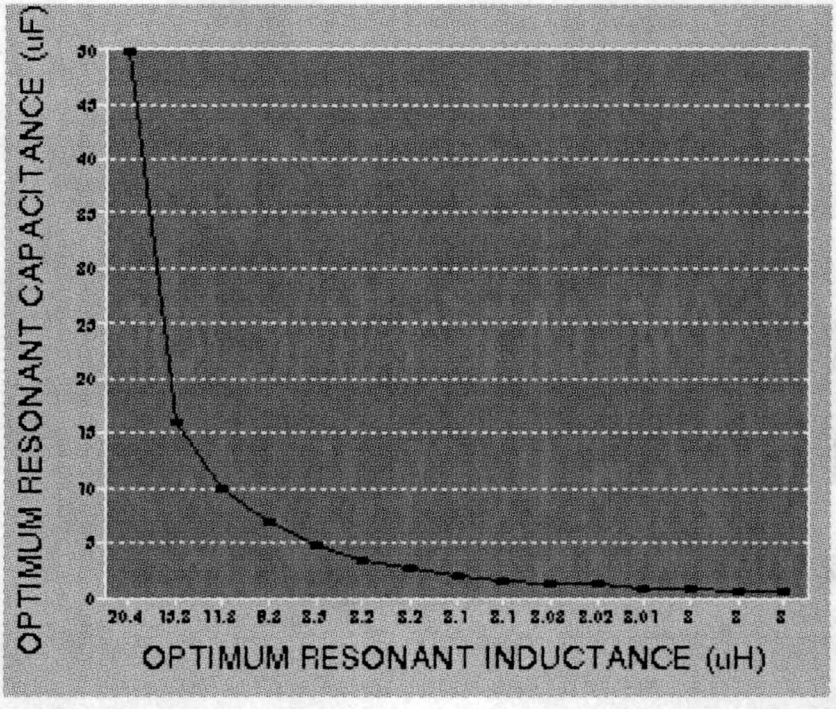


Fig. 3.13 Optimum resonant capacitance Vs. optimum resonant inductance.

Table 3.5 Non-optimal and optimal performance parameters for ACRDCL/ axial gap brushless motor drive system.

Ratings and Parameters	**Non optimized**	**Optimized (f_{sw}=60 kHz)**	**Optimized (f_{sw}= 5 kHz)**	**Units**
Motor:				
DC link voltage	216	216	216	Volts
Rated speed	3200	3200	3200	Rpm
Rated power	100	100	100	Hp
Rated back emf	203	207	207	Volts
Rated current	368	360	360	Amps
Motor efficiency	95.20	98.06	98.06	%
Inverter:				
Link Capacitance	8E -06	8E-06	2.64E-05	F
Link Inductance	8.8E-07	8.8E-07	4.97E-05	H
Capacitor Peak I	366.23	364.37	440.32	Amps
Inductor Peak I	115.09	115.02	349.13	Amps
Device Losses				
Main (Q_1-Q_6)				
Conduction	2522	2522	2522	Watts
Switching	37	37	0.50	Watts
Aux. device , Q_7				
Conduction	81	81	52	Watts
Switching	18	18	0.25	Watts
Aux. device, S_2				

Conduction	237	170	145	Watts
Switching	75	94	9.4	Watts
Aux. diode, D_2				
Conduction	169	122	103	Watts
Switching	60	98	10	Watts
Auxiliary losses	676	619	320	Watts
Total losses	3199	3142	2843	Watts
Inverter efficiency	95.89	95.96	96.33	%
Drive efficiency	**91.28**	**94.09**	**94.46**	%

CHAPTER 4

AN ANALYTICAL SOLUTION FOR THE NO-LOAD FLUX DISTRIBUTION WITHIN THE AIR GAP

4.1 Introduction

Modern electrical machines are normally required to operate at high power density levels with a high degree of reliability and at minimum cost and improved efficiency. Such requirements necessitate a high degree of accuracy in predicting the machine performance. The machine performance is greatly dependent on the air gap flux density waveform which in turn depends on the magnet configuration, air gap length, number of magnet poles, direction of magnetization, etc.. Therefore, it is essential for the machine designer to obtain a clear understanding of the flux density distribution within the machine which leads to the optimal design configuration in terms of magnetic parameters and machine performance.

4.2 Mathematical Formulation to Obtain the Solution for Flux Components B_r, B_θ and B_z

Mathematical formulation for this problem is obtained by using the basic Maxwell's equations for magnetic fields. In this approach the magnetic flux density, B, is described by a non-linear three dimensional partial differential equation in three dimensions [39]. Then the most general form of the solution for B_r, B_θ and B_z is obtained (appendix A1). This solution can be modified according to the specific condition and the region over which the solution is sought [39]. The same form of solution can be used to calculate the

eddy current and hence the core losses in the stator. In deriving this general solution it is assumed that inside the electric machine, electrostatic flux density and charge density are very small and therefore can be considered to be zero [42]. Under these assumptions, the problem becomes that of computing the coupled current and flux distribution whose linkages are defined by [49]

$$\text{Curl } H = J \tag{4.1}$$

$$\text{Curl } E = -\frac{\partial B}{\partial t} \tag{4.2}$$

$$\text{Div } B = 0 \tag{4.3}$$

The geometry of the two sets of flow paths is controlled by the material properties defined by the following equations:

$$E = \rho J \tag{4.4}$$

$$B = \mu H \tag{4.5}$$

Equations (4.2) and (4.4) result in

$$\text{Curl } (\rho J) = -\frac{\partial B}{\partial t} \tag{4.6}$$

Equations (4.6) and (4.1) give

$$\text{Curl } (\rho \,.\text{Curl } H) = -\frac{\partial B}{\partial t} \tag{4.7}$$

Equations (4.5) and (4.7) yield

$$\text{Curl } .\text{ Curl } (B) + \frac{\mu}{\rho}\,\frac{\partial B}{\partial t} = 0 \tag{4.8}$$

By considering the z component of equation (4.8)

$$\frac{1}{r}\left[\frac{\partial}{\partial r}\left\{r\left(\frac{\partial B_r}{\partial z}-\frac{\partial B_z}{\partial r}\right)\right\}-\frac{\partial}{\partial \theta}\left(\frac{1}{r}.\frac{\partial B_z}{\partial \theta}-\frac{\partial B_\theta}{\partial z}\right)\right]+\frac{\mu}{\rho}\frac{\partial B_z}{\partial t}=0 \qquad (4.9)$$

$$\frac{1}{r}\left[\frac{\partial^2}{\partial r.\partial z}(rB_r)-\frac{\partial}{\partial r}\left(r.\frac{\partial B_z}{\partial r}\right)-\frac{1}{r}.\frac{\partial^2 B_z}{\partial \theta^2}+\frac{\partial^2 B_\theta}{\partial \theta.\partial z}\right]+\frac{\mu}{\rho}\frac{\partial B_z}{\partial t}=0 \qquad (4.10)$$

Now we can make use of equation (4.3), which is

$\frac{\partial}{\partial r}(rB_r)+\frac{1}{r}\frac{\partial}{d\theta}(rB_\theta)+r\frac{\partial B_z}{\partial z}=0$ and simplifying yields

$$\frac{\partial^2}{\partial r.\partial z}(rB_r)+\frac{1}{r}.\frac{\partial^2}{\partial \theta.\partial z}(rB_\theta)+r\frac{\partial^2 B_z}{\partial z^2}=0 \qquad (4.11)$$

Equations (4.10) and (4.11) result in

$$\left[\frac{\partial^2}{\partial r^2}+\frac{1}{r}\frac{\partial}{dr}+\frac{1}{r^2}\frac{\partial^2}{\partial \theta^2}+\frac{\partial^2}{\partial z^2}-\frac{\mu}{\rho}.\frac{\partial}{\partial t}\right]B_z=0 \qquad (4.12)$$

In A similar manner, by considering the r and θ components of equation (4.8) the equation (4.13) and (4.14) can be obtained [39]. Their derivation is shown in appendix A2 in detail.

$$\left[\frac{1}{r^2}.\frac{\partial^2}{\partial \theta^2}+\frac{\partial^2}{\partial z^2}+\frac{\partial^2}{\partial r^2}+\frac{1}{r}.\frac{\partial}{\partial r}-\frac{\mu}{\rho}.\frac{\partial}{\partial t}\right](rB_r)=-2.\frac{\partial B_z}{\partial z} \qquad (4.13)$$

$$\left[\frac{\partial}{\partial r}-r.\frac{\partial^2}{\partial z^2}-r.\frac{\partial^2}{\partial r^2}-\frac{1}{r}.\frac{\partial^2}{\partial \theta^2}+r.\frac{\mu}{\rho}.\frac{\partial}{dt}\right](rB_\theta)=2.\frac{\partial B_r}{\partial \theta} \qquad (4.14)$$

Now the solution for B_r , B_θ and B_z in any region can be found using equations (4.12) , (4.13) , (4.14) and (4.3). However, since we are interested in finding the no-load flux distribution within the air gap, equation (4.12) and ***Curl*** equation for the air gap region

can be used to solve for three components of the flux density reducing the number of computational steps needed.

4.2.1 Solution for No-load Flux Distribution Within the Air Gap

Solution for the air gap region can easily be obtained by substituting $\rho = \infty$ in equation (4.12). Then equation (4.12) becomes

$$\left[\frac{\partial^2}{\partial r^2}+\frac{1}{r}\frac{\partial}{\partial r}+\frac{1}{r^2}\frac{\partial^2}{\partial \theta^2}+\frac{\partial^2}{\partial z^2}\right](B_z)=0 \tag{4.15}$$

Equation (4.15) can be solved by using separation of variables [67][66]. Assume that the solution B_z is in the form of equation (4.16) [67][68].

$$B_z = Z(z).\,\Theta(\theta).\,R(r) \tag{4.16}$$

Substituting in equation (4.15) results in

$$\frac{1}{R}.\frac{d^2R}{dr^2}+\frac{1}{r}.\frac{1}{R}.\frac{dR}{dr}+\frac{1}{Z}.\frac{d^2Z}{dz^2}+\frac{1}{r^2}.\frac{1}{\Theta}.\frac{d^2\Theta}{d\theta^2}=0 \tag{4.17}$$

Let $$\frac{1}{Z}.\frac{d^2Z}{dz^2}=m^2 \tag{4.18}$$

and $$\frac{1}{\Theta}.\frac{d^2\Theta}{d\theta}=-p^2 \tag{4.19}$$

Then equation (4.17) yields, $$\frac{1}{R}.\frac{d^2R}{dr^2}+\frac{1}{r}.\frac{1}{R}.\frac{dR}{dr}+m^2-\frac{p^2}{r^2}=0 \tag{4.20}$$

Equations (4.18) to (4.20) can be solved to find the solutions for $Z(z)$, $\Theta(\theta)$, and $R(r)$ and hence B_θ [39] [67] [68]. Thus B_z is given by the equation (4.21)

$$B_z(r,q,z)=\sum_m\left\{\left(A_m.J_p(mr)+B_m.Y_p(mr)\right).\left(E_me^{mz}+F_me^{-mz}\right)\right\}\left(C_pSin(p\theta)+D_pCos(p\theta)\right)$$
$$+\left\{\left(G_p.r^p+H_p.r^{-p}\right).\left(C_p^1Sin(p\theta)+D_p^1Cos(p\theta)\right)\right\} \quad (4.21)$$

Since for any value of r and θ and $z=0$, B_z will always be equal to residual magnetism, B_{rs}. Therefore from equation (4.21) we can conclude that

$$G_p = H_p = 0 \quad (4.22)$$

Then

$$B_z(r,\theta,z)=\sum_m\left\{\left(A_m.J_p(mr)+B_m.Y_p(mr)\right).\left(E_me^{mz}+F_me^{-mz}\right)\right\}\left(C_pSin(p\theta)+D_pCos(p\theta)\right) \quad (4.23)$$

Now let us consider the physical placement of the rotor magnets which is shown in Fig. 4.1.

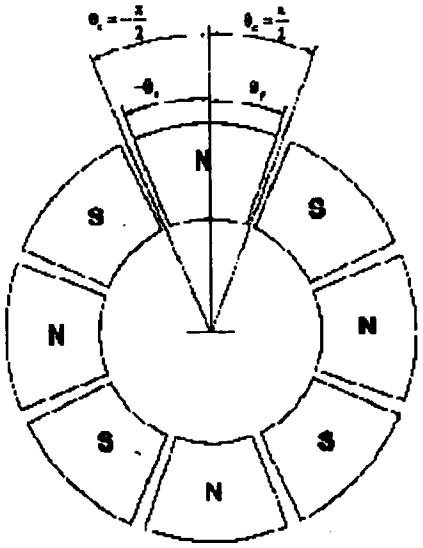


Fig. 4.1 Magnet configuration of an axial gap machine

This configuration of magnet placement leads to the following boundary conditions.

At any value of r, such that $R_i \le r \le R_o$ and any value of z such that $-m_t \le z \le l_g$ and $\theta_e = \pm\frac{\pi}{2}$, the B_r, B_θ and B_z components vanish. i.e.

$$B_r\left(r, z, \pm\tfrac{\pi}{2}\right) = 0 \tag{4.24}$$

$$B_\theta\left(r, z, \pm\tfrac{\pi}{2}\right) = 0 \tag{4.25}$$

$$B_z\left(r, z, \pm\tfrac{\pi}{2}\right) = 0 \tag{4.26}$$

Equation (4.23) and (4.24)-(4.26) implies that the value of C_p should be zero

$$C_p = 0 \tag{4.27}$$

Then equation (4.23) becomes

$$B_z(r,q,z) = \sum_m \left\{\left(A_m.J_p(mr) + B_m.Y_p(mr)\right).\left(E_m e^{mz} + F_m e^{-mz}\right)\right\}\left(D_p.Cos(p\theta)\right) \tag{4.28}$$

Because within the air gap region current density J is zero, the following equations hold true:

$$Curl(H) = Curl(B) = 0 \tag{4.29}$$

In cylindrical polar co-ordinates, equation (4.29) is equivalent to

$$\frac{1}{r}.\frac{\partial B_z}{\partial \theta} - \frac{\partial B_\theta}{\partial z} = 0 \tag{4.30}$$

$$\frac{\partial B_r}{\partial z} - \frac{\partial B_z}{\partial r} = 0 \tag{4.31}$$

$$\frac{B_\theta}{r} + \frac{\partial B_\theta}{\partial r} - \frac{1}{r}.\frac{\partial B_r}{\partial \theta} = 0 \tag{4.32}$$

Equation (4.28) and (4.30) can be used to solve for B_θ;

$$\frac{\partial B_\theta}{\partial z} = \frac{1}{r}.\frac{\partial}{\partial \theta}.\sum_m \left\{\left(A_m.J_p(mr)+B_m.Y_p(mr)\right).\left(E_m e^{mz}+F_m e^{-mz}\right)\right\}\left(D_p.Cos(p\theta)\right) \quad (4.33)$$

Equation (4.33) results in

$$\frac{\partial B_\theta}{\partial z} = \frac{p}{r}.\sum_m \left\{\left(A_m.J_p(mr)+B_m.Y_p(mr)\right).\left(E_m e^{mz}+F_m e^{-mz}\right)\right\}\left(-D_p.Sin(p\theta)\right) \quad (4.34)$$

$$B_\theta = \frac{p}{r}.\sum_m \frac{1}{m}\left\{\left(A_m.J_p(mr)+B_m.Y_p(mr)\right).\left(E_m e^{mz}-F_m e^{-mz}\right)\right\}\left(-D_p.Sin(p\theta)\right) \quad (4.35)$$

By substituting the value of B_z given by equation (4.28) in equation (4.32)

$$\frac{\partial B_r}{\partial z} = \frac{\partial}{\partial r}.\left\{\sum_m \left\{\left(A_m.J_p(mr)+B_m.Y_p(mr)\right).\left(E_m e^{mz}+F_m e^{-mz}\right)\right\}\left(D_p.Cos(p\theta)\right)\right\} \quad (4.36)$$

Now using the properties of derivatives of Bessel function [66][39]

$$\frac{d}{dr}J_p(mr) = \frac{p}{r}J_p(mr) - mJ_{p+1}(mr) \quad (4.37)$$

$$\frac{d}{dr}Y_p(mr) = \frac{p}{r}Y_p(mr) - mY_{p+1}(mr) \quad (4.38)$$

Then,

$$\frac{\partial B_r}{\partial z} = \sum_m \left\{\left[A_m\left(\frac{p}{r}J_p(mr)-mJ_{p+1}(mr)\right)+B_m\left(\frac{p}{r}Y_p(mr)-mY_{p+1}(mr)\right)\right].\left(D_p Cos(p\theta)\right)\left(E_m.e^{mz}+F_m.e^{-mz}\right)\right\} \quad (4.39)$$

$$B_r = \frac{p}{r}.\left\{\sum_m\left(\frac{A_m}{m}.J_p(mr)+\frac{B_m}{m}.Y_p(mr)\right).\left(E_m.e^{mz}-F_m.e^{-mz}\right).\left(D_p Cos(p\theta)\right)\right\} - \left\{\sum_m\left(A_m.J_{p+1}(mr)+B_m.Y_{p+1}(mr)\right).\left(E_m.e^{mz}-F_m.e^{-mz}\right).\left(D_p Cos(p\theta)\right)\right\} \quad (4.40)$$

The boundary condition on the magnet surface (i.e. at z=0) forces B_r and B_θ to be zero on the magnet surface. This implies:

$$B_r(r,\theta,0) = B_\theta(r,\theta,0) = 0 \tag{4.41}$$

Equation (4.35) , (4.40) and (4.41) results in

$$E_m = F_m \tag{4.42}$$

Now A_m , B_m , E_m , F_m in equation (4.40) can be lumped together and simplified.

Therefore, the final general solution for B_r , B_θ and B_z for a machine with p number of pole pairs are given by

$$B_r(r,\theta,z) = A.\frac{p}{r}\left\{\sum_m \left(A_m'.J_p(mr) + B_m^1.Y_p(mr)\right)\left(e^{mz} - e^{-mz}\right)\right\}\left(Cos(p\theta)\right)$$

$$-A.\left\{\sum_m \left(A_m.J_{p+1}(mr) + B_m.Y_{p+1}(mr)\right)\left(e^{mz} - e^{-mz}\right)\right\}\left(Cos(p\theta)\right) \tag{4.43}$$

$$B_\theta(r,\theta,z) = A.\frac{p}{r}\left\{\sum_m \left(A_m.J_p(mr) + B_m.Y_p(mr)\right)\left(e^{mz} - e^{-mz}\right)\right\}\left(-Sin(p\theta)\right) \tag{4.44}$$

$$B_z(r,\theta,z) = A\left\{\sum_m \left(A_m.J_p(mr) + B_m.Y_p(mr)\right)\left(e^{mz} + e^{-mz}\right)\right\}\left(Cos(p\theta)\right) \tag{4.45}$$

where m = Real positive constant and non zero

A = Constant

A_m = Lumped constant which is a function of m

B_m = Lumped constant which is a function of m

$$A_m' = \frac{A_m}{m}$$

$$B_m' = \frac{B_m}{m}$$

$R_i \le r \le R_o$; R_i = Inner radius, R_o= Outer radius

$J_p(mr)$ = Bessel's function of order p, argument mr

$Y_p(mr)$ = Weber's function of order p, argument mr

4.2.2 Application of the Boundary Conditions to Find Constants

The specific boundary conditions of the given problem can now be used to obtain the corresponding values of "m" and other constants and hence the numerical values of the magnetic flux densities given by equations (4.43) -(4.45).

Let

$$U_p(mr) = A_m.J_p(mr) + B_m.Y_p(mr) \tag{4.46}$$

Then $$B_\theta(r,\theta,z) = A.\frac{p}{r}\left\{\sum_m \left(U_p(mr)\right)\left(e^{mz} - e^{-mz}\right)\right\}\left(-Sin(p\theta)\right) \tag{4.47}$$

Now we know at $r=R_i$ and at $r=R_o$

$$B_\theta(R_i,\theta,z) = B_\theta(R_o,\theta,z) = 0 \tag{4.48}$$

But if we can write [67] [68]

$$U_p(mr) = Y_p(mR_i).J_p(mr) - J_p(mR_i).Y_p(mr) \tag{4.49}$$

By comparison of equation (4.46) and (4.49) we can deduct that

$$A_m = Y_p(mR_i) \tag{4.50}$$

$$B_m = -J_p(mR_i) \tag{4.51}$$

and it is always true that

$$U_p(mR_i) = 0 \tag{4.52}$$

This means $r=R_i$ is a root for the equation

$$U_p(mr) = Y_p(mR_i).J_p(mr) - J_p(mR_i).Y_p(mr) = 0 \tag{4.53}$$

for any $m \neq 0$ and $m=$ any real value. It is also required that the boundary condition at the outer radius to be satisfied. i.e.

$$B_\theta(R_o,\theta,z) = 0 \tag{4.54}$$

This implies that when $r = R_o$

$$U_p(mr) = 0 \tag{4.55}$$

i.e. $$U_p(mR_o) = Y_p(mR_o).J_p(mR_i) - J_p(mR_o).Y_p(mR_i) = 0 \tag{4.56}$$

Equation (4.56) is satisfied by m values which are the only roots of this equation. The plot of the $F(m) = U_p(mR_o)$ for p=6 as m varies is shown in fig. 4.2. The zero crossing points of fig. 4.2 give the corresponding values of m (m_i 's) . Thus, for any given value of number of pole pairs, p, corresponding values of m_i's can be found by obtaining the roots of equation (4.56). Those m values satisfy both the given boundary conditions and therefore they can be used to evaluate the value of $B_\theta(r,\theta,z)$ as shown by equation (4.57). The value of the constant "A" can also be found using the boundary condition at the magnet surface. This will be discussed during the solution procedure for $B_z(r,\theta,z)$. The number of roots , N, to be considered depends on the accuracy of the results that we want to calculate.

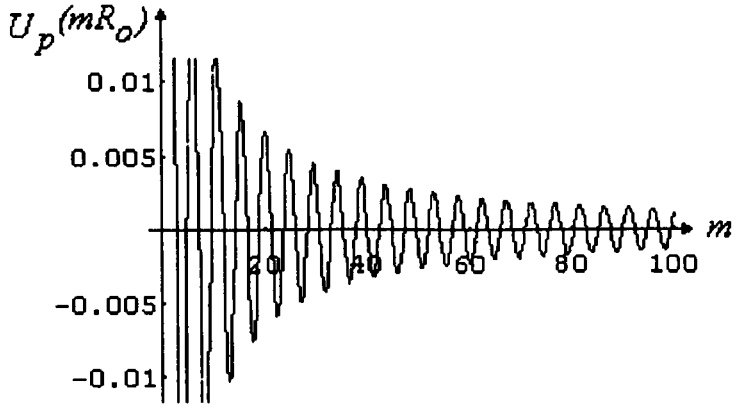


Fig. 4.2 The plot of $U_p\left(mR_o\right) = Y_p\left(mR_O\right).J_p(mR_i) - J_p(mR_O).Y_p(mR_i)$ for p=6, R_i =4.17 and R_o =5.50 for m=0$^+$ to 100.

$$B_\theta(r,\theta,z) = A.\frac{p}{r}\left\{\sum_{i=1}^{N} U_p(m_i r).\left(e^{m_i z} - e^{-m_i z}\right)\right\}\left(-Sin(p\theta)\right) \tag{4.57}$$

where

$$U_p(m_i r) = A_{m_i}.J_p(m_i r) + B_{m_i}.Y_p(m_i r) \tag{4.58}$$

$$A_{m_i} = Y_p(m_i R_i) \tag{4.59}$$

$$B_{m_i} = -J_p(m_i R_i) \tag{4.60}$$

Then the equation for $B_z(r,\theta,z)$ is given by

$$B_z(r,\theta,z) = A.\left\{\sum_{i=1}^{N} U_p(m_i r).\left(e^{m_i z} + e^{-m_i z}\right)\right\}\left(Cos(p\theta)\right) \tag{4.61}$$

Now by using the boundary condition for $B_z(r,\theta,z)$ at z=0 and $\theta = 0$

$$B_z(r,0,0) = B_R \tag{4.62}$$

where B_R = Residual magnetism of the magnetic material

By using equations (4.61) and (4.62) , the value of constant "A" can be found.

Equation for $B_r(r,\theta,z)$ is given by

$$B_r(r,\theta,z) = A.\frac{p}{r}\left\{\sum_{i=1}^{N}\left(U_p'(m_i r)\right).\left(e^{m_i z} - e^{-m_i z}\right)\right\}\left(Cos(p\theta)\right)$$

$$-\left\{\sum_{i=1}^{N} U_{p+1}(m_i r).\left(e^{m_i z} - e^{-m_i z}\right)\right\}\left(Cos(p\theta)\right) \qquad (4.63)$$

where

$$U_p'(m_i r) = \frac{Y_p(m_i R_i)}{m_i}.J_p(m_i r) - \frac{J_p(m_i R_i)}{m_i}.Y_p(m_i r) \qquad (4.64)$$

$$U_{p+1}(m_i r) = Y_p(m_i R_i).J_{p+1}(m_i r) - J_p(m_i R_i).Y_{p+1}(m_i r) \qquad (4.65)$$

Equations (4.57), (4.61) and (4.63) give the final solution of the three flux density components, $B_r(r,\theta,z)$, $B_\theta(r,\theta,z)$, and $B_z(r,\theta,z)$ within the air gap of the machine. Appendix A3 shows the detail calculation of three flux components for a machine with R_i=4.17 inch, R_o = 5.50 inch and p=6. Table 4.1- Table 4.3 show the peak magnitude of the flux densities calculated at r = 4.502 inch, r = 4.835 inch and r =5.167 inch as z value is varied from zero to actual air gap length. The slot effect is taken into consideration by extending the actual air gap to the effective air gap length according to equation (2.16) by multiplying with the Carter's coefficient [48].

Table 4.1 Peak Flux density in the Z-direction at different radial values.

Act. air gap (mils)	Eff. air gap (mils)	Eff. air gap (m)	B_z (Tesla)		
			r=4.502	r=4.835	r=5.167
0	0.0	0.000132	1.216	1.216	1.216
5	5.2	0.00000	1.215	1.198	1.195
10	10.4	0.000264	1.212	1.182	1.176
15	15.6	0.000396	1.208	1.169	1.158
20	20.8	0.000528	1.199	1.156	1.141
25	26.0	0.000660	1.190	1.144	1.124
30	31.2	0.000772	1.180	1.132	1.108
35	36.4	0.000924	1.169	1.120	1.091
38.5	**40.05**	**0.001017**	**1.165**	**1.111**	**1.084**
40	41.6	0.001050	1.159	1.109	1.075
45	46.8	0.001180	1.149	1.097	1.058
50	52.0	0.001320	1.138	1.086	1.042
55	57.2	0.001450	1.128	1.075	1.026
60	62.4	0.001580	1.118	1.063	1.010
65	67.6	0.001710	1.108	1.052	0.995
70	72.8	0.001840	1.098	1.041	0.979
75	78.0	0.001980	1.088	1.030	0.964
77	80.1	0.002030	1.082	1.024	0.955

Table 4.2 Peak flux density in r-direction at different radial values.

Act. air gap (mils)	**Eff. air gap (mils)**	**Eff. air gap (m)**	**B_r (Tesla)**		
			r=4.502	**r=4.835**	**r=5.167**
0	0.0	0.000000	0	0	0
5	5.2	0.000132	$4.994*10^{-4}$	$4.451*10^{-4}$	$3.705*10^{-4}$
10	10.4	0.000264	$9.988*10^{-4}$	$8.903*10^{-4}$	$7.409*10^{-4}$
15	15.6	0.000396	0.001	0.001	0.001
20	20.8	0.000528	0.002	0.02	0.001
25	26.0	0.000660	0.002	0.002	0.002
30	31.2	0.000772	0.003	0.003	0.002
35	36.4	0.000924	0.003	0.003	0.003
38.50	**40.05**	**0.001017**	**0.004**	**0.003**	**0.003**
40	41.6	0.001050	0.004	0.004	0.003
45	46.8	0.001180	0.004	0.004	0.003
50	52.0	0.001320	0.005	0.004	0.004
55	57.2	0.001450	0.005	0.005	0.004
60	62.4	0.001580	0.006	0.005	0.004
65	67.6	0.001710	0.006	0.005	0.005
70	72.8	0.001840	0.007	0.006	0.005
75	78.0	0.001980	0.007	0.006	0.006
77	80.1	0.002030	0.008	0.007	0.006

Table 4.3 Peak flux density in θ-direction at different radial values.

Act. air gap (mils)	Eff. air gap (mils)	Eff. air gap (m)	B_θ (Tesla)		
			r=4.502	r=4.835	r=5.167
0	0.0	0.000000	0	0	0
5	5.2	0.000132	0.001	0.001	$4.198*10^{-4}$
10	10.4	0.000264	0.003	0.003	$8.398*10^{-4}$
15	15.6	0.000396	0.005	0.004	0.001
20	20.8	0.000528	0.006	0.005	0.002
25	26.0	0.000660	0.07	0.007	0.002
30	31.2	0.000772	0.008	0.008	0.002
35	36.4	0.000924	0.011	0.009	0.003
38.5	**40.05**	**0.001017**	**0.012**	**0.009**	**0.003**
40	41.6	0.001050	0.012	0.010	0.003
45	46.8	0.001180	0.013	0.012	0.004
50	52.0	0.001320	0.015	0.013	0.004
55	57.2	0.001450	0.015	0.014	0.005
60	62.4	0.001580	0.018	0.016	0.005
65	67.6	0.001710	0.021	0.017	0.006
70	72.8	0.001840	0.021	0.018	0.006
77	80.1	0.002030	0.023	0.020	0.007

Table 4.4 shows the variation B_r ,B_z and B_θ along the center of the magnet face, at r=4.835, as θ_p varies from -90^0 to +90^0 electrical degrees. In these calculations magnet to magnet leakage is neglected. It is also assumed that the field in between two magnets is caused only by the magnets adjacent to the space. Fig. 4.3 shows the variation of B_z component as θ_p varies from -90^0 to +90^0 electrical degrees for r = 4.502 inch, r = 4.835 inch and r =5.167 inch. Fig. 4.4 and Fig. 4.5 show the variation of B_r and B_θ for the same radial values. The resultant flux density is given in the column 5 of Table 4.4. The plot of the resultant flux density variation is almost similar to B_z. Fig. 4.6 shows the measured value of the resultant magnetic flux density along the center of the magnet face for a 12-pole axial gap permanent magnet machine (This is measured by General Motors, Delco Remy Division in their laboratory at Indianapolis).

Table 4.4 The variation of B_r, B_z and B_θ along the center of the magnet face, at r=4.835, as θ_p varies from -90^0 to $+90^0$

Angle from magnet Center θ_p	B_z	B_r	B_θ	$B_R=(B_z^2+B_r^2+B_\theta^2)^{1/2}$
-90	0	0	0	0
-86	0.250	0.00021	0.00015	0.250
-82	0.500	0.00041	0.00258	0.500
-78	0.747	0.00062	0.00458	0.747
-74	0.990	0.00083	0.00654	0.990
-72	1.111	0.00093	0.00856	1.111
-64	1.111	0.00131	0.00808	1.111
-40	1.111	0.00229	0.00578	1.111
-16	1.111	0.00288	0.00248	1.111
-8	1.111	0.00290	0.00125	1.111
0	1.111	0.00300	0	1.111
8	1.111	0.00290	0.00125	1.111
16	1.111	0.00288	0.00248	1.111
40	1.111	0.00229	0.00578	1.111
64	1.111	0.00131	0.00808	1.111
72	1.111	0.00093	0.00856	1.111
74	0.990	0.00083	0.00654	0.990
78	0.747	0.00062	0.00458	0.747
82	0.500	0.00041	0.00258	0.500
86	0.250	0.00021	0.00015	0.250
90	0	0	0	0

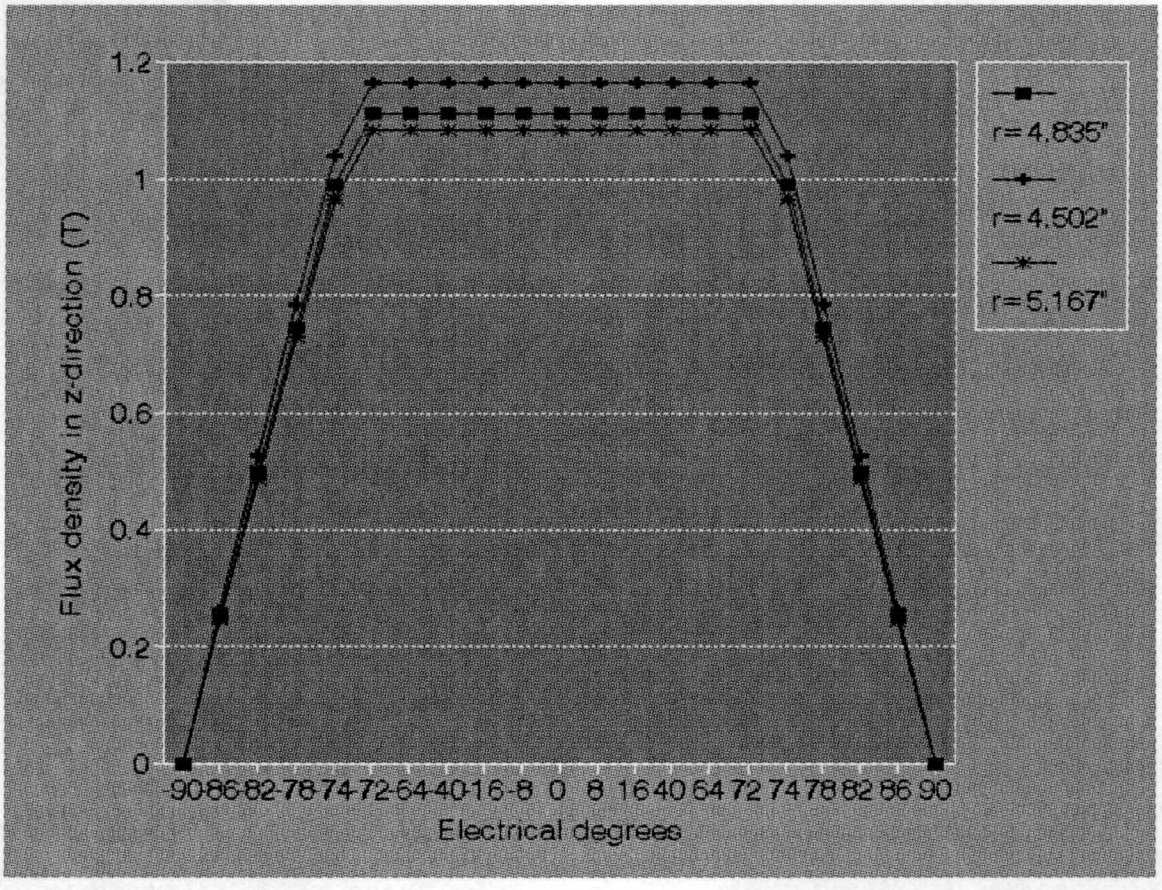


Fig. 4.3 Variation of z-direction flux density, B_z , along the center of magnet face.

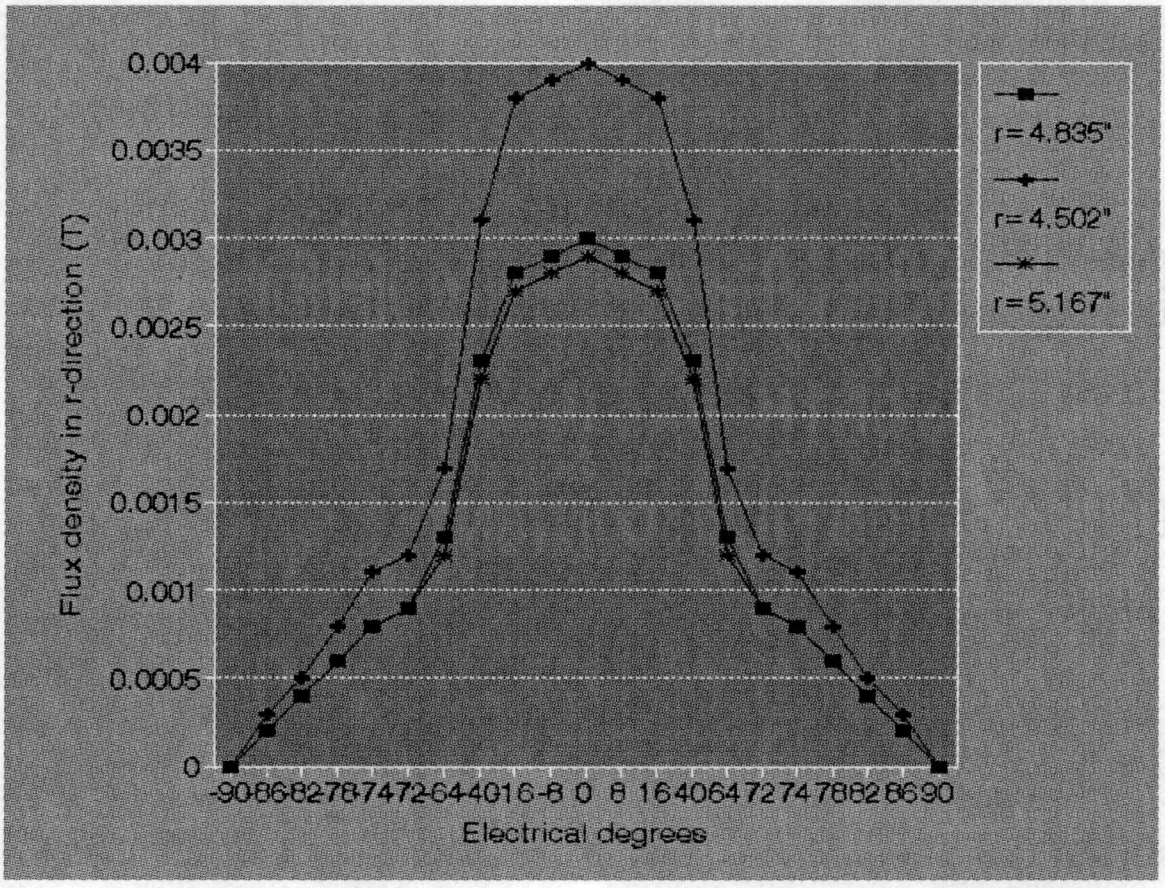


Fig. 4.4 Variation of radial flux density, B_r, along the center of magnet face.

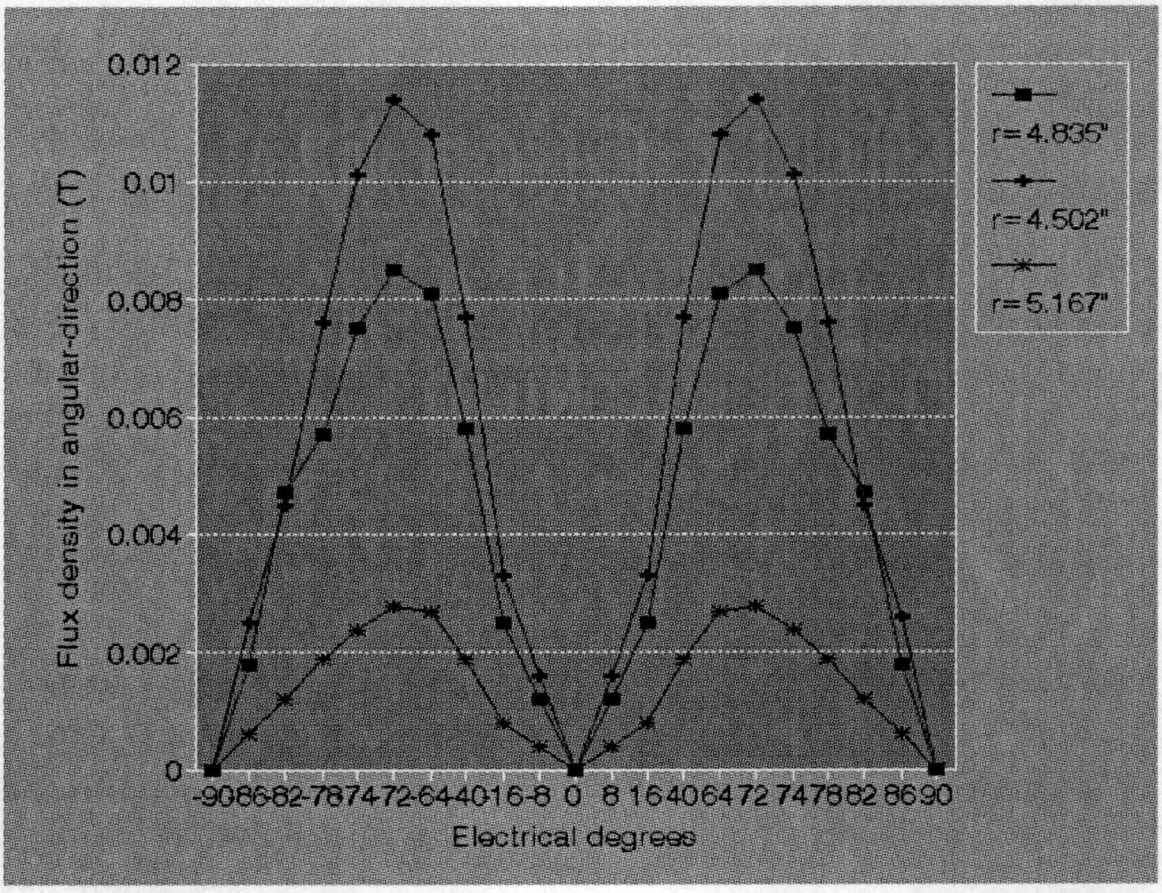


Fig. 4.5 Variation of angular flux density, B_θ, along the center of magnet face.

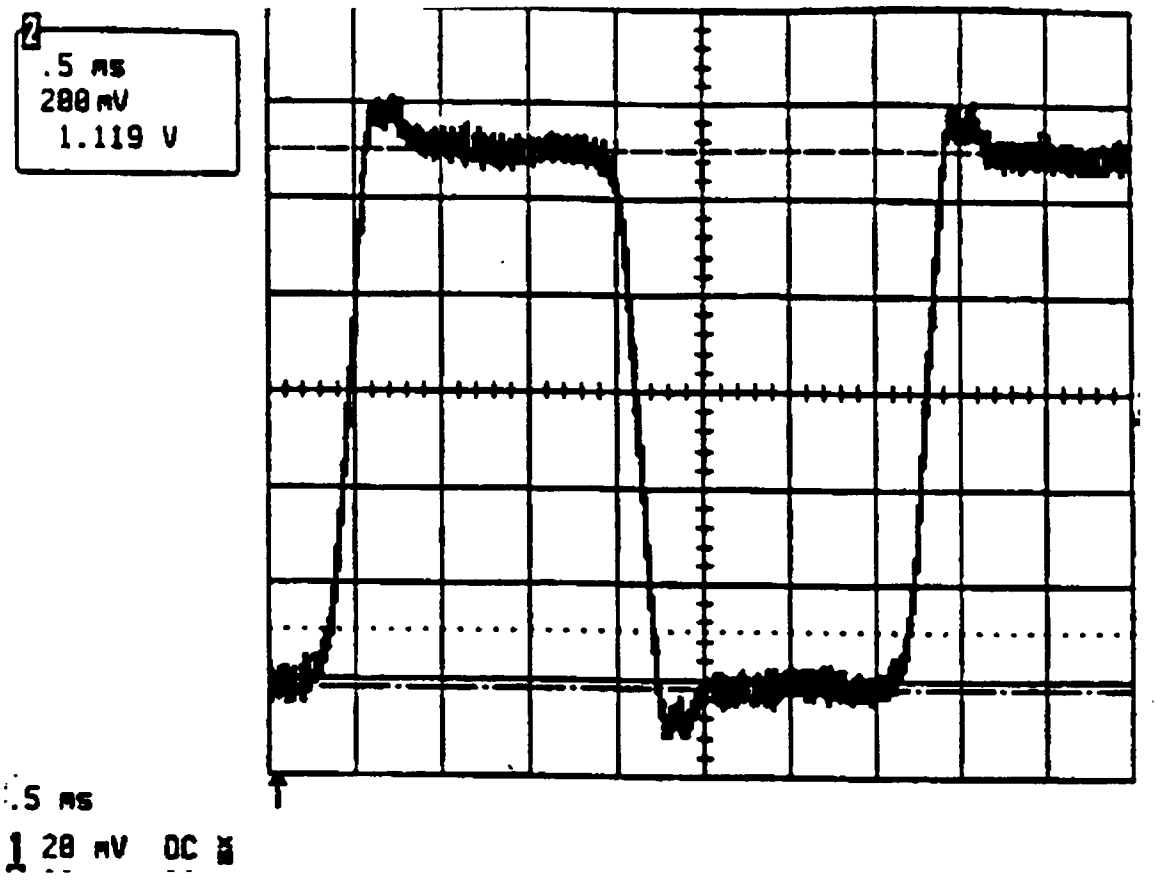


Fig. 4.6 Measured resultant flux density along the center of magnet.

CHAPTER 5

ESTIMATION OF ROTOR POSITION AND SPEED WITH AN ON-LINE PARAMETER IDENTIFICATION SCHEME FOR PMSM DRIVES

5.1 Introduction

Permanent magnet synchronous machines with sinusoidally distributed windings use shaft mounted encoders to obtain the absolute rotor position information required for inverter firing in order to maintain the synchronism, which is an essential requirement in a drive control. This kind of configuration greatly reduces the system robustness and reliability. For improving the mechanical robustness and reliability a few schemes have been suggested [57], [59], [60], [61], [62]. One of the techniques that has been used in the past is the back emf method. In this approach, the difficulty in estimating the counter emf at low speeds makes it unsuitable at low speeds. An observer technique has been attempted in [60], considering the machine model in the synchronously rotating reference frame. Both the observer and observer error dynamics are highly non-linear and require gain scheduling at different operating conditions for stability. Recently, a few methods have been proposed [61], by computing stator inductances. In this approach, calculation of inductances may lead to errors due to subtransient effects [64]. In [62], an algorithm was developed from rotating frame d-q equivalent frame. However, the initial position is not identified, and it does not consider any parameter variation effects. Also in [57], parameter variation effect is not considered. In this work, the parameter variation effect due to saturation and temperature is included in the estimation algorithm. The machine d-q

equivalent model is more accurately represented by taking the core losses into consideration. The estimation algorithm is developed in the synchronously rotating reference frame for effective use in machine vector control. Furthermore, the inclusion of parameter variation can enhance the prediction of machine performance. A simple hardware implementation to estimate the initial rotor position during the machine start-up and the implementation of the position and speed estimation algorithm using a Texas Instruments Digital Signal Processor (TMS320C25 DSP) is presented. A complete vector-controlled drive system using an actively clamped resonant dc link inverter with the estimation algorithm is simulated using PC based SIMNON to verify the validity of the algorithm.

5.2 Development of an accurate d^e-q^e circuit model

Fig. 5.1 shows the equivalent per-phase diagram of the machine with core losses taken into consideration in the form of a parallel resistor R_c, which is placed across the machine internal voltage E_i. Fig. 5.2 shows the equivalent phasor diagrams in the d-q frame with core loss resistor accounted. Using Fig. 5.1, equations for I_d and I_q can be obtained as follows.

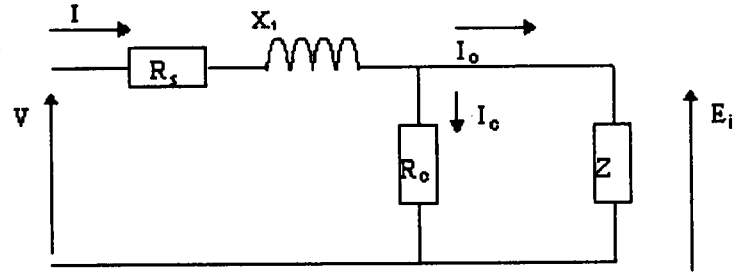


Fig. 5.1 Equivalent per phase diagram with core loss resistor, R_c.

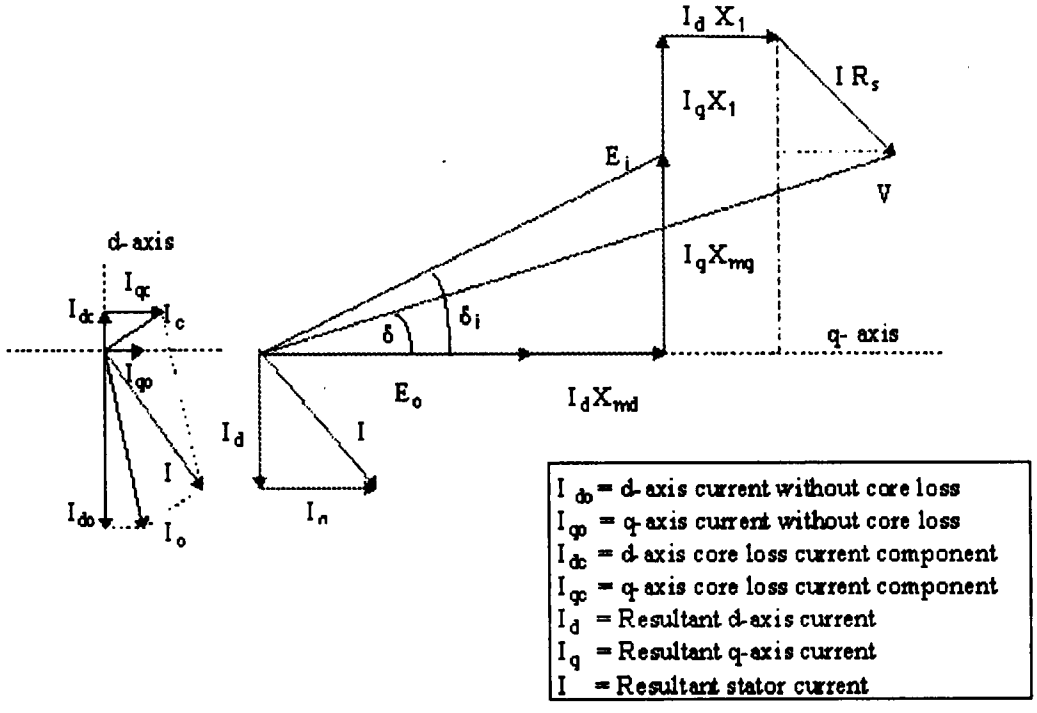


Fig. 5.2 Equivalent phasor diagram in d^e-q^e reference frame with core loss accounted.

$$I_d = I_{do} + I_{dc} \tag{5.1}$$

$$I_q = I_{qo} + I_{qc} \tag{5.2}$$

Fig. 5.2 gives

$$E_i \cos\delta_i = E_o + I_{do} X_{md} \tag{5.3}$$

$$E_i Sin\delta_i = I_q X_{mq} = I_{dc} R_c \tag{5.4}$$

where X_{md} and X_{mq} are d-axis and q-axis magnetizing inductances.

Equations (5.1) , (5.3) and (5.4) result in

$$I_d = \frac{E_i \cos\delta_i - E_0}{X_{md}} - \frac{E_i \sin\delta_i}{R_c} \tag{5.5}$$

and it follows from Fig. 5.1 that

$$I_{qc} = \frac{E_i Cos\delta_i}{R_c} \tag{5.6}$$

From equations (5.2), (5.4) and (5.6)

$$I_q = \frac{E_i \sin\delta_i}{X_{mq}} + \frac{E_i \cos\delta_i}{R_c} \tag{5.7}$$

From Fig. 5.2

$$V_d = V\sin\delta = E_i \sin\delta_i + I_q X_1 - I_d R_s \tag{5.8}$$

$$V_q = V\cos\delta = E_i \cos\delta_i + I_d X_1 + I_q R_s \tag{5.9}$$

From equations (5.5) and (5.9)

$$I_d = \frac{\left(V\cos\delta - I_d X_1 - I_q R_s - E_o\right)}{X_{md}} - \frac{\left(V\sin\delta - I_q X_1 + I_d R_s\right)}{R_c} \tag{5.10}$$

$$\frac{V\cos\delta}{X_{md}} - \frac{V\sin\delta}{R_c} = I_d + \frac{I_d X_1}{x_{md}} + \frac{I_d R_s}{R_c} + \frac{I_q R_s}{X_{md}} - \frac{I_q X_1}{R_c} + \frac{E_o}{X_{md}} \tag{5.11}$$

From equations (5.7), (5.8) and (5.9)

$$I_q = \frac{\left(V\sin\delta - I_q X_1 + I_d R_s\right)}{X_{md}} + \frac{\left(V\cos\delta - I_d X_1 - I_q R_s\right)}{R_c} \tag{5.12}$$

$$\frac{V\sin\delta}{X_{mq}} + \frac{V\cos\delta}{R} = I_q + \frac{I_d X_1}{R_c} - \frac{I_d R_s}{x_{mq}} + \frac{I_q X_1}{X_{mq}} + \frac{I_q R_s}{R_c} \tag{5.13}$$

By solving for V_d and V_q, using equations (5.11) and (5.13)

$$V_d = V\sin\delta = I_q\left(X_q - \varepsilon X_{mq}\right) - I_d\left(R_s + \varepsilon R_c\right) - E_o \frac{\varepsilon}{\alpha_d} \tag{5.14}$$

Equation (5.14) can be rewritten as in equation (5.17), by Substituting for X_q and X_{mq} from equations (5.15) and (5.16),

$$X_q = L_q.\omega_e \tag{5.15}$$

$$X_{mq} = L_{mq}\omega_e \tag{5.16}$$

$$V_d = V\sin\delta = I_q\varpi_e\left(L_q - \varepsilon L_{mq}\right) - I_d\left(R_s + \varepsilon R_c\right) - E_o\frac{\varepsilon}{\alpha_d} \tag{5.17}$$

where $$\varepsilon = \frac{X_{md}X_{mq}}{\left(R_c^2 + X_{md}X_{mq}\right)} \tag{5.18}$$

$$\alpha_d = \frac{R_c}{X_{md}} \tag{5.19}$$

$$V_q = V\cos\delta = I_d\left(X_d - \varepsilon X_{md}\right) + I_q\left(R_s + \varepsilon R_c\right) + E_o(1-\varepsilon) \tag{5.20}$$

equation (5.20) can be rewritten as in equation (5.23) by substituting for X_d and X_{md} from equations (5.21) and (5.22).

$$X_d = L_d\omega_e \tag{5.21}$$

$$X_{md} = L_{md}\omega_e \tag{5.22}$$

$$V_q = V\cos\delta = I_d\omega_e\left(L_d - \varepsilon L_{md}\right) + I_q\left(R_s + \varepsilon R_c\right) + E_o(1-\varepsilon) \tag{5.23}$$

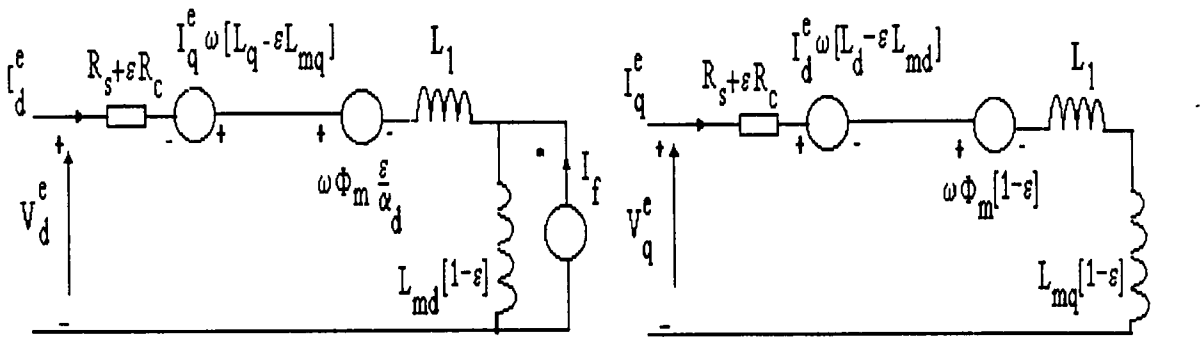
In order to account for the core loss effect, the d and q axes magnetizing inductances should be modified as shown in equations (5.24) and (5.25).

$$X_{mmd} = X_{md}(1-\varepsilon) \tag{5.24}$$

$$X_{mmq} = X_{mq}(1-\varepsilon) \tag{5.25}$$

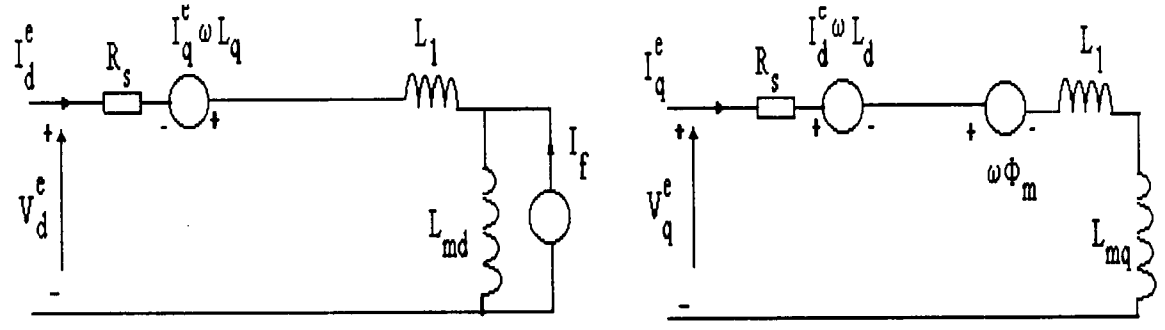
Now the equations (5.22) -(5.25) can be used to modify the d^e-q^e equivalent circuit of the machine, as shown in Fig. 5.3a and Fig. 5.3b. The d^e-q^e equivalent circuit for the

permanent magnet synchronous machine, when the core losses are neglected, is shown in fig 5.4a and Fig. 5.4b. It is clear that the modified circuits shown in Fig. 5.3 become the circuits shown in Fig. 5.4 when $\varepsilon = 0$ (i.e. core losses are neglected , R_c =0).



(a) (b)

Fig. 5.3 Modified d^e-q^e equivalent circuit of the machine.



(a) (b)

Fig. 5.4 d^e-q^e equivalent circuit when core losses are neglected.

5.3 A Method to Account for Machine Parameter Variations due to Saturation and Temperature

The variations of the machine magnetic parameters L_d , L_q , and permanent magnet flux f_m, due to the level of saturation, are defined as the functions of level of current loading in d^e and q^e axes [57]. They can be defined in the machine model by a simple linear relationship as shown in equations (5.26) to (5.30).

$$L_d = L_{do} - \beta_{d1} I_d \qquad \text{for} \quad I_d > 0 \qquad (5.26)$$

$$L_d = L_{do} - \beta_{d2} I_d \qquad \text{for} \quad I_d < 0 \qquad (5.27)$$

$$L_q = L_{qo} - \beta_{q1} I_q \qquad (5.28)$$

$$\phi_m = \phi \qquad \text{for} \quad I_q < I_{qo} \qquad (5.29)$$

$$\phi_m = \phi - K_\phi \left(I_q - I_{qo} \right) \qquad \text{for} \quad I_q > I_{qo} \qquad (5.30)$$

Magnet induced EMF, E_o , should also be modified according to the equations (5.29) and (5.30). Thus the modified induced EMF becomes:

$$E_0 = E_o^o \qquad \text{for} \quad I_q < I_{qe} \qquad (5.31)$$

$$E_o = E_o^o - K_\phi \left(I_q - I_{qo} \right) \qquad \text{for} \quad I_q > I_{qe} \qquad (5.32)$$

where ϕ is as defined in equation (5.34) and other constants are defined in Table 5.1. Because the rate of change of L_d with I_d is different for the normal mode of operation as compared to the field weakening mode of operation, two saturation coefficients are required to describe the variation of L_d. In general, for machines with saliency, b_{q1} and

b_{d2} are much higher than b_{d1}. For axial-gap machines, due to its planar air-gap and very high pole enclosure factor, saturation coefficients b_{d1} and b_{q1} are almost equal. These values vary to a great extent from machine to machine and according to the rotor configuration. However, the normal range of variation of L_d and L_q is about 20% -30% as the current is varied from zero to full load value and therefore, the saturation coefficient can be selected accordingly. In equation (5.30), I_{qo} is normally taken as a fraction of full load current, I_{qf}, and it varies from machine to machine. Finally, the variations of stator resistance and magnet flux due to temperature variations are modeled as shown in equations (5.33) and (5.34).

$$R_s = R_{so}\left[1+\rho(T_s - T_o)\right] \tag{5.33}$$

$$\phi = \phi_o\left[1+k_t(T_r - T_o)\right] \tag{5.34}$$

Where R_s = Stator resistance at measured stator temperature , T_s

T_o = Temperature at which stator resistance R_{so} and magnet flux ϕ_o is given

k_t = Temperature coefficient of magnet flux

ρ = Temperature coefficient of copper

T_s = Estimated rotor temperature using stator-rotor thermal model.

The measurement of the rotor magnet temperature is difficult; therefore, the rotor temperature is estimated using a simplified first-order thermal model, as shown in equation (5.35) [63].

Table 5.1 Machine ratings and parameters

Machine Parameter	**Value**	
Rated Power (P)	94	HP
Rated Speed (N_R)	2800	RPM
Rated Voltage (DC Link Voltage) (V_{L-L})	200	Volts
Rated Current (I)	208	Amps
Stator Resistance (R_{so}) @ $T_0 = 75^0$ C	0.0087	Ohms
Equivalent Core Loss Resistance (R_c)	101.66	Ohms
Stator Leakage Reactance (L_l)	0.0000277	H
d-axis Inductance (L_d)	0.000181	H
q-axis Inductance (L_q)	0.000185	H
d-axis Magnetizing Inductance (L_{md})	0.000090	H
q-axis Magnetizing Inductance (L_{qd})	0.000092	H
d-axis Saturation Coefficient (b_{d1})	0.26	mH/ A
d-axis Saturation Coefficient (b_{d2})	0.32	mH/ A
q-axis Saturation Coefficient (b_{q1})	0.26	mH/ A
Coeff. to Account for Pole Sat. (K_f)	2.40	mWeb/ A
I_{qo}	104	Amps
Temperature Coefficient of Mag. Flux (K_t)	-0.2%	per ^{0} C
Magnet Flux (f_0) @ $T_o = 75^\circ$ C	0.274	Web
Temperature Coefficient of Resistance (r)	0.00374	Ohms/ ^{0} C
Stator Rotor Thermal Time Constant (t_{rs})	40	min
Machine Moment of Inertia (J)	0.946	$Nm.s^2$

$$T_r(k) = T_r(k-1) + \frac{1}{\tau}\left[T_s(k-1) - T_r(k-1)\right] \tag{5.35}$$

Where t = Thermal time constant

$T_r(k)$,$T_r(k\text{-}1)$ = Estimated rotor temperature at k^{th} and $(k\text{-}1)^{th}$ sampling interval.

$T_s(k\text{-}1)$ = Measured stator temperature at $(k\text{-}1)^{th}$ sampling interval.

As seen from equations (11)- (18) these linear equations can easily be programmed within the DSP.

5.4 Algorithm Development for the Estimation of Rotor Position and Rotor Speed

5.4.1 Rotor Position Estimation

The modified d^e-q^e equivalent circuits shown in Fig. 5.3 can be used to develop a sensorless position and speed measuring scheme for the drive system. The estimation algorithm is developed in d^e-q^e reference frame, so that this can be used effectively in vector control drives. Fig. 5.5 shows the synchronous and stationary reference frames for the permanent magnet synchronous machine. The initial rotor position is assumed to be equal to θ_o and is shown in Fig. 5.5.

Three phase to stationary reference transformation results in equations (5.36)-(5.39)

$$V_d^s = -\frac{(V_b - V_c)}{\sqrt{3}} \tag{5.36}$$

$$V_q^s = V_a \tag{5.37}$$

$$I_d^s = -\frac{(I_b - I_c)}{\sqrt{3}} \tag{5.38}$$

$$I_q^s = I_a \tag{5.39}$$

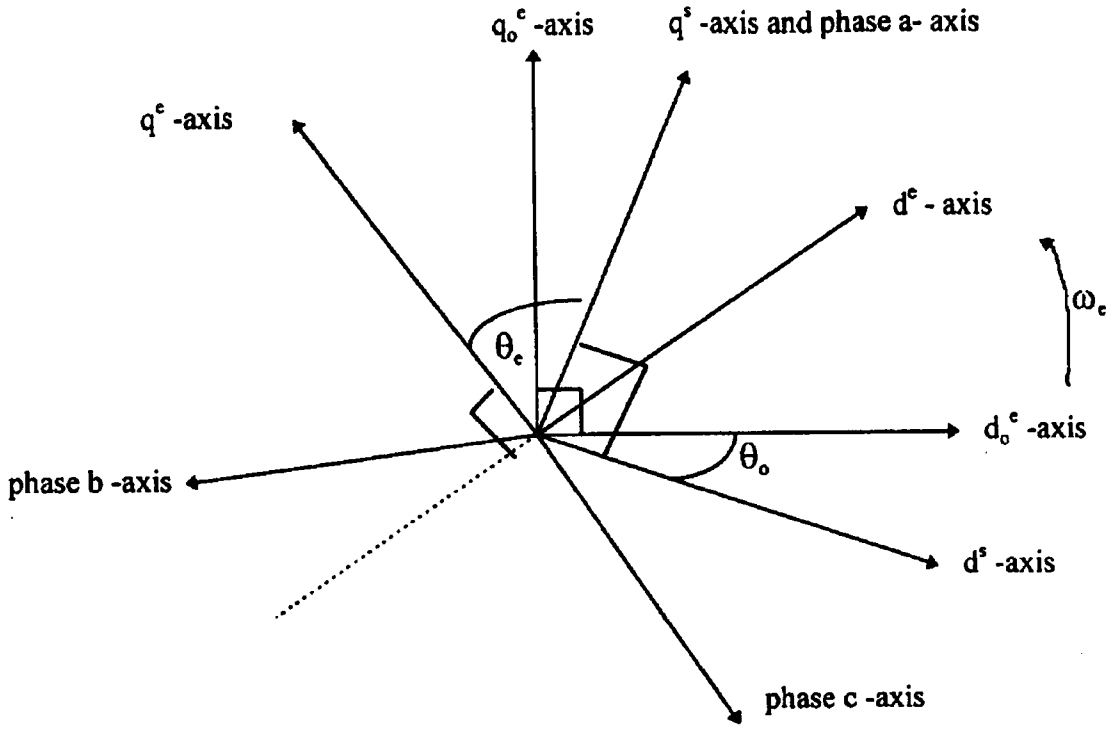


Fig. 5.5 d^e-q^e , d^s-q^s and a-b-c axes for the permanent magnet machine.

Transforming d^s-q^s voltages and currents into d^e-q^e reference frame ,

$$I_d^e = I_d^s \cos\theta_e + I_q^s \sin\theta_e \tag{5.40}$$

$$I_q^e = -I_d^s \sin\theta_e + I_q^s \cos\theta_e \tag{5.41}$$

$$V_d^e = V_d^s \cos\theta_e + V_q^s \sin\theta_e \tag{5.42}$$

$$V_q^e = -V_d^s \sin\theta_e + V_q^s \cos\theta_e \tag{5.43}$$

where $\theta_e = \omega_e t$ (5.44)

Fig. 5.3a , the modified d^e equivalent circuit, can be used to obtain an equation for the modified d^e axis voltage. This is given by equation (5.45).

$$V_d^e = \{(R_s + \varepsilon R_c) + p(L_d - \varepsilon L_{md})\} I_d^e - \omega_e I_q^e (L_q - \varepsilon L_{mq}) + \omega_e \phi_m \frac{\varepsilon}{\alpha_d} \tag{5.45}$$

where $p = \frac{d}{dt}$ and

$$L_d = L_1 + L_{md} \tag{5.46}$$

$$L_q = L_1 + L_{mq} \tag{5.47}$$

By substituting the values for I_d^e and I_q^e from equations (5.38) and (5.39) into equation (5.45) and combining with equation (5.40), an expression for the θ_e can be obtained as shown in equation (5.48).

$$Tan\theta_e = \frac{\{(R_s + \varepsilon R_c) I_d^s + [L_1 + L_{md}(1-\varepsilon)] p I_d^s - I_q^s \omega_e (L_q - \varepsilon L_{mq}) - V_d^s\}}{\{V_q^s - (R_s + \varepsilon R_c) I_q^s - [L_1 + L_{md}(1-\varepsilon)] p I_q^s - I_d^s \omega_e (L_q - \varepsilon L_{mq})\}} \tag{5.48}$$

Let $X = (R_s + \varepsilon R_c) I_d^s + [L_1 + L_{md}(1-\varepsilon)] p I_d^s - I_q^s \omega_e (L_q - \varepsilon L_{mq}) - V_d^s$ (5.49)

$$Y = V_q^s - (R_s + \varepsilon R_c) I_q^s - [L_1 + L_{md}(1-\varepsilon)] p I_q^s - I_d^s \omega_e (L_q - \varepsilon L_{mq}) \tag{5.50}$$

Then $Cos\theta_e = \frac{Y}{\sqrt{X^2 + Y^2}}$ (5.51)

$$Sin\theta_e = \frac{X}{\sqrt{X^2 + Y^2}} \tag{5.52}$$

and rotor position at the machine start-up, θ_{eo} ,can be obtained by substituting $\omega_e = 0$ in equation (5.48).

$$Tan\theta_{eo} = \frac{\{(R_s + \varepsilon R_c)I_d^s + [L_1 + L_{md}(1-\varepsilon)]pI_d^s - V_d^s\}}{\{V_q^s - (R_s + \varepsilon R_c)I_q^s - [L_1 + L_{md}(1-\varepsilon)]pI_q^s\}} \quad (5.53)$$

and $$X_o = (R_s + \varepsilon R_c)I_d^s + [L_1 + L_{md}(1-\varepsilon)]pI_d^s - V_d^s \quad (5.54)$$

$$Y_o = V_q^s - (R_s + \varepsilon R_c)I_q^s - [L_1 + L_{md}(1-\varepsilon)]pI_q^s \quad (5.55)$$

Then $$Cos\theta_{eo} = \frac{Y_o}{\sqrt{X_o^2 + Y_o^2}} \quad (5.56)$$

$$Sin\theta_{eo} = \frac{X_o}{\sqrt{X_o^2 + Y_o^2}} \quad (5.57)$$

To find the actual value of θ_{eo} , the polarity detection test as described in section 5.4.2 should be carried out. This test can be used to determine the polarity in the vicinity of phase "a". If the phase "a" is closer to a north pole, then the initial rotor position will be given by equation (5.51). Otherwise, it is given by equation (5.58).

$$\theta_{eo} \Rightarrow \theta_{eo} + \pi \quad (5.58)$$

5.4.2 Polarity Detection Test and Initial Rotor Position Estimation

A special inverter switching configuration is required to determine the polarity in the vicinity of phase "a" at the machine start-up. This test configuration takes the advantage of the non-linearity of the magnetization characteristics. Fig. 5.6 shows a typical curve of the magnetization characteristics. At the machine start-up, the phase windings should be connected as shown in Fig. 5.7 for a very short time, through the inverter switches. During this period of time the positive and negative bus voltage is applied to phase "a" and the rate of change of current in phase "a" in two different

instances is compared. This comparison can be used to determine the polarity in the vicinity of phase "a" . Assume that phase "a" is closer to a north pole. Application of a positive voltage to phase "a" aids the magnetization and therefore the rate of rise of phase "a" current would be higher than that would have resulted if the voltage was negative. If phase "a" is closer to a south pole, then the application of the negative voltage would have resulted in a higher rate of change of current in phase "a' than it would have been if the voltage was positive. Fig. 5.8 shows the two possibilities and the initial value of the rotor position depending upon the results of the comparison.

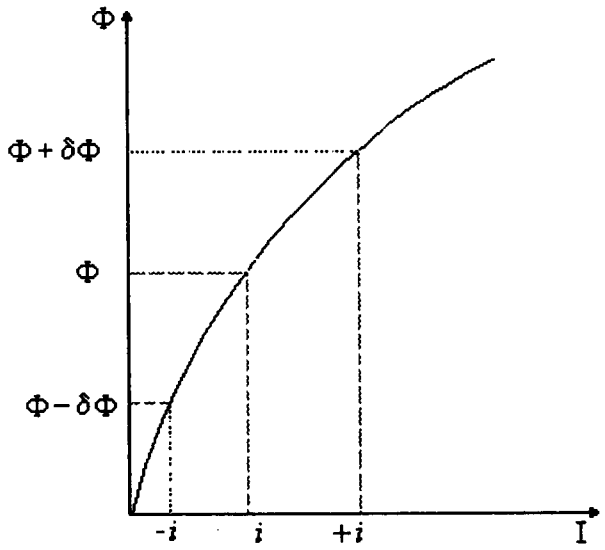


Fig. 5.6 Typical magnetization characteristics curve.

In order to obtain the phase winding configuration and voltage pulse application shown in Fig. 5.7 , it is necessary to switch on the inverter switches Q_1 , Q_2 and Q_6 during

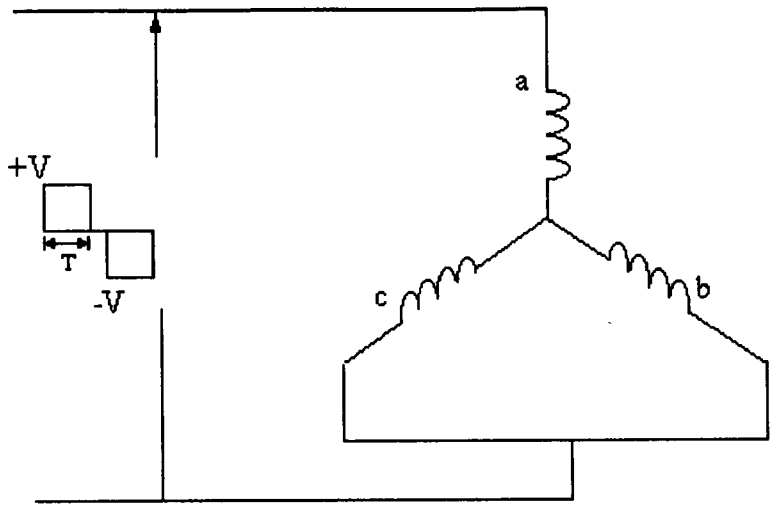


Fig. 5.7 Phase winding connection configuration at the machine start-up.

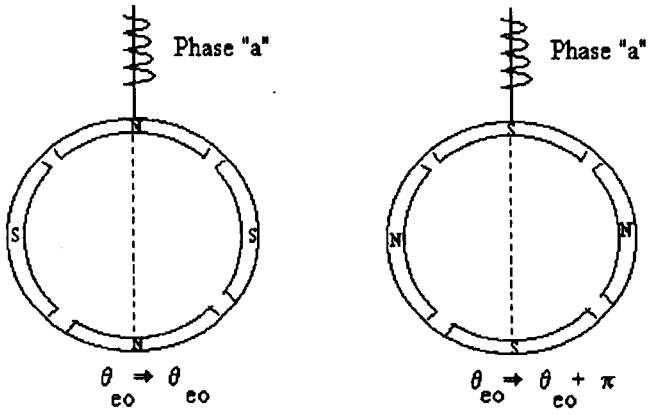


Fig. 5.8 Two possibilities of the initial rotor position.

the application of the positive voltage and the inverter switches Q_3 , Q_4 and Q_5 during the application of the negative voltage. Once the polarity detection test is completed, it is necessary to estimate the value of initial rotor position, θ_{eo} . This requires a special switching configuration of the inverter during the start-up process. Fig. 5.9 shows the inverter control block diagram with the modified inverter switching pattern to facilitate for the required configuration at the machine start-up. This configuration uses 10 single pole double throw (SPDT) analog switches. The functional block diagram with logic "1" as input to the switches is shown with the truth table in Fig. 5.10. By controlling the four digital to analog (D/A) channel logic levels as shown in Table 5.2, the inverter mode of operation can be progressively changed from polarity detection state to initial rotor position estimate state. Once this stage is reached, a high frequency saw tooth waveform control signal, I_q^{e*}, as shown in Fig. 5.9, is applied to the torque control loop. This will cause the motor shaft to oscillate without rotating. At the same time D/A channels # 3 and # 4 are set to 1 and 0 respectively. This process enables the estimation of the initial rotor position according to equation (5.53). Finally, the inverter configuration is transferred to the normal operating mode of the drive system, as shown in Fig. 5.11.

Table 5.2 Control logic signals at the machine start-up

Control Signal Channel #			
DA1	**DA2**	**DA3**	**DA4**
1	0	0	0
1	1	0	0
1	1	1	0
1	1	0	0
1	1	0	1
0	1	0	0
1	0	0	0
0	0	1 (initial position est.)	0 (initial position est.)
0	0	sin q_e (normal mode)	cos q_e (normal mode)

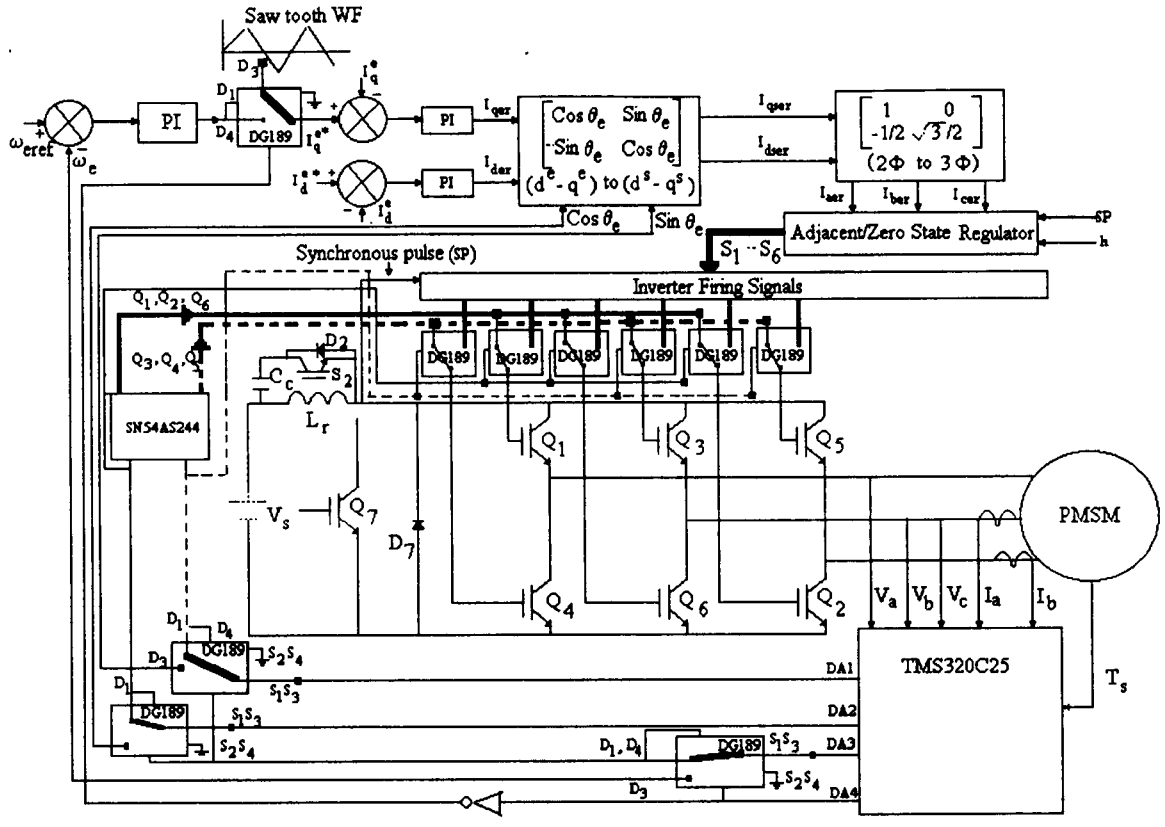
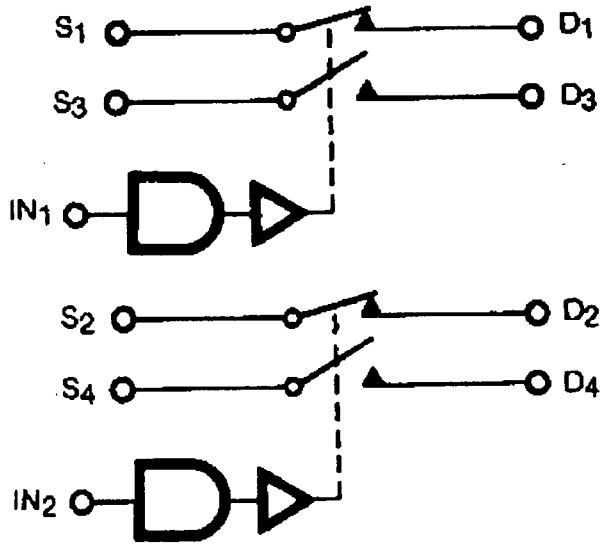


Fig. 5.9 Inverter control block diagram and switching configuration for initial rotor position estimation



Truth Table

LOGIC	SW 1 SW 2	SW 3 SW 4
0	OFF	ON
1	ON	OFF

Fig. 5.10 The functional block diagram of SPDT switch.

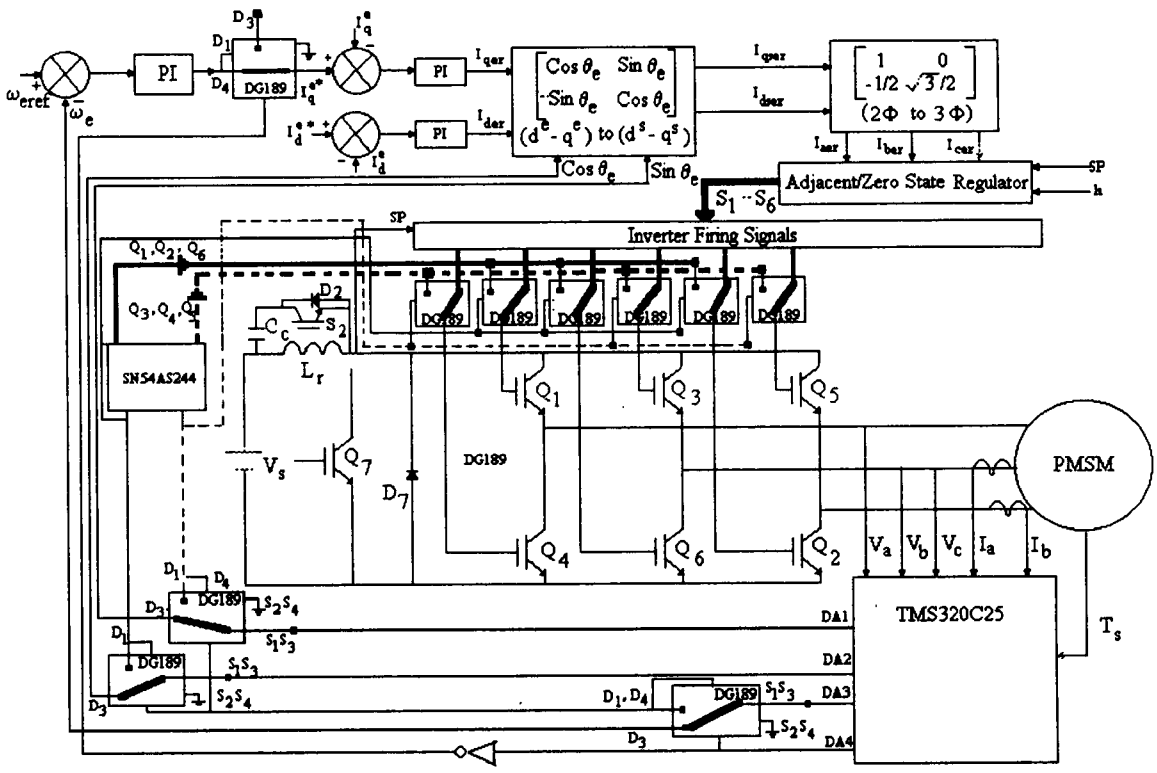


Fig. 5.11 Inverter control block diagram and switching configuration for normal mode of operation of the drive system.

5.4.3 Rotor Speed Estimation

The modified q^e equivalent circuit shown in Fig. 5.3b can be used to obtain an expression for the V_q^e as given by equation (5.59).

$$V_q^e = \left[(R_s + \varepsilon R_c) + p(L_q - \varepsilon L_{mq})\right] I_q^e + I_d^e \omega_e (L_d - \varepsilon L_{md}) + \omega_e \phi_m (1-\varepsilon) \tag{5.59}$$

By substituting for I_d^e , I_q^e and V_q^e from equations (5.40), (5.41) and (5.43)

$$Cos\theta_e \left\{V_q^s - \left[(R_s + \varepsilon R_c) + (L_q - \varepsilon L_{mq})p\right] I_q^s - \omega_e (L_d - \varepsilon L_{md}) I_d^s\right\}$$

$$= Sin\theta_e \left\{V_d^s - \left[(R_s + \varepsilon R_c) + (L_q - \varepsilon L_{mq})p\right] I_d^s + \omega_e (L_d - \varepsilon L_{md}) I_q^s\right\} + \omega_e \phi_m (1-\varepsilon) \tag{5.60}$$

Dividing by $Cos\theta_e$ and substituting for $Tan\theta_e$ and $Cos\theta_e$ result in equation (5.61).

$$\left\{V_q^s - \left[(R_s+\varepsilon R_c) + (L_q - \varepsilon L_{mq})p\right] I_q^s - \omega_e (L_d - \varepsilon L_{md}) I_d^s\right\} =$$

$$\frac{\left\{\left[(R_s+\varepsilon R_c) + (L_d - \varepsilon L_{md})p\right] I_d^s - I_q^s \omega_e (L_q - \varepsilon L_{mq}) - V_d^s\right\}}{\left\{V_q^s - (R_s+\varepsilon R_c) I_q^s - \left[L_d - \varepsilon L_{md}\right] p I_q^s - I_d^s \omega_e (L_q - \varepsilon L_{mq})\right\}} \left\{V_d^s - \left[(R_s+\varepsilon R_c) + (L_q - \varepsilon L_{mq})p\right] I_d^s + \omega_e (L_d - \varepsilon L_{md}) I_q^s\right\} +$$

$$\frac{\left\{\left[\left[(R_s+\varepsilon R_c) + (L_d - \varepsilon L_{md})p\right] I_d^s - I_q^s \omega_e (L_q - \varepsilon L_{mq}) - V_d^s\right]^2 + \left[V_q^s - (R_s+\varepsilon R_c) I_q^s - \left[L_d - \varepsilon L_{md}\right] p I_q^s - I_d^s \omega_e (L_q - \varepsilon L_{mq})\right]^2\right\}^{\frac{1}{2}}}{V_q^s - (R_s+\varepsilon R_c) I_q^s - \left[L_d - \varepsilon L_{md}\right] p I_q^s - I_d^s \omega_e (L_q - \varepsilon L_{mq})} \omega_e (1-\varepsilon)$$

(5.61)

Let

$$A = V_q^s - \left[(R_s + \varepsilon R_c) + (L_q - \varepsilon L_{mq})p\right] I_q^s \tag{5.62}$$

$$B = V_d^s - \left[(R_s + \varepsilon R_c) + (L_d - \varepsilon L_{md})p\right] I_d^s \tag{5.63}$$

$$C = (L_d - \varepsilon L_{md}) I_d^s \tag{5.64}$$

$$D = \left(L_q - \varepsilon L_{mq}\right) I_q^s \tag{5.65}$$

$$F = V_q^s - \left[\left(R_s + \varepsilon R_c\right) + \left(L_d - \varepsilon L_{md}\right)p\right] I_q^s \tag{5.66}$$

$$G = \left(L_q - \varepsilon L_{mq}\right) I_d^s \tag{5.67}$$

$$H = V_d^s - \left[\left(R_s + \varepsilon R_c\right) + \left(L_q - \varepsilon L_{mq}\right)p\right] I_d^s \tag{5.68}$$

$$K = \left(L_d - \varepsilon L_{md}\right) I_q^s \tag{5.69}$$

Since the contribution of saliency terms in computing ω_e is negligible [57], it is reasonable to assume that the d^e and q^e axes inductances are equal [57] .

This assumption results in the following equations.

$$A = F \tag{5.70}$$

$$B = -H \tag{5.71}$$

$$G = C \tag{5.72}$$

$$K = D \tag{5.73}$$

By using the equations (5.62) to (5.73) to substitute in equation (5.61)

$$\left(A - \omega_e C\right)^2 + \left(B - \omega_e D\right)^2 = \omega_e \phi (1-\varepsilon)\sqrt{\left(B - \omega_e D\right)^2 + \left(A - \omega_e C\right)^2} \tag{5.74}$$

By taking the square of both sides and simplifying

$$\omega_e^2\left[C^2 + D^2 - \phi^2(1-\varepsilon)^2\right] - 2\omega_e(AC + BD) + \left(A^2 + B^2\right) = 0 \tag{5.75}$$

Solving for ω_e results

$$\omega_e = \frac{2(AC + BD) \pm \sqrt{4(AC + BD)^2 - 4\left(C^2 + D^2 - \phi^2(1-\varepsilon)^2\right)\left(A^2 + B^2\right)}}{2\left(C^2 + D^2 - \phi^2(1-\varepsilon)^2\right)} \tag{5.76}$$

Since the values of d and q axes inductances are in the range of few micro Henrys to milli Henrys, and the value of ϕ is in generally in the range of 0.4 to 0.6 it is clear that the denominator in equation (5.76) always tend to be a negative number. Therefore, the value of rotor speed, ω_e , can be taken as

$$\omega_e = \frac{2(AC+BD) - \sqrt{4(AC+BD)^2 - 4\left(C^2+D^2-\phi^2(1-\varepsilon)^2\right)\left(A^2+B^2\right)}}{2\left(C^2+D^2-\phi^2(1-\varepsilon)^2\right)} \qquad (5.77)$$

5.5 DSP-Based Implementation of the Estimation Algorithm

Fig. 5.12 shows the DSP-based vector control drive system which consists of an actively clamp resonant dc link inverter, an adjacent state current controller an axial gap permanent magnet synchronous machine and the TMS320C25 digital signal processor. The position and speed estimation algorithms are programmed in the TMS320C25 DSP. The flow chart of the estimation algorithm with the on-line parameter identification scheme is shown in Fig. 5.13. As shown in Fig. 5.13 the stator phase voltages and two phase currents are measured and input to the TMS320C25. The stator temperature is also measured and used as an input to the DSP. In order to have high accuracy, the average of two input samples is taken for all measured quantities. The current and voltages are then transformed to stationary reference frame values, using three phase to stationary reference transformation. The current sample at the end of the k^{th} sampling instant is then transformed to the synchronous reference frame value by using the position estimation for the $(k-1)^{th}$ sample. The synchronous reference frame

currents I_d^e and I_q^e is also output to the inner control loop for torque control. The derivative of the stationary reference frame current can also be calculated using two successive current samples. As shown in Fig. 5.12 the machine's nominal parameters and other machine constants are stored in the DSP memory. These values, transformed voltages and currents can then be used to calculate the actual machine parameters during the operation. Because the measurement of the rotor temperature is difficult, the stator temperature measurements are used to estimate the rotor temperature. The estimated rotor temperature can then be used to estimate the actual flux component of the machine. The actual machine parameters, the stationary reference frame currents, the stationary reference frame voltages and the estimated flux value can be substituted in equations (5.48) and (5.76) to estimate the rotor position and the speed respectively.

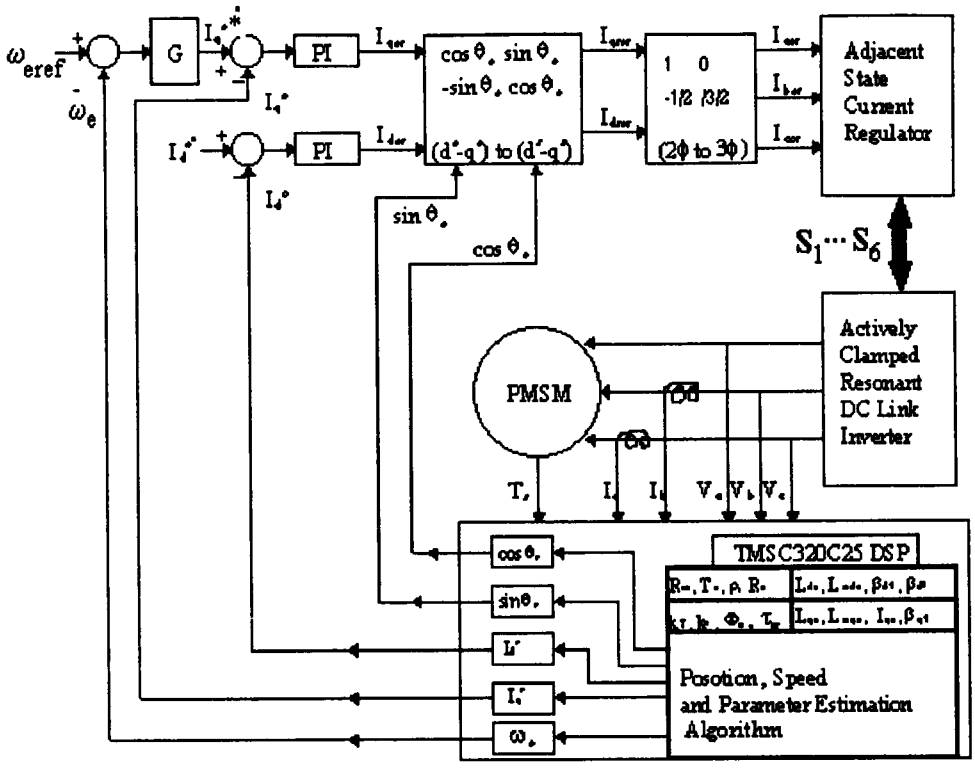


Fig. 5.12 Vector control block diagram of the drive system with estimation algorithm.

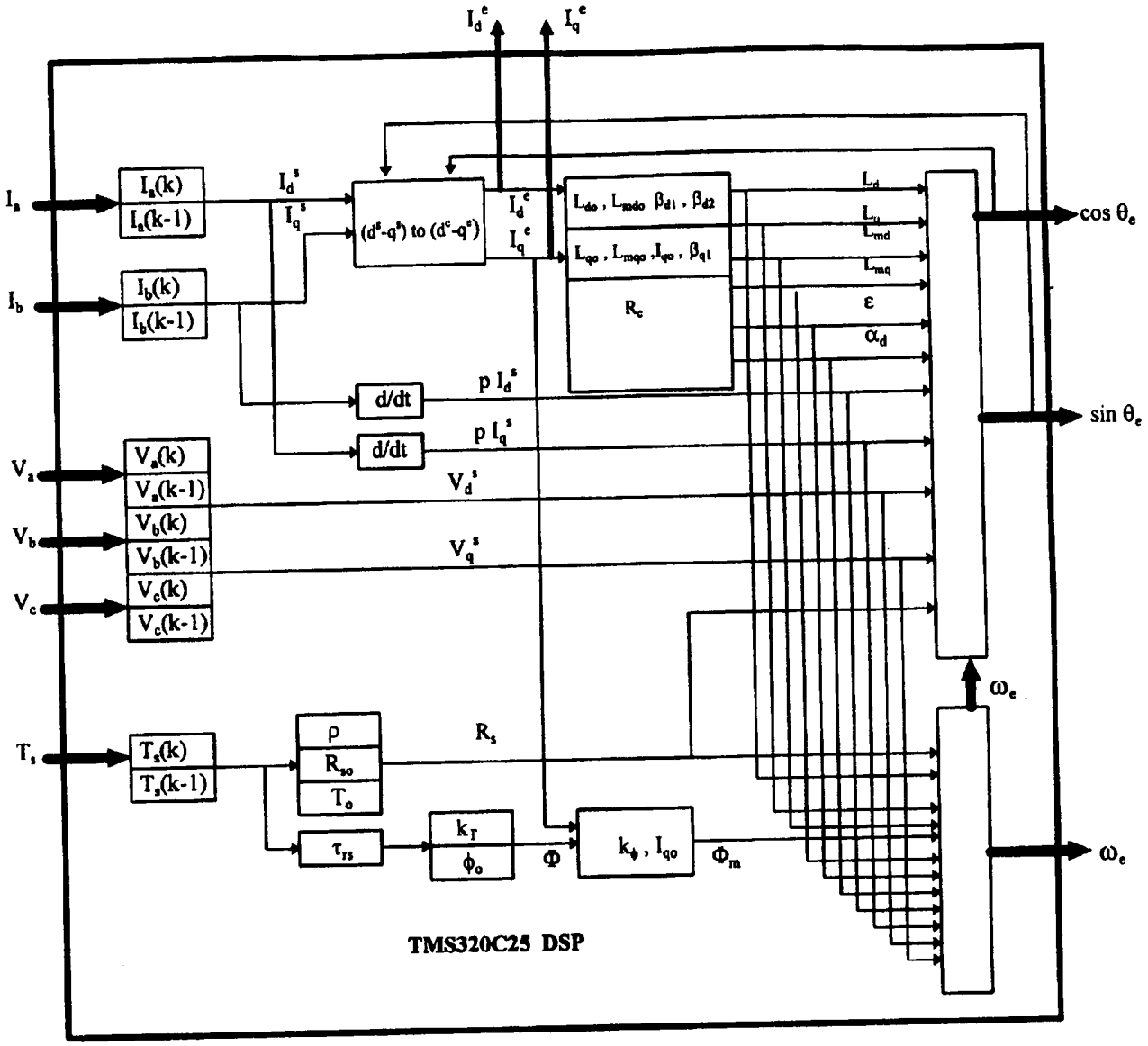


Fig. 5.13 Flow chart of the on line parameter identification and estimation algorithm.

5.6 Digital Simulation of the Drive System

The axial gap permanent magnet synchronous adjustable speed drive system shown in Fig. 5.12 is simulated using PC-based simulation language, SIMNON. In this process the drive system is divided to six main modules as shown in Fig. 5.14 [7]. First, the SIMNON codes were written separately for each module [7]. Those modules were than interconnected using SIMNON's systems connecting capabilities, through input and output signals of the different modules to formulate the integrated drive system [7].

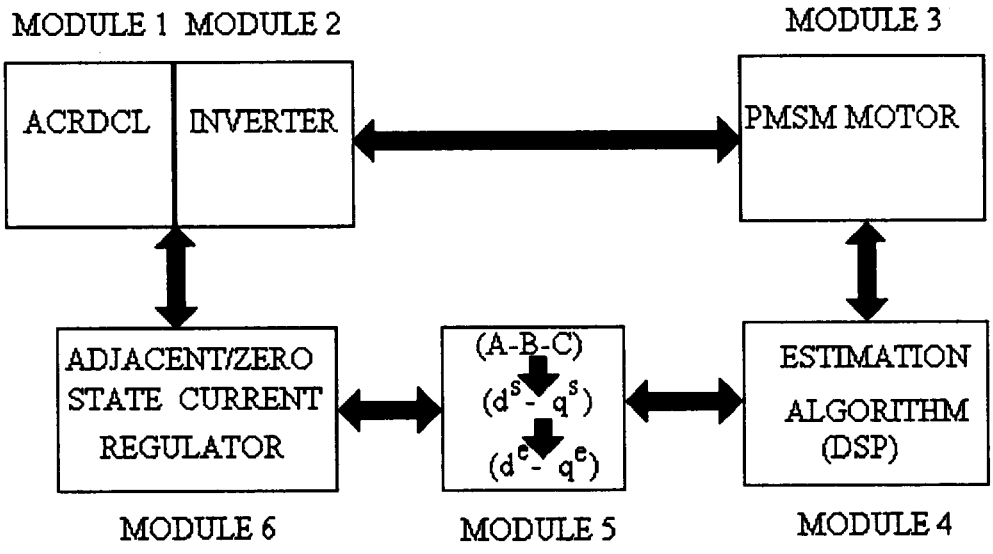


Fig. 5.14 SIMNON modules used in the simulations study.

5.6.1 Simulations Results

The SIMNON simulations for the drive system is carried out to establish the validity of the estimation algorithm. The machine parameters and other constants used in the simulations are shown in Table 5.1. The drive system parameters used in the

simulations are the same as the ones that are used in the simulation studies of [7]. Fig. 5.15 shows the estimated and actual unit vectors (Fig. 5.15b and Fig. 5.15d are in expanded time scale). Fig. 5.16 shows the actual machine currents and the reference currents generated by the estimated rotor position. Fig. 5. 17 shows the estimated and actual rotor electrical speeds.

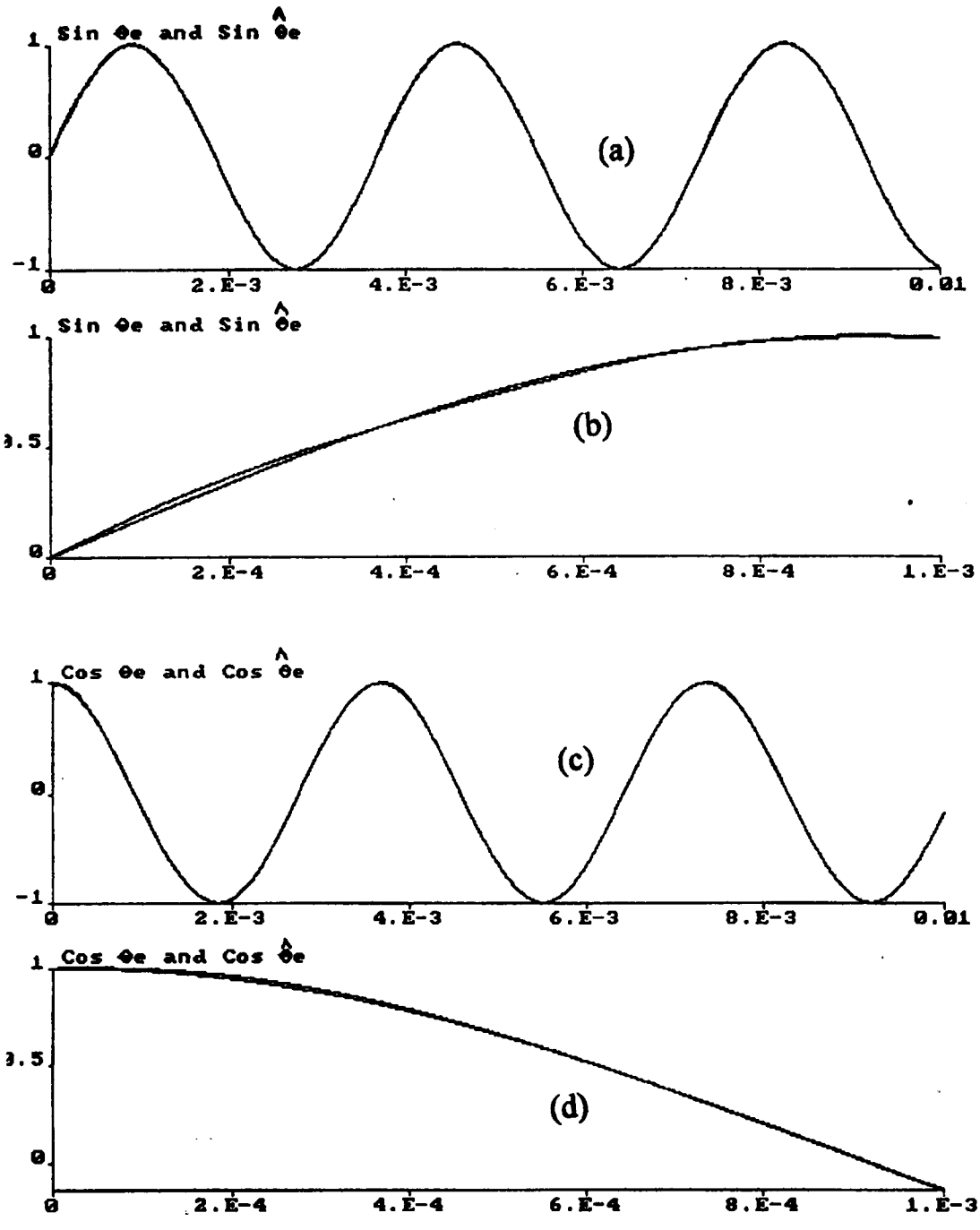


Fig. 5.15 Estimated and actual unit vectors.

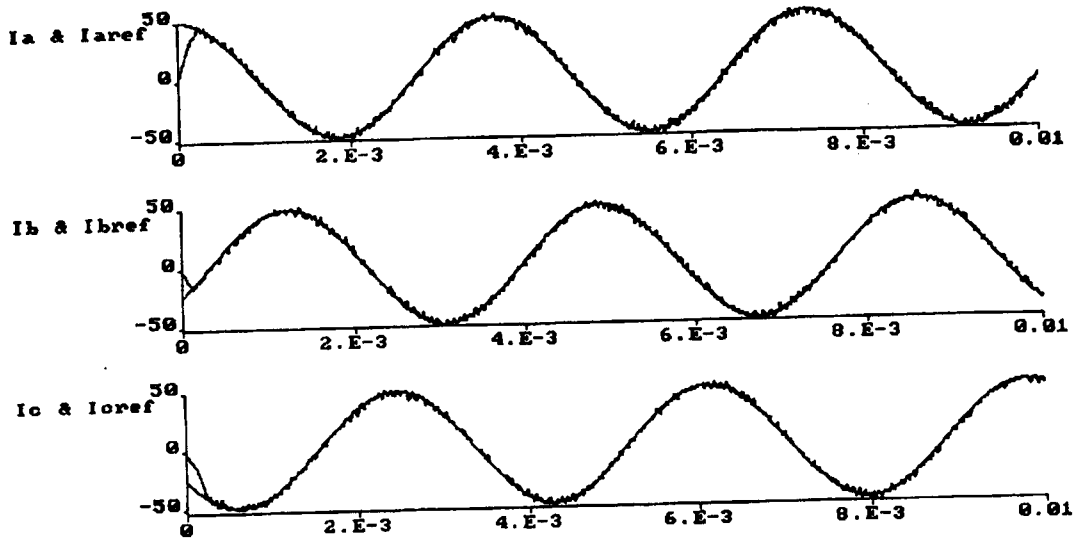


Fig. 5.16 Phase reference currents and actual motor phase currents generated by using estimated rotor position.

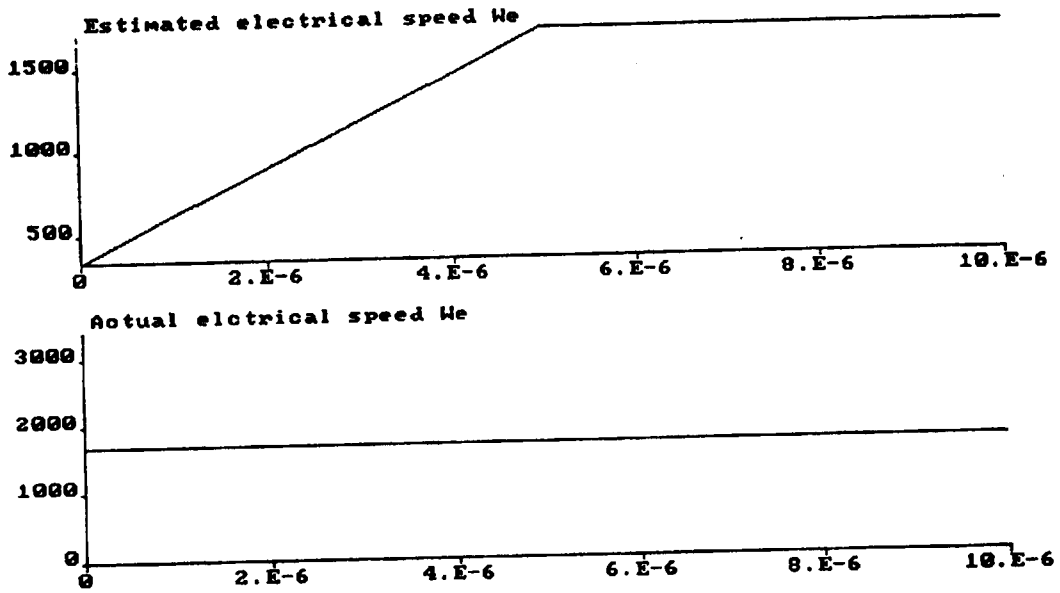


Fig. 5.17 Actual and estimated rotor speed.

CHAPTER 6

CONCLUSIONS AND RECOMMENDATIONS FOR FUTURE RESEARCH

6.1 Conclusions

In this dissertation, analysis and design/efficiency optimization of an axial gap permanent magnet brushless dc drive has been discussed. Several design optimization approaches for the axial gap permanent magnet brushless dc machine have been investigated extensively, followed by the efficiency optimization of the overall drive system. A three dimensional analytical solution to obtain the magnetic field distribution within the air gap is developed. Finally, as a further design optimization step, a position sensor elimination scheme for an axial gap permanent magnet synchronous motor drive system has been presented.

First, the inherent problems associated with permanent magnet machines have been discussed. The effective design approaches to select the machine design parameters to overcome some of these problems is presented briefly.

A simple and efficient program has been developed using QPRO for the design of a single/double stator axial gap permanent magnet synchronous machine. The equations for the machine output and performance parameters, in terms of input design parameters have been developed. A single objective optimization procedure with a constraint on efficiency has been formulated and successfully implemented for the specific power optimization of an axial gap brushless dc machine. The results show that the optimization process may result in a 40% increase in the specific power (from 1.14 to 1.69 Hp/Lb.) for the same

efficiency. The optimization has also resulted in active material cost reduction, although this may not be an absolute minimum cost (from $1161 to $611).

A multiobjective optimization procedure, which optimizes the specific power and the efficiency simultaneously, has been developed and implemented for a 100 Hp axial gap brushless dc motor. The feasibility frontier curve, which reflects a set of superior design points has been obtained. The results show that for this particular machine, the efficiency could be high as 98.06% (@ 0.69 Hp/Lb.) and the specific power could be as high as 4.54 Hp/Lb. (@ 94% efficiency).

The performance of the overall drive system has been analyzed using an Actively Clamped Resonant DC Link (ACRDCL) inverter. An analytical approach to estimate the approximate power losses of the inverter has been presented. The results of this analysis have been used to develop an efficiency optimization method for the ACRDCL inverter. The optimum parameters for the resonant link elements have been derived. At these values, the inverter losses are minimum and the optimum efficiency of the drive system is reached. However, the results show that a significant improvement cannot be obtained for the drive efficiency alone. This is due to the fact that the power losses are dominated by the frequency independent conduction losses of the main devices (approximately 80% of the total losses are due to main devices conduction loss). However, the entire optimization process has resulted in about 3% increase in the overall efficiency drive system.

An analytical three dimensional solution for the no-load flux distribution within the air gap has been discussed. This result can be used to obtain a clear insight and a better prediction of the machine performance. These results, in conjunction with a finite element analysis, can be effectively used to find the optimum magnetic parameters of the machine. The three flux components, B_r, B_θ and B_z have been calculated for a 12-pole axial gap machine whose inner and outer radius are 4.17 inches and 5.5 inches respectively. This machine is designed for the General Motors Delco Remy Division to use in their hybrid electric vehicle. The calculated field values are in close agreement with the measured resultant field.

As a further optimization step, a DSP-based scheme has been developed to eliminate the position and speed sensors used in vector control PMSM drives. This scheme estimate the rotor position and the speed by sampling the three stator voltages, two stator currents and the stator temperature. To improve the estimation accuracy, a modified d^e-q^e equivalent circuit model, which accounts for the stator core losses, has also been developed. The algorithm also takes machine parameter variations into account and performs an on-line parameter identification task. A special switching configuration for the inverter at the machine start up has been developed and presented. This enables the algorithm to estimate the rotor position at zero speed, so that estimation accuracy and effectiveness is valid over the entire speed range of the drive system.

6.2 Recommendations for Future Research

The following research topics to extend and enhance the current work are recommended.

* Develop a design program for a slot-less axial gap machine, so that further analysis can be carried out with respect to the stator core loss component and associated cogging characteristics.

* Develop a single design program, which includes the design programs for the permanent magnet synchronous machine and for the induction machine with both field configurations. This will enable the user to select a better machine depending on the application requirements.

* Extent the bi-criterion optimization process further to include the machine's cost function within the objective function. This may increase the complexity of the optimization algorithm, but it is a very attractive approach to most motor design applications.

* Further analysis and efficiency optimization of the Actively Clamped Resonant DC Link inverter system using new generation IGBTs to reduce the conduction losses.

* Develop an efficiency optimization algorithm using the modified d^e-q^e equivalent circuit, where the objective is to find the optimum frequency at which the total machine losses (i.e. I^2R losses + core losses) are minimum.

REFERENCES

REFERENCES

[1] Michael Liwschitz-Garik and Clyde C. Whipple, "Electric machinery, A-C machines, Volume 11, D. Van Nostrand Company, Inc., 1946.

[2] P. Pillay and R. Krishnan, " Modeling, analysis and simulation of a high performance, vector controlled, permanent magnet synchronous motor drive", Conference Record IEEE-IAS Annual Meeting, 1987, pp 253-261.

[3] Roy S. Colby, " Classification of inverter driven permanent magnet synchronous motors", Conference Record IEEE-IAS Annual Meeting, 1988, pp 1-6.

[4] P. Pillay and R. Krishnan, " Application characteristics of permanent magnet synchronous and brushless dc motors for servo drives", Conference Record IEEE-IAS Annual Meeting, 1987, pp 380-390.

[5] Ajith H. Wijenayake, " Design and efficiency optimization of axial-gap pm synchronous machine adjustable speed drive system", Dissertation proposal, Department of electrical and computer engineering, The university of Tennessee.

[6] C. C. Chan, " Axial field electrical machines- design and applications", IEEE Transactions on Energy Conversion, Vol EC-2, No. 2, June 1987, pp 294-300.

[7] J. M. Bailey, " Motor models and transient analysis for HTSC switch-based adjustable speed applications - phase II", Final report Feb. 94, EPRI RP 3087-16.

[8] Duane C. Hanselman, Brushless permanent-magnet motor design, McGraw-Hill, Inc., 1994.

[9] G. Amararunga, P. Acarnley and P. McLaren, "Optimum magnet circuit confogiuration for permanent magnet aerospace generators", IEEE Transactions on Aerospace and Electronics Systems, Vol AES 21, No. 2, March 1985, pp 230-254.

[10] R. Krihnan and A. J. Beutler, "Performance and design of an axial field pm synchronous motor servo drive", Conference Record IEEE-IAS Annual Meeting, 1985, pp 634-640.

[11] T. Sebastian and G. R. Slemon, "Operating limits of inverter driven permanent magnet motor drives", Conference Record IEEE-IAS Annual Meeting, 1986, pp 800-805.

[12] G. R. Slemon and X. Liu, " Core losses in permanent magnet motors", IEEE Transactions on Magnetics, Vol. 26, No. 5, Sep. 1990.

[13] J. A. Moss, J. L. Kirtley, J. H. Lang, R. D. Tabors and F. de. Cuadra, " A computer-based design assistant for induction motors", Conference Record IEEE-IAS Annual Meeting, 1991, pp 1-6.

[14] H. A. Toliyat, M. M. Rahiman and T. A. Lipo, "d-q modelling of the phase synchronous reluctance machine including third harmonic of air gap MMF", Conference Record IEEE-IAS Annual Meeting, 1991, pp 231-237.

[15] H. A. Toliyat, L. Xu and T. A. Lipo, "A five phase reluctance motor with high specific torque, Conference Record IEEE-IAS Annual Meeting, 1990, pp 207-213.

[16] P. J. McCleer, J. M. Bailey and B. Banerjee, " Five phase trapezoidal back emf pm synchronous machines and drives", European Power Electronics Conference, 1991.

[17] J. M. Bailey, J. S. Lawler and P. J. McCleer, "Design optimization of a quasi square wave permanent magnet motor/inverter for variable speed, smooth torque applications, EPRI report, RP3087-07.

[18] Olorunfemi Ojo, "Multiobjective optimum design of electrical machines for variable speed motor drives", Conference Record IEEE-IAS Annual Meeting, 1991, pp 163-168.

[19] P. Campbell, "The magnetic circuit of an axial field dc electrical machine", IEEE transactions on Magnetics, Vol Mag.-11, No. 5 Sep. 1975, pp 1541-1543.

[20] T. A. Lipo and Feng. X. Wang, "Design and performance of a converter optimized ac machine", IEEE Transactions on Ondustry Applications, Vol IA-20, No. 4, Jul.-Aug. 1984, pp 834-844.

[21] J. M. Bailey, R. A. Hawsey, D. S. Daniel and R. J. Thomas, "Design of a high power density permanent magnet axial gap dc motor" Proceedings of IEEE Southeastern Conference, April 90.

[22] H. Takano, T. Ito, K. Mori, A. Sakuta and H. Hirasa, "Optimium value for magent and armature winding thickness for axial field permanent magnet brushless dc motors", Conference Record IEEE-IAS Annual Meeting, 1990, pp 157-162.

[23] W. S. Leung and C. C. Chan, "A new design approach for axial field electrical machines", IEEE Transactions on Power Apparatus and Systems, Vol. PAS-94, No. 4, Jul-Aug. 1980, pp 1679-1685.

[24] D. Platt, "Permanent magnet synchronous motor with axial flux geometry", IEEE Transactions on magnetics, Vol. 25, No. 4, Jul. 1989, pp 3076-3079.

[25] J. B. Patton, "Axial gap brushless dc machine design considerations" Feb. 1990.

[26] W. F. Xiang and Z. B. Yi, "Waveform optimization design of a converter ac machine", Conference Record IEEE-IAS Annual Meeting, 1987, pp 92-97.

[27] P. Pillay and P. Freere, " Literature survey of permanent magnet ac motors and drives", Conference Record IEEE-IAS Annual Meeting, 1989, pp 74-84.

[28] Hendrick R. van Niekerk and J. D. van Wyk, "Electric machines: A new formulation for the power-mass-efficiency-speed relationship", Conference Record IEEE-IAS Annual Meeting, 1992, pp 86-91.

[29] A. Kaddouri and H. Le-huy, "Analysis and design of a slotless Nd-Fe-B permanent magnet synchronous motor for direct drive", Conference Record IEEE-IAS Annual Meeting, 1992, pp 271-278.

[30] M. Hippner and R. G. Harley, "Looking for an optimal rotor for hgih speed permanent magnet synchronous machine", Conference Record IEEE-IAS Annual Meeting, 1992, pp 265-270.

[31] H. A. Toliyat, T. A. Lipo and J. C. White, " Analysis of a concentrated windign induction machine for adjustable speed drive applications, part 1 (motor analysis), IEEE transactions on Energy Conversion, Vol. 6, No. 4, Dec. 1994, pp 679-683.

[32] D. M. divan and G. Skibinski, "Zero switching loss inverters for high power applications", Conference Record IEEE-IAS Annual meeting, 1987, pp 627-634.

[33] D. M. Divan, G. Venkataramanan and R. W. De Doncker, " Design Methodologies for soft switched inverters", Conference Record IEEE-IAS Annual Meeting, 1988, pp 758-766.

[34] D. M. Divan, "The resonant dc link converter- A new concept in static power conversion", Conference Record IEEE-IAS Annual Meeting, 1986, pp 648-656.

[35] R. D. Lorenz and D. M. Divan, "Dynamic analysis & experimental evaluation of delta modulators for field oriented ac machine current regulators", Conference Record IEEE-IAS Annual Meeting , 1988, pp 196-201.

[36] G. Venkataramanan and D. M. Divan, "Pulse width modulation with resonant dc link converters", Conference Record IEEE-IAS Annual Meeting, 1990, pp 984-990.

[37] D. M. Divan and A. Mertens, " A high frequency resonant dc link inverter using IGBTs", Soft switching converters: topologies, design and control, summary of publications 1986-1990, Department of Electrical and Computer Engineering, University of Wisconsin-Madison, pp 141-149.

[38] A. Nasar, "Electromagnetic theory of electrical machines", Proceedings, IEE, Vol 111, No. 6, Jun. 1964, pp 1123-1131.

[39] P. J. Lawrenson and M. C. Ralph, "General 3-dimensional solution of eddy-cuurent and laplacian fields in cylindrical structures", Proceedings, IEE, Vol. 117, No. 2, Feb. 1970.

[40] E. Mukai, I. Muta and M. Yagi, " Three-dimensional analysis of inductance and magnetic fields in the air-cored armature windings of a superconducting synchronous machine", Electrical Engineering in Japan, Vol. 100, No. 2, 1980, pp 72-79.

[41] E. Mukai, I. Muta and M. Yagi, " Three-dimensional analysis of self-inductance and magnetic fields in the air-cored armature winfdings of a superconducting synchronous machine", Electrical Engineering in Japan, Vol. 99, No. 4, 1979, pp 25-32.

[42] N. Boules, " Prediction of no-load flux density distribution in permanent magnet machines", IEEE Transactions on Industry Applications, Vol. IA-21, No. 4, May-Jun. 1985, pp 633-643.

[43] B. Ancelle and J. C. Sabonnadiere, "Numerical solution of 3D magnetic field problems using boundary integral equations", IEEE Transactions on Magnetics, Vol. Mag-16, No. 5, Sep. 1980, pp 1089-1091.

[44] M. V. K. Chari, Z. J. Csendes, P. Silvester, A. Konrad and M. A. Palmo, "Three-dimensional magnetostatic field analysis of electrical machinery by the finite-element method", IEEE Transactions on Power Apparatus and Systems, Vol. PAS-100, No. 8, August 1981, pp 4007-4019.

[45] H. Weh and N. boules, "Field analysis for a hgih-power, high-speed permanent magnet synchronous machine of the disc construction type", Electric Machines and Electromechnics, Vol. 5, 1980, pp 25-37.

[46] J. D'Angelo, M. V. K. Chari and P. Campbell, "Three-dimensional finite element solution for a permanent magnet axial-field machine", IEEE Transactions on Power Apparatus and Systems, Vol. PAS 102, No. 1, Jan. 1983, pp 83-90.

[47] N. Boules and H. Wey, "Machine constants and design considerations of a high-power, high-speed permanent magnet disc type synchronous machine", Electric Machines and Electromechanics, Vol. 5, 1980, pp 113-123.

[48] N. Boules, "Two-dimensional field analysis of cylindrical machines with permanent magnet excitation", IEEE Transactions on Industry Applications, Vol. IA-20, No. 5, sep-Oct 1984, pp 1267-1277.

[49] C. J. Carpenter, "3-dimensional magnetic field and eddy current problems at power frequencies", Proceedings, IEE, Vol. 124, No. 11, Nov. 1977, pp 1026-1034.

[50] B. K. Bose, Power electronics and ac drives, Prentice Hall, 1986.

[51] B. K. Bose, "Variable frequency drives- technology and applications", IEEE International Symp. on Industrial Electronics Conference Record , 1993, pp 1-18.

[52] N. Mohan, T. M. Undeland and W. P. Robbins, Power electronics-converters, applications and design, John Wiley & Sons, 1989.

[53] P. H. Mellor, F. B. Chaaban and K. J. Binns, "Estimation of parameters and performance of rare-earth permanent magnet motors avoiding measurement of load angle", IEE proceedings-B, Vol. 138, No. 6, Nov. 1991, pp 322-330.

[54] V. B. Honsinger, "Performance of polyphase permanent magnet machines, IEEE Transactions on Power Apparatus and Systems, Vol. PAS-99, No. 4, Jul./Aug. 1980, pp 1510-1516.

[55] P. H. Mellor, M. A. Al-Taee and K. J. Binns, "Open loop stability characteristics of synchronous drive incorporating high field permanent magnet motor", IEE Proceedings-B, Vol. 138, No. 4, Jul. 1991, pp 175-184.

[56] R. Krishnan and P. Pillay, "Parameter sensitivity in vector controlled ac motor drives", IEEE IECON Proceedings, 1987, pp 212-218.

[57] M. Naidu and B. K. Bose, "Rotor position estimation scheme of a permanent magnet synchronous machine for high performance variable speed drive", Conference Record IEEE-IAS Annual Meeting, 1992, pp 48-53.

[58] R. S. Colby, "Efficient operation of surface mounted permanent magnet synchronous motors", Conference Record IEEE -IAS Annual Meeting, 1986, pp 806-813.

[59] Ajith H. Wijenayake, B. K. Bose, "Position and Speed Estimation of a Permanent Magnet Synchronous Machine Using a High Speed Digital Signal Processor for High Performance Industry Applications", Project Report , Department of Electrical & Com. Eng. , University of Knoxville, Dec. 1990.

[60] L. A. Jones and J. H. Lang, "A State Observer for the Permanent Magnet Synchronous Motor", IEEE IECON Proceedings, 1987, pp. 197-204.

[61] A. B. Kulkarni and M. Eshani, "A Micro-computer Based Position Sensor Elimination Scheme for the Interior Permanent Magnet Synchronous Motor Drive", Conference Record IEEE -IAS Annual Meeting, 1989, pp. 773-779.

[62] H. Watanabe, T. Isii and T. Fuji, "DC Brushless Servo System Without Rotor Position and Speed Sensor, " IEEE IECON Proceedings, 1987, pp. 238-234.

[63] B. K. Bose, "A High Performance Inverter Fed Drive System of an Interior Permanent Magnet Synchronous Machine", IEEE Transactions, Vol. 24, No. 6, Nov./Dec. 1988.

[64] C. V. Jones, Unified Machine Theory, Plenum Press, New York, 1968.

[65] T. A. Lipo, D. M. Novotny, " Electrical machine design notes", Department of Electrical and Computer Engineering, University of Wisconsin-Madison.

[66] N.N. Lebedev," Special functions and their applications", Prentice-Hall, Inc., Englewood Cliffs, NJ, 1965.

[67] Francis B. Hildebrand, "Advanced calculas for applications", Prentice-Hall, Engle Wood, Cliffs, NJ, 1965.

[68] David E. Johnson and Johnny R. Johnson, "Mathematical methods in engineering and physics, special functions and boundary problems", The Ronald Press Company, New York, 1965.

[69] A. H. Wijenayake, J. M. Bailey and M. Naidu, "A DSP-based position sensor elimination method with an on-line parameter identification scheme for permanent magnet synchronous motor drives", To be presented at the IEEE IAS 30th Annual Meeting, 1995.

[70] A. H. Wijenayake, J. M. Bailey and P. J. McCleer, "Design optimization of an axial gap permanent magnet brushless dc motor for electric vehicle applications", To be presented at the IEEE IAS 30th Annual Meeting, 1995.

APPENDICES

APPENDIX A1

FORMULATION OF THE OPTIMIZATION PROBLEM USING QPRO

A1.1 Introduction

This appendix describes QPRO's built-in Optimizer[1], the commands on the Optimizer menu, and how the Optimizer is used to find the optimum specific power with a constraint on the efficiency for a given design problem. To use Optimizer, the machine design model containing the input design parameters should be entered into a spreadsheet as shown in Table A1. Then using equations (2.9) to (2.61), output data and performance parameters are obtained in terms of input parameters and programmed into the same spreadsheet. This is shown in Table A2. The parameters shown in Table A1 and Table A2 are obtained using the classical design approach as discussed in section 2.2.13. These values can be used as the starting design parameters for the optimization process.

A1.2 Optimizer Menu

The Optimizer menu allows the programmer to define the solution cell, the variable cells, the constraints cells, and the options that can be used during the optimization process. The Optimizer menu can be displayed by selecting the command /Tools| Optimizer.

A1.2.1 Solution Cell

Define the solution cell as the cell which contains the formula for the specific power. This cell contains a highly non-linear function whose parameters are the input

[1] Optimizer is the menu driven, built-in optimization algorithm in QPRO

design parameters given in Table A1. When the solution cell is defined, a menu appears, which indicates whether the optimization problem is a Maximization, Minimization or a Equal value. Then select the Maximization from the menu. These selections result in the following:

Solution Cell = B67

Type of optimization = Maximization

A1.2.2 Variable Cells

The variable cells are cells whose values the Optimizer adjusts to reach an optimal solution. The variable parameters should be in a continuous block of cells. Table A3 shows the block of variable cells selected from the Table A1. If required, the cells B18 to B31 can also be regarded as variables. However, here they are considered as fixed parameters. Optimizer allows up to 200 variable cells.

A1.2.3 Constraints

The constraints are the limitations placed on the variable cells and other cells. The constraint conditions may either be equal, unequal or a range. The Optimizer allows up to 100 constraints to be used in the optimization process. The constraint conditions used in this particular design are given below.

$$B4 \leq 6 \qquad \text{(A1.1)}$$

$$B5 \geq 3 \qquad \text{(A1.2)}$$

Table A1.1 Input design parameters

PARAMETER	VALUE	CELL #	UNITS
Rated power/ Stator	50	B2	Hp
Rated speed	1800	B3	Rpm
Magnet outside radius	5.886	B4	Inch
Magnet inside radius	3.000	B5	Inch
Magnet axial thickness	0.35	B6	Inch
Magnet remanence	1.100	B7	Tesla
Magnet recoil permeability	1.05	B8	_
Air gap	30	B9	mils
Stator iron axial thickness	1.800	B10	Inch
Number of phases	3	B11	_
Number of poles	16	B12	_
Number of parallel circuit/phase	1	B13	_
Number of parallel wires/conductor	4	B14	_
Number of conductors/slot	12	B15	_
Stator average slot opening factor	0.70	B16	_
Stator slot width multiplication factor	0.85	B17	_
Stator slot tip depth	35	B18	mils
Stator slot wedge depth	43	B19	mils
Wire AWG	18	B20	_
Wire diameter	0.0403	B21	Inch
Wire resistance/1000 Ft.	6.61	B22	Ohm
Number of wires/square inch	450	B23	_
Wire weight per 1000 Ft.	4.92	B24	Lb.
Continuos current rating of wire	5.00	B25	Amps
Distance between two coil sides	60	B26	mils

Coil extension at outer radius	0.25	B27	Inch
Coil extension at inner radius	0.25	B28	Inch
Slot insulation thickness	7	B29	mils
Slot fill factor	0.60	B30	_
Magnet space thickness	0.063	B31	Inch

Table A1.2 Output and performance parameters

PARAMETER	VALUE	CELL #	UNITS
Torque	145.88	B33	Ft-Lb.
Active radial length	2.89	B34	Inch
Tooth width at inside radius	0.225	B35	Inch
Shoe width at inside radius	0.276	B36	Inch
Slot width at inside radius	0.167	B37	Inch
Slot opening at inside radius	0.116	B38	Inch
Slot opening/(2* air gap)	1.95	B39	_
Carter's coefficient	1.15	B40	_
Effective gap length	34.6	B41	mils
Area of magnet/ area of gap	0.95	B42	_
B- gap at stator iron surface	0.949	B43	Tesla
Peak flux per pole	0.08	B44	mV-sec
B_{max} at tooth inside radius	1.650	B45	Tesla
Required slot area	0.178	B46	$Inch^2$
Required slot depth	1.169	B47	Inch
B_{max} at stator yoke	1.985	B48	Tesla
Phase current	65.64	B49	Amps
Slot current density	1071	B50	$A/Inch^2$
Line-line back emf at rated speed	567.99	B51	Volts
V(L-L)+I*R drop+ Inverter switch drop	593.00	B52	Volts
Mean turn length	11.22	B53	Inch
Phase resistance	148.30	B54	mOHm
Phase inductance	0.241	B55	mH
Inverse time constant	616.02	B56	$sec.^{-1}$

		B57	
Stator teeth volume	69.52	B58	$Inch^3$
Stator back iron volume	44.49	B59	$Inch^3$
Stator iron volume	114.01	B60	$Inch^3$
		B61	
Weight of the stators	62.93	B62	Lb.
Magnet weight	15.40	B63	Lb.
Wire weight	5.30	B64	Lb.
Rotor weight	19.55	B65	Lb.
Total active material weight	87.77	B66	Lb.
Specific power	1.14	B67	Hp/Lb.
Total active material cost	1161	B68	$
		B69	
I^2*R loss at rated current	1278.03	B70	Watts
Teeth loss at rated speed	304.17	B71	Watts
Yoke loss at rated speed	147.57	B72	Watts
Efficiency at rated speed & torque	95.57	B73	%

Table A1.3 Block of variable cells

PARAMETER	CELL #	UNITS
Magnet outside radius	B4	Inch
Magnet inside radius	B5	Inch
Magnet axial thickness	B6	Inch
Magnet remanence	B7	Tesla
Magnet recoil permeability	B8	_
Air gap	B9	mils
Stator iron axial thickness	B10	Inch
Number of phases	B11	_
Number of poles	B12	_
Number of parallel circuit/phase	B13	_
Number of parallel wires/conductor	B14	_
Number of conductors/slot	B15	_
Stator average slot opening factor	B16	_
Stator slot width multiplication factor	B17	_

$$B6 \geq 0.2 \qquad \text{(A1.3)}$$

$$B7 = 1.10 \qquad \text{(A1.4)}$$

$$B8 = 1.05 \qquad \text{(A1.5)}$$

$$B9 \geq 20 \qquad \text{(A1.6)}$$

$$B10 \leq 4.0 \qquad \text{(A1.7)}$$

$$B11 = 3 \qquad \text{(A1.8)}$$

$$B12 \geq 2 \qquad \text{(A1.9)}$$

$$B12 \leq 24 \qquad \text{(A1.10)}$$

$$B13 \geq 1 \qquad \text{(A1.11)}$$

$$B14 \geq 1 \qquad \text{(A1.12)}$$

$$B16 \geq 0.1 \qquad \text{(A1.13)}$$

$$B17 \leq 1.75 \qquad \text{(A1.14)}$$

$$B45 \leq 2 \qquad \text{(A1.15)}$$

$$B48 \leq 2 \qquad \text{(A1.16)}$$

$$B73 \geq 94.00 \qquad \text{(A1.17)}$$

$$B52 = 600 \qquad \text{(A1.18)}$$

$$B50 \leq 6452 \qquad \text{(A1.19)}$$

$$B25 - \frac{B49}{(B13 * B14 * B15)} \geq 0.25 \qquad \text{(A1.20)}$$

$$\frac{B12}{2} = Integer \qquad \text{(A1.21)}$$

$$\frac{B12}{B13} = Integer \qquad \text{(A1.22)}$$

$$\frac{B15}{2} = Integer \qquad \text{(A1.23)}$$

$$B14 = Integer \qquad \text{(A1.24)}$$

A1.2.4 Options Menu

The options menu offers additional setting that can be used to save time or/and to improve accuracy of the optimization algorithm. The options menu gives the following settings to control the optimization process.

* **Max time**: This indicates that how long Optimizer can spend looking for the optimum solution. This can be set to any value between 1 and 1000 seconds. The default is 100.

* **Max Iterations**: This sets the maximum number of iterations Optimizer can perform to find the optimum solution. This value can be set to any value between 1 and 1000 iterations. The default value is 100.

* **Precision**: This controls the accuracy of Optimizer solution. This value can take any value between 0 and 1. The default setting is 0.0005

* **Linear or Non-Linear:** This indicates whether Optimizer uses Linear or Non-linear methods to solve the optimization problem. Since the design optimization problem is a highly non-liner problem, this setting always should be set to non- linear.

* **Estimates**: This specifies the approach used to obtain initial estimates of the variable parameters in each iteration. This allows to select between Tangent method and Quadratic method. Tangent method uses linear extrapolation from a tangent vector, while

Quadratic uses quadratic extrapolation. Selecting Quadratic can be helpful in highly non-linear problems.

* **Derivatives:** This select the Forward or Central differencing for estimates of partial derivatives. Central requires more calculations than Forward method.

* **Search:** This selects a method for computing the search direction during the optimization process. This may either be Newton or Conjugate. Newton method is a quasi-Newton method and requires less computational time and work. Conjugate method can be used to reach an optimum solution, if the objective function is changing too slowly.

* **Answer Report:** This allows programmer to select an area of the spreadsheet to list the solution cell and variable cells with their original values, final values and variable dual values. This also provides a report on constraints and their dual values.

* **Detail Report:** This allows the programmer to select an area of the spreadsheet to produce a detailed report that lists the iteration number and the corresponding variable cells values and the solution cell value.

* **Go:** This command executes the search for the optimum solution and automatically replaces the initial variable cells values and corresponding output and performance parameters with their optimum values.

The final results of these steps are shown in Table A4 -Table A8.

A1.2.5 A Brief Description of Quasi-Newton Methods

In Quasi-Newton methods, for maximizing a differentiable function, $F(x)$ of several variables, the following procedure is implemented. At some iteration k of the method, given the current point X_k , the following two steps are performed:

(i) Determine a search direction, d_k , and

(ii) Determine the step, λ_k along the direction d_k to find the next iterating point, X_{k+1} , given by equation (A1.25):

$$X_{k+1} = X_k + \lambda_k d_k \qquad \text{(A1.25)}$$

The search direction is determined using a positive definite symmetric matrix, D_k that approximates the inverse of the Hessian matrix of the function $F(x)$. The search direction is given by equation (A1.26):

$$d_k = -D_k \nabla F(x) \qquad \text{(A1.26)}$$

The positive definiteness of the matrix D_k ensure that d_k is a descent direction whenever $\nabla F(x) \neq 0$. The step λ_k is determined using a cross section of the function, F to be maximized. If the λ_k is an optimal solution to the problem, then λ_k can be obtained by equations (A1.27) and (A1.28):

$$\text{Maximize } -F(X_k + \lambda_k d_k) \qquad \text{(A1.27)}$$

$$\text{Subject to } \lambda_k \geq 0 \qquad \text{(A1.28)}$$

The Hessian matrix can now be updated according to the new iterating point, X_{k+1}. Then, steps (i) and (ii) are repeated until the optimum solution is reached.

Table A1.4 Optimal design parameters.

Answer report			
Solution cell:	**Starting**	**Final**	
Specific power	**1.13**	**1.69**	
Variable cells:	Starting	Final	Dual value
Magnet outer radius	5.899	6.000	0.29
Magnet inner radius	3.000	3.597	0.00
Magnet axial thickness	0.35	0.20	-0.79
Magnet permeance	1.10	1.10	0.00
Recoil permeability	1.05	1.05	0.00
Air gap	30	20	-0.00
Stator axial thickness	1.8000	1.4446	0.00
No. of phases	3	3	0.00
No. of poles	16	18	0.00
No. of parallel cct	1	1	0.00
No. of parallel wires	4	4	0.00
No. of conductors per slot	12	12	0.00
Stator slot opening factor	0.70	0.15	-0.00
Slot width multip. factor	0.85	1.05	0.00

Table A1.5 Constraints and optimal values.

Report on constraints					
Parameter or Constraints	**Value**	**Constra.**	**Binding**	**Slack**	**Dual value**
Mag. outer radius	6.000	6	Yes	0.000	0.00
Magnet inner radius	3.597	3	No	-0.597	0.00
Mag. axial thickness	0.20	0.2	Yes	0.00	0.00
Mag. axial thickness	0.20	0.5	No	0.30	0.00
Magnet permeance	1.10	1.10	Yes	0.00	0.00
Recoil permeability	1.05	1.05	Yes	0.00	0.00
Air gap	20	20	Yes	0.00	0.00
Stator axial thickness	1.4446	1	No	-0.4446	0.00
Stator axial thickness	1.4446	4	No	2.5554	0.00
No. of phases	3	3	Yes	0	0.00
No. of poles	18	24	No	6	0.00
No. of poles	18	2	No	-16	0.00
No. of parallel cct	1	1	No	0	0.00
No. of parallel wires	4	1	No	-3	0.00
No. of conductors per slot	12	2	No	-10	0.00
Stator slot opening factor	0.15	0.1	No	-0.05	0.00
Stator slot opening factor	0.15	1.0	No	0.85	0.00
Slot width multip. factor	1.05	1.75	No	0.70	0.00
Active radial length	2.40	0.5	No	-1.90	0.00
B_{tmax}	2.00	2.00	Yes	0	0.47
B_{ymax}	2.00	2.00	Yes	0	0.29
Winding current density	1058	3871	No	2813	0.00
V_l + IR drop+ Inv. sw.drop	600	600	Yes	0	0.00
Efficiency	95.71	94.00	No	-1.71	0.00
Even no of poles	0	0	Yes	0.00	0.13
Integer no of parallel cct.	0	0	Yes	0.00	0.00
Integer no of parallel wires	0	0	Yes	0.00	-0.21
Even no of conductors/slot	0	0	Yes	0.00	0.14
Current tolerance in a wire	3.65	0.25	No	-3.40	0.00

Table A1.6 Detail report of each iteration step.

Ite. #	R_o	R_i	T_{mn}	B_r	m_r	g	T_{sa}	N_{ph}	N_{mp}	N_p	N_w	N_c	S_{of}	S_{wm}	P_{sp}
Start	5.89	3.00	0.35	1.10	1.05	30	1.80	3	16	1	4	12	0.70	0.85	1.13
# 1	5.89	3.00	0.35	1.10	1.05	30	1.80	3	18	1	4	12	0.70	0.85	1.16
# 2	5.76	3.07	0.27	1.10	1.05	30	1.81	3	18	1	4	12	0.71	0.86	1.30
# 3	5.77	3.08	0.27	1.10	1.05	30	1.83	3	18	1	4	12	0.71	0.91	1.28
# 4	5.77	3.07	0.25	1.10	1.05	30	1.83	3	18	1	4	12	0.70	0.91	1.35
# 5	5.79	3.07	0.22	1.10	1.05	30	1.75	3	18	1	4	12	0.69	1.04	1.49
# 6	5.83	3.06	0.21	1.10	1.05	30	1.57	3	18	1	4	12	0.69	1.11	1.56
# 7	5.84	3.06	0.20	1.10	1.05	30	1.49	3	18	1	4	12	0.68	1.12	1.57
#8	5.86	3.06	0.20	1.10	1.05	30	1.49	3	18	1	4	12	0.68	1.12	1.57
#9	5.86	3.34	0.20	1.10	1.05	29.9	1.41	3	18	1	4	12	0.66	1.12	1.63
#10	6.0	3.45	0.20	1.10	1.05	20	1.42	3	18	1	4	12	0.10	1.09	1.65
# 11	6.0	3.60	0.20	1.10	1.05	20	1.44	3	18	1	4	12	0.10	1.05	1.69
# 12	6.0	3.59	0.20	1.10	1.05	20	1.44	3	18	1	4	12	0.15	1.05	1.69
# 13	6.0	3.59	0.20	1.10	1.05	20	1.44	3	18	1	4	12	0.15	1.05	1.69
Opti	**6.0**	**3.60**	**0.20**	**1.10**	**1.05**	**20**	**1.44**	**3**	**18**	**1**	**4**	**12**	**0.15**	**1.05**	**1.69**
# 15	6.0	3.89	0.21	1.10	1.05	49.9	1.85	3	8	1	3	32	0.35	1.13	1.29
# 16	6.0	3.86	0.20	1.10	1.05	49.9	1.84	3	8	1	3	32	0.33	1.14	1.29
# 17	6.0	3.86	0.20	1.10	1.05	49.9	1.84	3	8	1	3	32	0.33	1.14	1.29
# 18	6.0	3.88	0.20	1.10	1.05	49.9	1.85	3	8	1	3	32	0.20	1.14	1.29
# 19	6.0	3.89	0.20	1.10	1.05	30.8	1.85	3	8	1	3	32	0.19	1.13	1.29
# 20	6.0	4.10	0.20	1.10	1.05	20	1.95	3	8	1	3	32	0.12	1.06	1.32
# 21	6.0	4.21	0.20	1.10	1.05	20	2.03	3	8	1	3	32	0.16	1.01	1.33
# 22	5.78	3.87	0.20	1.10	1.05	20	2.04	3	8	1	3	32	0.29	1.01	1.33
# 23	5.72	3.77	0.20	1.10	1.05	20	2.04	3	8	1	3	32	0.43	1.02	1.33
# 24	5.81	3.86	0.20	1.10	1.05	20	1.99	3	8	1	3	32	0.72	1.04	1.34
# 25	5.85	3.93	0.20	1.10	1.05	20	1.99	3	8	1	3	32	0.69	1.04	1.34
Final	5.85	3.93	0.20	1.10	1.05	20	2	3	8	1	3	32	0.70	1.04	1.34

Table A1.7 Optimized input design parameters.

OPTIMIZED PARAMETER	VALUE	CELL #	UNITS
Rated power/ Stator	50	B2	Hp
Rated speed	1800	B3	Rpm
Magnet outside radius	6.000	B4	Inch
Magnet inside radius	3.597	B5	Inch
Magnet axial thickness	0.20	B6	Inch
Magnet remanence	1.100	B7	Tesla
Magnet recoil permeability	1.05	B8	_
Air gap	20	B9	mils
Stator iron axial thickness	1.4446	B10	Inch
Number of phases	3	B11	_
Number of poles	18	B12	_
Number of parallel circuit/phase	1	B13	_
Number of parallel wires/conductor	4	B14	_
Number of conductors/slot	12	B15	_
Stator average slot opening factor	0.15	B16	_
Stator slot width multiplication factor	1.05	B17	_
Stator slot tip depth	35	B18	mils
Stator slot wedge depth	43	B19	mils
Wire AWG	18	B20	_
Wire diameter	0.0403	B21	Inch
Wire resistance/1000 Ft.	6.61	B22	Ohm
Number of wires/square inch	450	B23	_
Wire weight per 1000 Ft.	4.92	B24	Lb.
Continuos current rating of wire	5.00	B25	Amps
Distance between two coil sides	60	B26	mils

Coil extension at outer radius	0.25	B27	Inch
Coil extension at inner radius	0.25	B28	Inch
Slot insulation thickness	7	B29	mils
Slot fill factor	0.60	B30	_
Magnet space thickness	0.063	B31	Inch

Table A1.8 Optimized output and performance parameters.

OPTIMIZED PARAMETER	VALUE	CELL #	UNITS
Torque	145.88	B33	Ft-Lb.
Active radial length	2.40	B34	Inch
Tooth width at inside radius	0.198	B35	Inch
Shoe width at inside radius	0.384	B36	Inch
Slot width at inside radius	0.220	B37	Inch
Slot opening at inside radius	0.116	B38	Inch
Slot opening/(2* air gap)	0.85	B39	_
Carter's coefficient	1.02	B40	_
Effective gap length	20.50	B41	mils
Area of magnet/ area of gap	0.95	B42	_
B- gap at stator iron surface	0.949	B43	Tesla
Peak flux per pole	0.07	B44	mV-sec
B_{max} at tooth inside radius	2.000	B45	Tesla
Required slot area	0.177	B46	$Inch^2$
Required slot depth	0.870	B47	Inch
B_{max} at stator yoke	2.000	B48	Tesla
Phase current	64.88	B49	Amps
Slot current density	1058	B50	$A/Inch^2$
Line-line back emf at rated speed	574.62	B51	Volts
V(L-L)+I*R drop+ Inverter switch drop	600	B52	Volts
Mean turn length	10.04	B53	Inch
Phase resistance	149.38	B54	mOHm
Phase inductance	0.378	B55	mH
Inverse time constant	395.41	B56	$sec.^{-1}$

		B57	
Stator teeth volume	40.64	B58	$Inch^3$
Stator back iron volume	35.98	B59	$Inch^3$
Stator iron volume	76.62	B60	$Inch^3$
		B61	
Weight of the stators	42.29	B62	Lb.
Magnet weight	7.91	B63	Lb.
Wire weight	5.34	B64	Lb.
Rotor weight	11.40	B65	Lb.
Total active material weight	59.03	B66	Lb.
Specific power	1.69	B67	Hp/Lb.
Total active material cost	611	B68	$
		B69	
I^2*R loss at rated current	1257.36	B70	Watts
Teeth loss at rated speed	263.78	B71	Watts
Yoke loss at rated speed	150.30	B72	Watts
Efficiency at rated speed & torque	95.71	B73	%

APPENDIX A2

SOLUTION FOR B_r, B_θ, and B_z

In this appendix the most general form of the solution for B_r, B_θ, and B_z is obtained by solving the three dimensional partial differential equations. In deriving this general solution, it is assumed that inside the air gap, electrostatic flux density and charge density are very small and therefore can be considered to be zero.

The Maxwell's equations can be written as follows:

$$\text{Curl } H = J \tag{A2.1}$$

$$\text{Curl } E = -\frac{\partial B}{\partial t} \tag{A2.2}$$

$$\text{Div } B = 0 \tag{A2.3}$$

The geometry of the two sets of flow paths is controlled by the material properties defined by the following equations:

$$E = \rho J \tag{A2.4}$$

$$B = \mu H \tag{A2.5}$$

Equations (A2.2) and (A2.4) result in

$$\text{Curl } (\rho J) = -\frac{\partial B}{\partial t} \tag{A2.6}$$

Equations (A2.6) and (A2.1) give

$$\text{Curl } (\rho . \text{Curl } H) = -\frac{\partial B}{\partial t} \tag{A2.7}$$

Equations (A2.5) and (A2.7) yield

$$\text{Curl . Curl (B)} + \frac{\mu}{\rho}\frac{\partial B}{\partial t} = 0 \qquad \text{(A2.8)}$$

By considering the z component of equation (A2.8)

$$\frac{1}{r}\left[\frac{\partial}{\partial r}\left\{r\left(\frac{\partial B_r}{\partial z} - \frac{\partial B_z}{\partial r}\right)\right\} - \frac{\partial}{\partial \theta}\left(\frac{1}{r}.\frac{\partial B_z}{\partial \theta} - \frac{\partial B_\theta}{\partial z}\right)\right] + \frac{\mu}{\rho}\frac{\partial B_z}{\partial t} = 0 \qquad \text{(A2.9)}$$

$$\frac{1}{r}\left[\frac{\partial^2}{\partial r.\partial z}(rB_r) - \frac{\partial}{\partial r}\left(r.\frac{\partial B_z}{\partial r}\right) - \frac{1}{r}.\frac{\partial^2 B_z}{\partial \theta^2} + \frac{\partial^2 B_\theta}{\partial \theta.\partial z}\right] + \frac{\mu}{\rho}\frac{\partial B_z}{\partial t} = 0 \qquad \text{(A2.10)}$$

Now we can make use of equation (A2.3), which is

$$\frac{\partial}{\partial r}(rB_r) + \frac{1}{r}\frac{\partial}{d\theta}(rB_\theta) + r\frac{\partial B_z}{\partial z} = 0 \qquad \text{(A2.11)}$$

and simplifying yields

$$\frac{\partial^2}{\partial r.\partial z}(rB_r) = -\frac{1}{r}.\frac{\partial^2}{\partial \theta.\partial z}(rB_\theta) - r\frac{\partial^2 B_z}{\partial z^2} \qquad \text{(A2.12)}$$

Substituting for $\frac{\partial^2}{\partial r.\partial z}(rB_r)$ in (A2.10) results

$$\left[\frac{\partial^2}{\partial r^2} + \frac{1}{r}\frac{\partial}{dr} + \frac{1}{r^2}\frac{\partial^2}{\partial \theta^2} + \frac{\partial^2}{\partial z^2} - \frac{\mu}{\rho}.\frac{\partial}{\partial t}\right] B_z = 0 \qquad \text{(A2.13)}$$

By considering r component of equation (A2.8)

$$\frac{1}{r}\left[\frac{\partial}{\partial \theta}\left(\frac{1}{r}\frac{\partial}{\partial r}rB_\theta - \frac{\partial B_r}{\partial \theta}\right)\right] - \frac{\partial}{\partial z}\left(\frac{\partial B_r}{\partial z} - \frac{\partial B_z}{\partial r}\right) + \frac{\mu}{\rho}\frac{\partial B_r}{\partial t} = 0 \qquad \text{(A2.14)}$$

$$-\left(\frac{1}{r^2}\frac{\partial^2}{\partial \theta^2} + \frac{\partial^2}{\partial z^2}\right)(rB_r) + \frac{1}{r}\frac{\partial^2}{\partial r\partial \theta}(rB_\theta) + r\frac{\partial^2 B_z}{\partial z\partial r} + \frac{\mu}{\rho}\left(\frac{\partial(rB_r)}{\partial t}\right) = 0 \qquad \text{(A2.15)}$$

By using equation (A2.11)

$$\frac{\partial}{\partial r}\left(\frac{\partial}{\partial r}(rB_r)\right)+\frac{\partial}{\partial r}\left(\frac{1}{r}\frac{\partial}{d\theta}(rB_\theta)\right)+\frac{\partial}{\partial r}\left(r\frac{\partial B_z}{\partial z}\right)=0 \qquad \text{(A2.16)}$$

$$\frac{\partial^2}{\partial r^2}(rB_r)+\frac{1}{r}\frac{\partial^2}{\partial r\partial\theta}(rB_\theta)-\frac{1}{r^2}\frac{\partial}{\partial\theta}(rB_\theta)+\frac{\partial B_z}{\partial z}+r^2\frac{\partial^2 B_z}{\partial r\partial z}=0 \qquad \text{(A2.17)}$$

Equations (A2.11) and (A2.17) result in

$$\frac{\partial^2}{\partial r^2}(rB_r)+\frac{1}{r}\frac{\partial^2}{\partial r\partial\theta}(rB_\theta)+\frac{1}{r}\left[\frac{\partial}{\partial r}(rB_r)+r\frac{\partial B_z}{\partial z}\right]+\frac{\partial B_z}{\partial z}+r^2\frac{\partial^2 B_z}{\partial r\partial z}=0 \qquad \text{(A2.18)}$$

$$\frac{1}{r}\frac{\partial^2}{\partial r\partial\theta}(rB_\theta)=-\frac{1}{r}\frac{\partial}{\partial r}(rB_r)-2\frac{\partial B_z}{\partial z}-r^2\frac{\partial^2 B_z}{\partial r\partial z}-\frac{\partial^2}{\partial r^2}(rB_r) \qquad \text{(A2.19)}$$

By substituting for $\frac{1}{r}\frac{\partial^2}{\partial r\partial\theta}(rB_\theta)$ in equation (A2.15) and simplyfying

$$\left[\frac{1}{r^2}.\frac{\partial^2}{\partial\theta^2}+\frac{\partial^2}{\partial z^2}+\frac{\partial^2}{\partial r^2}+\frac{1}{r}.\frac{\partial}{\partial r}-\frac{\mu}{\rho}.\frac{\partial}{\partial t}\right](rB_r)=-2.\frac{\partial B_z}{\partial z} \qquad \text{(A2.20)}$$

By considering θ component of equation (A2.8)

$$\frac{\partial}{\partial z}\left[\frac{1}{r}\frac{\partial B_z}{\partial\theta}-\frac{\partial B_\theta}{\partial z}\right]-\frac{\partial}{\partial r}\left[\frac{1}{r}\left(\frac{\partial}{\partial r}(rB_\theta)-\frac{\partial B_r}{\partial\theta}\right)\right]+\frac{\mu}{\rho}\frac{\partial B_\theta}{\partial t}=0 \qquad \text{(A2.21)}$$

Equation (A2.21) can be wriiten as

$$\left[\frac{-2}{r^3}\frac{\partial}{\partial\theta}+\frac{1}{r^2}\frac{\partial^2}{\partial r\partial\theta}\right](rB_r)+\left[\frac{1}{r^2}\frac{\partial}{\partial r}-\frac{1}{r}\frac{\partial^2}{\partial z^2}-\frac{1}{r}\frac{\partial^2}{\partial r^2}\right](rB_\theta)+\frac{1}{r}\frac{\partial^2 B_z}{\partial z\partial\theta}+\frac{\mu}{\rho}\frac{\partial B_\theta}{\partial t}=0 \qquad \text{(A2.22)}$$

By multiplying equation (A2.22) by *r* and rearranging

$$\left[\frac{1}{r}\frac{\partial^2}{\partial r\partial\theta}-\frac{2}{r^2}\frac{\partial}{\partial\theta}\right](rB_r)+\left[\frac{1}{r}\frac{\partial}{\partial r}-\frac{\partial^2}{\partial z^2}-\frac{\partial^2}{\partial r^2}\right](rB_\theta)+\frac{\partial^2 B_z}{\partial z\partial\theta}+\frac{\mu}{\rho}\frac{\partial(rB_\theta)}{\partial t}=0 \qquad \text{(A2.23)}$$

By taking the partial differentiation of equation (A2.11) with respect to θ result in

$$\frac{\partial^2 B_z}{\partial z \partial \theta} = -\frac{1}{r}\frac{\partial^2}{\partial \theta \partial r}(rB_r) - \frac{1}{r^2}\frac{\partial^2}{\partial \theta^2}(rB_\theta) \qquad \text{(A2.24)}$$

By substituting for $\frac{\partial^2 B_z}{\partial z \partial \theta}$ in equation (A2.23) and simplyfying result in

$$\left[\frac{\partial}{\partial r} - r.\frac{\partial^2}{\partial z^2} - r.\frac{\partial^2}{\partial r^2} - \frac{1}{r}.\frac{\partial^2}{\partial \theta^2} + r.\frac{\mu}{\rho}.\frac{\partial}{dt}\right](rB_\theta) = 2.\frac{\partial B_r}{\partial \theta} \qquad \text{(A2.25)}$$

APPENDIX A3

CALCULATION OF THREE FLUX COMPONENTS

This section briefly describes the method of calculation of three flux components for a brushless dc machine with the following parameters.

Magnet inner radius $= R_i = 4.17$ Inch

Magnet outer radius $= R_o = 5.50$ Inch

Number of pole pairs $= p = 6$

For this machine, equation (4.56) becomes

$$U_6(m5.50) = Y_6(m5.50).J_6(m4.17) - J_6(m5.50).Y_6(m4.17) = 0 \qquad \text{(A3.1)}$$

The roots of the above equation, m_i 's are obtained using MATHCAD and shown in Table A3.1. The number of roots, N, considered in this calculations is 50. The equations for B_r, B_θ, and B_z are given by equations (A3.2) ,(A3.5) and (A3.6) respectively.

$$B_r(r,\theta,z) = A.\frac{6}{r}\left\{\sum_{i=1}^{50}\left(U_6'(m_i r)\right).\left(e^{m_i z} - e^{-m_i z}\right)\right\}\left(Cos(6\theta)\right)$$

$$-\left\{\sum_{i=1}^{50} U_7(m_i r).\left(e^{m_i z} - e^{-m_i z}\right)\right\}\left(Cos(6\theta)\right) \qquad \text{(A3.2)}$$

where θ is in electrical degrees and

$$U_6'(m_i r) = \frac{Y_6(m_i 4.17)}{m_i}.J_6(m_i r) - \frac{J_6(m_i 4.17)}{m_i}.Y_6(m_i r) \qquad \text{(A3.3)}$$

$$U_7(m_i r) = Y_6(m_i 4.17).J_7(m_i r) - J_6(m_i 4.17).Y_7(m_i r) \qquad \text{(A3.4)}$$

$$B_\theta(r,\theta,z) = A.\frac{6}{r}\left\{\sum_{i=1}^{50} U_6(m_i r).\left(e^{m_i z} - e^{-m_i z}\right)\right\}\left(-Sin(6\theta)\right) \qquad \text{(A3.5)}$$

$$B_z(r,\theta,z) = A.\left\{\sum_{i=1}^{50} U_6(m_i r).\left(e^{m_i z} + e^{-m_i z}\right)\right\}(Cos(6\theta)) \qquad \text{(A3.6)}$$

where $U_6(m_i r) = Y_6(m_i 4.17)J_6(m_i r) - J_6(m_i 4.17)Y_6(m_i r)$ (A3.7)

Now using the boundary condition for $B_z(r,\theta,z)$ at z=0 and $\theta = 0$ and r=4.835

$$B_z(4.835,0,0) = 1.216 \qquad \text{(A3.8)}$$

Equation (A3.6) and (A3.8) can be used to find the value of A. Thus

A= -24.575

Now using equations (A3.2), (A3.5) and (A3.6), the peak value of three flux components $B_{r,,}$ B_θ, and B_z as z varies from zero to effective gap length, at r=4.835 and θ=0 can be found. These values are shown in Table 4.1 , Table 4.2 and table 4.3 respectively. By neglecting the magnet to magnet leakage and considering the physical placement of magnets, the variation of three flux components, $B_{r,,}$ B_θ, and B_z as θ varies from -90 to +90 electrical degrees could be obtained by using equations (A3.2), (A3.5) and (A3.6) respectively. These results are shown in Table 4.4.

Table A3.1 Roots of $U_6(m.5.50) = 0$ and corresponding values of $U_6(m_i r)$, $U_6'(m_i r)$ and $U_7(m_i r)$ for r=4.835 inch

Root #	Root value, m_i	$U_6(m_i r)$	$U_6'(m_i r)$	$U_7(m_i r)$
1	2.667	-0.061	-0.023	-0.065
2	4.881	$5.496*10^{-4}$	$-1.126*10^{-4}$	0.002
3	7.199	0.02	0.003	0.02
4	9.54	$1.667*10^{-5}$	$1.747*10^{-6}$	$3.589*10^{-4}$
5	11.889	-0.0121	-0.001	-0.012
6	14.242	$4.695*10^{-5}$	$3.297*10^{-6}$	$-1.045*10^{-4}$
7	16.598	0.009	$5.163*10^{-4}$	0.009
8	18.955	$-5.491*10^{-5}$	$-2.897*10^{-6}$	$3.016*10^{-5}$
9	21.313	-0.007	$3.127*10^{-4}$	-0.007
10	23.672	$5.239*10^{-5}$	$2.213*10^{-6}$	$-2.037*10^{-6}$
11	26.031	0.005	$2.095*10^{-4}$	0.005
12	28.391	$4.778*10^{-5}$	$-1.683*10^{-6}$	$-9.985*10^{-6}$
13	30.751	-0.005	$-1.501*10^{-4}$	-0.005
14	33.111	$4.309*10^{-5}$	$1.301*10^{-6}$	$1.532*10^{-5}$
15	35.472	0.004	$1.128*10^{-4}$	0.004
16	37.833	$-3.882*10^{-5}$	$-1.026*10^{-6}$	$-1.756*10^{-5}$
17	40.193	-0.004	$-8.871*10^{-6}$	-0.004
18	42.554	$3.506*10^{-5}$	$8.24*10^{-7}$	$1.827*10^{-5}$
19	44.916	0.003	$7.031*10^{-5}$	0.003
20	47.277	$-3.179*10^{-5}$	$-6.725*10^{-7}$	$-1.818*10^{-5}$
21	49.638	-0.003	$-5.756*10^{-5}$	-0.003
22	51.999	$2.894*10^{-5}$	$5.565*10^{-7}$	$1.769*10^{-5}$
23	54.361	0.003	$4.799*10^{-6}$	0.003

24	56.722	$-2.644*10^{-5}$	$-4.662*10^{-7}$	$-1.699*10^{-5}$
25	59.083	-0.002	$-4.062*1o^{-5}$	-0.002
26	61.445	$2.425*10^{-5}$	$3.947*10^{-7}$	$1.62*10^{-5}$
27	63.806	0.002	$3.483*10^{-5}$	0.002
28	66.168	$-2.231*10^{-5}$	$-3.372*10^{-7}$	$1.537*10^{-5}$
29	68.529	-0.002	$-3.019*10^{-5}$	0.002
30	70.891	$2.059*10^{-5}$	$2.904*10^{-7}$	$1.454*10^{-5}$
31	73.253	0.002	$2.643*10^{-5}$	0.002
32	75.614	$-1.905*10^{-5}$	$-2.519*10^{-7}$	$-1.37?*10^{-5}$
33	77.976	-0.002	$2.332*10^{-5}$	0.002
34	80.337	$1.766*10^{-5}$	$2.199*10^{-7}$	$1.295*10^{-5}$
35	82.699	0.002	$2.073*10^{-5}$	0.002
36	85.061	$-1.642*10^{-5}$	$-1.930*10^{-7}$	$-1.22*10^{-5}$
37	87.423	-0.002	$-1.855*10^{5}$	-0.002
38	89.784	$1.529*10^{-5}$	$1.703*10^{-7}$	$1.152*10^{-5}$
39	92.146	0.002	$1.67*10^{-5}$	0.002
40	94.508	$-1.426*10^{-5}$	$-1.509*10^{-7}$	$-1.086*10^{-5}$
41	96.869	-0.001	$1.511*10^{-5}$	-0.001
42	99.231	$1.332*10^{-5}$	$1.343*10^{-7}$	$1.023*10^{-5}$
43	101.593	0.001	$1.374*10^{-5}$	0.001
44	103.955	$1.246*10^{-5}$	$-1.199*10^{-7}$	$-9.65*10^{-6}$
45	106.316	-0.001	$-1.254*10^{-5}$	-0.001
46	108.678	$1.167*10^{-5}$	$1.074*10^{-7}$	$9.1*10^{-6}$
47	111.04	0.001	$1.15*10^{-5}$	0.001
48	113.402	$-1.095*10^{-5}$	$-9.652*10^{-8}$	$-8.582*10^{-6}$
49	115.674	-0.001	$-1.058*10^{-5}$	-0.001
50	118.125	$1.027*10^{-5}$	$8.697*10^{-8}$	$8.095*10^{-6}$

VITAE

Ajith H. Wijenayake was born in Matugama, Sri Lanka on October 23, 1959. From 1964 to 1973, he attended Matugama Central College, Matugama, Sri Lanka. Then he went to Ananda College, Colombo, Sri Lanka for his high school studies and finished the General Certificate of Education (Advanced Level) in 1976, ranking number 6 in the university entrance examination in Engineering. He received a B.Sc.(Hons) degree in Electrical Engineering from the University of Moratuwa, Moratuwa, Sri Lanka, in 1982. From January 1982 to June 1982, he worked as a temporary faculty member in he Department of Electrical Engineering, University of Moratuwa, Moratuwa, Sri Lanka. From June 1982 to December 1986, he worked as a Telecommunication Engineer in the Ministry of Post, Telegraph, and Telecommunication, Riyadh, Kingdom of Saudi Arabia. He went to pursue his graduate studies at Louisiana State University, Baton Rouge, Louisiana, U. S. A and received a M.Sc degree in Electrical Engineering in 1989. From 1990 to 1995, he pursued his doctoral studies at the University of Tennessee, Knoxville, Tennessee, U.S.A. From May 1990 to December 1991, he also worked as a Test Engineer at Electric Power Research Institute's Power Electronics Application Center, Knoxville, Tennessee. He received his Ph.D. degree in Electrical Engineering in August, 1995.

Since April, 1995 he has been working at Allen-Bradley Co., Inc. as a Senior Research Engineer. His current research interests are in Power Electronics and Machine Design . He has published several technical papers on these subjects.